TURBULENCE STRUCTURE IN STRATIFIED FLOW(Dissertation_全文)

AUTHOR(S):

Komori, Satoru

TURBULENCE STRUCTURE IN STRATIFIED FLOW

SATORU KOMORI

TURBULENCE STRUCTURE IN STRATIFIED FLOW

SATORU KOMORI

TURBULENCE STRUCTURE IN STRATIFIED FLOW

By

Satoru Komori

B.S., Kyoto University, 1974

M.S., Kyoto University, 1976

DOCTORAL DISSERTATION

Submitted to

Kyoto University

in partial fulfillment of
the requirements for the degree of

Doctor of Philosophy

in

Engineering

Commencement March 1980

ACKNOWLEDGEMENTS

The author would like to express his sincere gratitude to Professor T.Mizushina, the author's advisor, who provided him many helpful suggestions and encouragement in the course of preparation of the dissertation.

Many thanks to Dr. F.Ogino, Assistant Professor of Kyoto University and Dr. H. Ueda , Research Manager of Atmospheric Environment Division , the National Institute for Environmental Studies, for their continued interest and many important advices on this study.

Messrs S.Machida, K.Maeda and Y.Kawai have helped the author in conducting the experiments. The author acknowledges their great help.

Thanks also to Miss K.Yoshinari for her kind help in printing the dissertation.

TABLE OF CONTENTS

LIST OF TABLES

LIST OF PLATES

LIST OF FIGURES

Page

Page

LIST OF SYMBOLS

a	: Tangent of ψ	[ ]
b	: Temperature gradient $(= \partial\overline{T}/\partial y)$	[K/m]
C_1	: Correlation value $(=\overline{u_a\|_{\zeta=0}\, \partial^2\theta/\partial t^2\|_{\zeta=0}})$	[m·K/s^3]
C_2	: Correlation value $(=\overline{v_a\|_{\zeta=0}\, \partial^2\theta/\partial t^2\|_{\zeta=0}})$	[m·K/s^3]
c	: Velocity of light	[m/s]
d_i	: Scattering volume dimension in the i direction	[m]
E_{ij}	: Spectrum function of $\overline{(u_i)_A(u_j)_B}$ nondimensionalized by $\nu(t_t-t_0)/J_0$	[ ]
$E_{i\theta}$	: Spectrum function of $\overline{(u_i)_A(\theta)_B}$ nondimensionalized by $\nu/(J_0 b)$	[ ]
$E_{\theta j}$	: Spectrum function of $\overline{(\theta)_A(u_j)_B}$ nondimensionalized by $\nu/(J_0 b)$	[ ]
$E_{\theta\theta}$	: Spectrum function of $\overline{(\theta)_A(\theta)_B}$ nindimensionalized by $\nu/((t_t-t_0)J_0 b^2)$	[ ]
e	: Erroneous velocity due to the broadening	[m/s]
F_r	: Froude number $(=\overline{U}_{ave}/(g\delta)^{1/2})$	[ ]
$F(\sigma)$	: Flatness factor of $\sigma(t)$ $(= \overline{\sigma^4}/(\overline{\sigma^2})^2)$	[ ]
f	: Frequency	[1/s]
f_1	: x co-ordinate of the light beam	[m]
f_2	: y co-ordinate of the light beam	[m]
f_1'	: Fluctuating component of f_1	[m]
f_2'	: Fluctuating component of f_2	[m]
g	: Gravitational acceleration	[m/s^2]
J_0	: Constant that depends on initial conditions	[m^7/s^2]
K	: Thermal diffusivity	[m^2/s]
k	: Wavenumber $(=2\pi f/\overline{U})$	[1/m]

k_i	: Dimensionless wavenumber component in the i direction $(=\nu^{1/2}(t_t-t_0)^{1/2}\kappa_i)$	[ ]
ℓ	: Distance from the light source to the receiver in the z direction	[m]
ℓ_1	: Position of the light source	[m]
ℓ_2	: Position of the receiver	[m]
N	: Vaisala frequency $(=(\beta g \partial\overline{T}/\partial y)^{1/2})$	[1/s]
n	: Refractive index	[ ]
n_0	: Averaged refractive index	[ ]
n'	: Fluctuating component of n	[ ]
Pr	: Prantl number $(=\nu/K)$	[ ]
$P\sigma$	: Normalized probability density functions of $\sigma(t)$	[ ]
$P\sigma_1\sigma_2$	: Normalized joint probability density functions of $\sigma_1(t)$ and $\sigma_2(t)$	[ ]
p	: Fluctuating pressure	[Pa]
Q_{ij}	: Velocity-velocity correlation $(=\overline{(u_i)_A(u_j)_B})$	$[m^2/s^2]$
Q_{ip}	: Velocity-pressure correlation $(=\overline{(u_i)_A(p)_B})$	[Pa·m/s]
Q_{pj}	: Pressure-velocity correlation $(=\overline{(p)_A(u_j)_B})$	[Pa·m/s]
$Q_{i\theta}$	: Velocity-temperature correlation $(=\overline{(u_i)_A(\theta)_B})$	[K·m/s]
$Q_{\theta j}$	: Temperature-velocity correlation $(=\overline{(\theta)_A(u_j)_B})$	[K·m/s]
$Q_{\theta\theta}$	: Temperature-temperature correlation $(=\overline{(\theta)_A(\theta)_B})$	$[K^2]$
$\overline{q^2}$	: Turbulence kinetic energy $(=\overline{u^2}+\overline{v^2}+\overline{w^2})$	$[m^2/s^2]$
R	: Hydraulic radius $(=\delta W/(2\delta+W))$	[m]
Re	: Reynolds number $(=4R\overline{U}_{ave}/\nu)$	[ ]
Ri	: Local gradient Richardson number	

	$(=\beta g(\partial\overline{T}/\partial y)/(\partial\overline{U}/\partial y)^2)$	[ ]
$\overline{Ri}$	: Bulk Richardson number	
	$(=\beta gR(\overline{T}_{suf}-\overline{T}_{bot})/\overline{U}_{ave}^2)$	[ ]
R_{uv}	: Correlation coefficient between u and v	
	$(=-\overline{uv}/u'v')$	[ ]
$R_{u\theta}$	: Correlation coefficient between u and θ	
	$(=\overline{u\theta}/u'\theta')$	[ ]
$R_{v\theta}$	: Correlation coefficient between v and θ	
	$(=-\overline{v\theta}/v'\theta')$	[ ]
$\mathbf{r}$	: Distance vector from point A to point B	
	$(=(\xi_1,\xi_2,\xi_3))$	
$S_{aa}(f)$	: Power spectrum of u_{ia}	$[m^2/s]$
$S_{ff}(f)$	: Power spectrum of u_{if}	$[m^2/s]$
$S_{rr}(f)$	: Power spectrum of u_{ir}	$[m^2/s]$
$S_{uu}(f)$	: Power spectrum of u	$[m^2/s]$
$S_{vv}(f)$	: Power spectrum of v	$[m^2/s]$
$S_{\theta\theta}(f)$	: Power spectrum of θ	$[K^2\cdot s]$
$S_{\ddot{\theta}\ddot{\theta}}(f)$	: Power spectrum of $\partial^2\theta/\partial t^2$	$[K^2/s^3]$
$S_{uu}(k)$	: Normalized power spectrum of u	
	$(=S_{uu}(f)\overline{U}/2\pi)$	$[m^3/s^2]$
S_{ij}	: Dimensionless spectrum of $\overline{u_i u_j}$ averaged	
	over all directions in wavenumber space	[ ]
$S_{i\theta}$	: Dimensionless spectrum of $\overline{u_i\theta}$ averaged	
	over all directions in wavenumber space	[ ]
$S_{\theta\theta}$	: Dimensionless spectrum of $\overline{\theta\theta}$ averaged	
	over all directions in wavenumber space	[ ]
$S(\sigma)$	: Skewness factor of $\sigma(t)$ $(=\overline{\sigma^3}/(\overline{\sigma^2})^{3/2})$	[ ]
s	: Space co-ordinate along the light path	[m]
$\overline{T}$	: Time-averaged temperature	[K]

t	: Time	[s]
t_0	: Initial time	[s]
t_t	: Terminal time	[s]
U_{ia}	: Apparent velocity in the i direction	[m/s]
U_{ir}	: Real velocity in the i direction	[m/s]
$\overline{U}$	: Time-averaged velocity in the streamwise direction	[m/s]
$\overline{U}_{ave}$	: Cross-sectional time-averaged velocity	[m/s]
u	: Fluctuating velocity in the streamwise (x) direction	[m/s]
u_{ia}	: Apparent fluctuating velocity in the i direction	[m/s]
u_{if}	: Fictitious fluctuating velocity in the i direction	[m/s]
u_{ir}	: Real fluctuating velocity in the i direction	[m/s]
u'	: Root mean square value of u $(=(\overline{u^2})^{1/2})$	[m/s]
u^*	: Friction velocity $(=(\tau_w/\rho)^{1/2})$	[m/s]
$\mathbf{u}_r$	: Real velocity vector $(=(U_{1r},U_{2r},U_{3r}))$	
v	: Fluctuating velocity in the vertical (y) direction	[m/s]
v'	: Root mean square value of v $(=(\overline{v^2})^{1/2})$	[m/s]
W	: Width of the flume	[m]
w	: Fluctuating velocity in the lateral (z) direction	[m/s]
x	: Space co-ordinate in the streamwise direction $(= x_1)$	[m]
x_i	: Space co-ordinate in the i direction	[m]
y	: Vertical distance from the bottom floor of the flume or space co-ordinate in the	

	vertical direction ($=x_2$)	[m]
z	: Space co-ordinate in the lateral direction ($=x_3$)	[m]

Greek Symbols

α	: Temperature dependence of the refractive index	[1/K]
β	: Expansion coefficient	[1/K]
γ	: Spherical co-ordinate in wavenumber space	[ ]
δ	: Flow depth	[m]
δ_{ij}	: Kronecker delta	[ ]
ε	: Viscous dissipation rate	[m^2/s^3]
ε_h	: Eddy diffusivity of heat	[m^2/s]
ε_m	: Eddy diffusivity of momentum	[m^2/s]
ζ	: Replaced variable ($=\ell-z$)	[m]
θ	: Fluctuating temperature	[K]
$\ddot{\theta}$	: Second partial derivative of θ with respect to time	[K/s^2]
θ'	: Root mean square value of θ ($=(\overline{\theta^2})^{1/2}$)	[K]
κ_i	: Component of wavenumber vector	[1/m]
$\mathbb{k}$	: Wavenumber vector	
Λ	: Integral scale	[m]
λ	: Wave length of laser beam	[m]
ν	: Kinematic viscosity	[m^2/s]
ξ_i	: Distance from point A to point B in the i direction	[m]

ρ	: Density	$[kg/m^3]$
σ	: Random variable $(=\sigma(t))$	
σ_1	: Random variable $(=\sigma_1(t))$	
σ_2	: Random variable $(=\sigma_2(t))$	
τ	: Dimensionless time $(=(\partial \overline{U}/\partial y)(t-t_0))$	[ ]
τ_t	: τ at $t=t_t$	[ ]
τ_w	: Shear stress at the wall	$[kg/m\cdot s^2]$
$\boldsymbol{\tau}$	: Tangential unit vector of the beam	
υ	: Doppler frequency	[1/s]
υ_0	: Doppler frequency at the light source	[1/s]
ϕ	: Spherical co-ordinate in wavenumber space	[ ]
χ	: Experimental constant	[ ]
ψ	: One half of beam intersection angle	[rad]
ω	: Dimensionless wavenumber $(=(k_1^2+(k_2-k_1\tau)^2+k_3^2)^{1/2})$	[ ]

Superscripts

—	: Time-averaged

Subscripts

A	: At point A
a	: Apparent
B	: At point B
bot	: In the immediate vicinity of the bottom floor of the flume
c	: Conditional averaged
F	: due to finite transit time

f	: Fictitious
G	: Due to gradients in mean velocity
i,j,k	: Three co-ordinate directions
max	: Maximum
N	: Due to electric noise
n	: In neutral conditions
P	: Due to instrumental bandwidth
r	: Real
suf	: In the immediate vicinity of the free surface
T	: Due to small scale turbulent fluctuations

CHAPTER 1 INTRODUCTION

The fluids appearing in the environment are in motion; and often the flow is turbulent. In addition, since heat transfer on the environmental scale usually involves buoyancy effects, it is important to know the interaction between buoyancy and turbulence. Such flow configurations of an environmental heat transfer process with governing influence of buoyancy are stratified shear flows which have been an important subject of study in the atmospheric boundary layer , the ocean and in many industrial operations.

The stratified shear flows are divided into the two flow configurations; stably stratified flow and unstably stratified flow. In the stably stratified flow, mean temperature and velocity gradients are positive in the vertical y direction. For a positive temperature gradient, a turbulent eddy moving upward, for instance, is normally colder than the surrounding fluids. Then, buoyancy forces will tend to decelerate the eddy moving upward. Similarly, an eddy moving downward will be decelerated. Therefore, the flow with a positive temperature gradient is generally called "stably stratified flow". However, real flow does not consist of such simple motions, as will be discussed in subsequent chapters.

In unstably stratified flow, a mean temperature gradient is negative in the vertical direction. For a negative temperature gradient, it can be seen that the buoyancy effect will be contrary to that in stably stratified flow; that is, the buoyancy forces will tend to accelerate the eddy motions. Thus, the flow with a negative gradient is generally called "unstably stratified flow".

Field observations of the stratified flows have been performed by many geophysicists; Charnock[1], Businger et al.[2], Haugen et al. [3], Wyngarrd & Cote'[4], Wyngarrd et al.[5], McBean & Miyake[6] and

Pruitt et al.[7].

The standards of accuracy desired or attained in these meteorological observations are, however, lower than those in laboratory experiments and the results from the field observations should be treated with some reserve in respect to the steadiness of the flow and flow-direction, constancy of the momentum and heat fluxes, and radiation effect. Laboratory experiments were also performed by Webster[8], Arya & Plate[9] and Arya[10] in specially designed wind tunnels and by Ellison & Turner[11], Schiller & Sayre[12] and Strele & Sayre[13] in open channels.

Most of these field observations and laboratory experiments concern the measurements of the eddy diffusivities of momentum and heat. The eddy diffusivities are, however, inherently insufficient to clarify turbulence structure, and also a few measurements of turbulence quantities are not conclusive, because of a wide scattering among the individual experiments and because of the limited experimental condition of rather weak stability or instability.

In recent years, some turbulence models for stratified turbulent flows have been presented. Most of these models belong to a type of the multi-equation models based on one-point correlation equations, and they involves many empirical constants and functions in themselves to close the correlation equations. Deardorff[14], Launder[15], Gibson & Launder[16] and others have developed second order turbulence closures based on approximated sets of transport equations for momentum and heat fluxes, and applied them to the experimental results obtained in atmospheric layers and wind tunnels. However, these theoretical considerations are not complete because of the lack of detailed information on the turbulence structure under stratified conditions.

The purpose of this study is to clarify the buoyancy effects on the turbulence structure, by presenting reliable turbulence measurements in stratified shear flows, in particular, in strongly stratified flows, and to offer the experimental results for use in the closure problems of turbulence.

The heart of this study is in chapters 2 and 3, and there turbulence structures both in stably and unstably stratified flows are clarified experimentally by means of various statistical analyses and flow visualization technique.

Velocity and temperature fluctuations are simultaneously measured by a laser Doppler velocimeter and a cold-film probe in a bridge arrangement. Measurements include turbulence intensities, correlation coefficients of heat fluxes and the Reynolds stress, probability density and joint probability density functions, skewness and flatness factors, coherence-phase relationships between velocity and temperature and others. The experiments were performed in an open channel, in which strongly stratified flows were attained by limiting the temperature field to the region near the free surface where the velocity gradient is small. Strictly speaking, the flows investigated in this study are not fully developed, but may be regarded as ones of the most ideal flows which are close to plane-homogeneity. In such flows, as well as in fully-developed homogeneous flow, a suitable framework for presenting and discussing the results may be provided through theoretical and similarity considerations.

Thus, the measured turbulence quantities are discussed by using two stability parameters; the bulk Richardson number,

$$\overline{Ri} = \beta g R(\overline{T}_{suf} - \overline{T}_{bot})/\overline{U}_{ave}^{2}$$

and the local gradient Richardson number,

$$Ri = \beta g(\partial\overline{T}/\partial y)/(\partial\overline{U}/\partial y)^2 .$$

Variations of the turbulence quantities with $\overline{Ri}$ are also discussed by using their transport equations.

Chapter 4 deals with a theoretical consideration by a spectral equation model. As mentioned above, most of the current models are multi equation models and require many empirical constants and functions. A new practical model involving the empirical constants and functions based on the experimental results in chapters 2 and 3 should be developed. Its work is, however, left as a future one, and here a spectral equation model based on two-point correlation equations was applied to the stratified flows. The spectral equation model requires no empirical constants and no functions except only two assumptions; the neglect of the inertial effects and the homogeneity of the flow, but it has a drawback that it is difficult to predict quantitatively the experimental results obtained in a steady state. Therefore, the results calculated by the spectral equation model were qualitatively compared with the experimental results in chapters 2 and 3.

In chapter 5, an application of laser Doppler velocimetry to turbulence measurement in stratified flow is discussed. The interaction effect of the laser beams with the turbulent temperature fluctuations along the beam paths causes serious error to the measured velocity even in non-isothermal water flow with comparatively small temperature fluctuations. Thus, a correction method for such interaction effect was proposed in order to apply laser Doppler velocimetry to the turbulence measurements in the stratified flows in chapters 2 and 3.

CHAPTER 2 TURBULENCE STRUCTURE IN STABLY STRATIFIED FLOW

2.1 Introduction

In stably stratified flow many workers have investigated the turbulent transport mechanisms. The previous studies[2,7,8,9,11] show that in stable stratification the eddy diffusivities of heat and momentum decrease with increasing stability, and then the transport processes of heat and mass change drastically more than that of momentum, that is, the ratio of the eddy diffusivities of heat and momentum(the reciprocal of the turbulent Prandtl number) decreases remarkably. These changes in the transport processes arise through those of turbulence structure itself. Pao[17] and Stewart[18] suggested that the fluctuating motions in stably stratified flows consisted of turbulence and internal gravity waves. To distinguish between them, Stewart[18] and McBean & Miyake[6] analyzed coherence-phase relationships between vertical velocity and temperature fluctuations obtained from field observations, and showed that internal wave motions played an important role in stably stratified flows. Long[19] devised a theory of turbulence in stratified fluids with large Richardson number,i.e., under strongly stable conditions and reached the conclusion that turbulent transport of heat and momentum could occur only at the instant of the sporadic breakdown of finite amplitude gravity waves even in the strongly stable conditions. Turner[20] also discussed in detail the internal wave in stratified fluids.

Despite these works, detailed mechanisms of turbulent transport in stably stratified flow have not yet been clarified and more information on turbulence structure are required.

The purpose of this chapter is to present reliable turbulence measurements in stably stratified flow and to clarify the buoyancy effects on the turbulence structure by means of various statistical analyses and flow visualization technique. Stably stratified flow was obtained by condensing saturated steam at the free surface in the upstream region. Various turbulence quantities were measured and are discussed by using the bulk Richardson number, $\overline{Ri}$, and the local gradient Richardson number,Ri. Variations of the turbulence quantities with $\overline{Ri}$ are also discussed by using the contribution terms in their transport equations.

2.2 Experiment

2.2.1 Experimental apparatus and measuring equipment

Figure 2.1 illustrates the flow system of the experimental apparatus. Water was recirculated through the flume by a pump and the temperature of the water was kept to within $\pm$0.05K by controlling the flow rate of the cold water in a temperature regulating tank. Water from a head tank passed through a calibrated orifice and a flow control valve into a head box which was connected to the flume. The experimental flume is shown in more detail in figure 2.2. The inside width and the depth were 0.3m and 0.06m, respectively and the length was 6.1m. The side walls and the bottom were made of smooth stainless steel plates lined with 0.03m thickness glasswool to maintain adiabatic conditions. At the measuring station($x \simeq 3.0$m) the optical glass plates were installed at the side walls and the bottom floor for use with a laser Doppler velocimeter. To create the

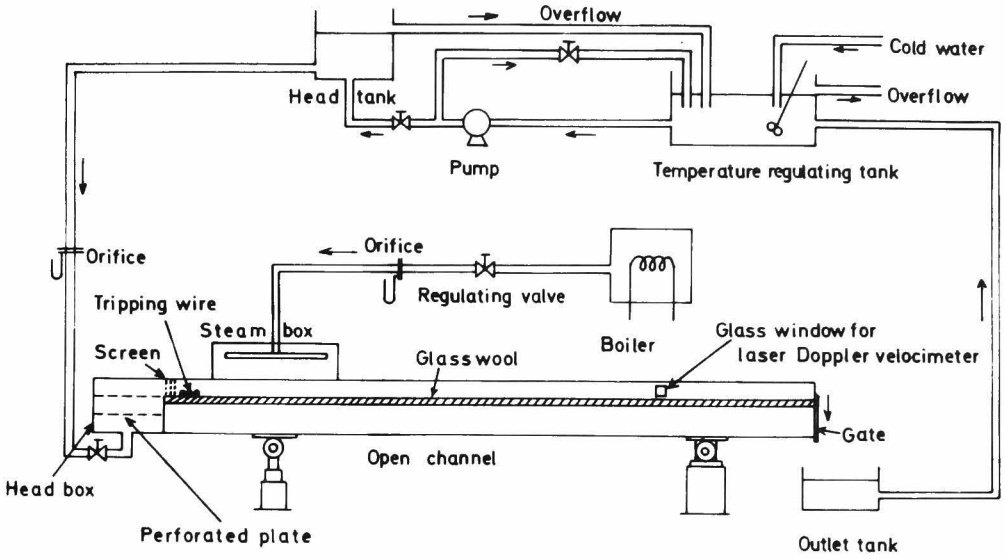

Figure 2.1. Flow system of experimental apparatus.

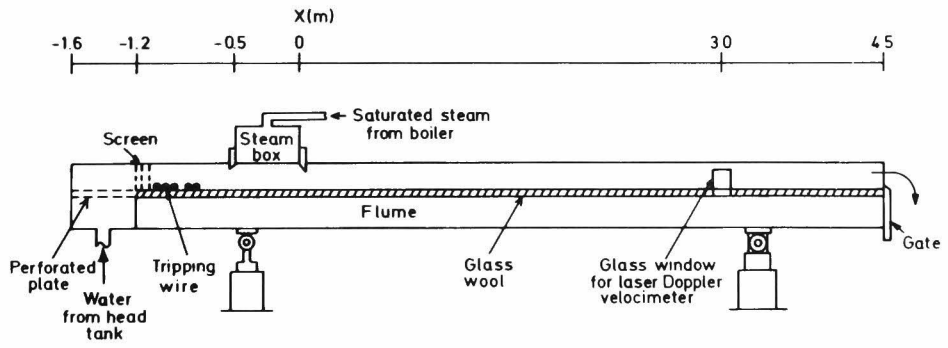

Figure 2.2. Experimental flume.

developed subcritical flow in shorter entrance region, seven tripping wires were mounted short distance from the inlet of the flume and two perforated plates and three screens(9 mesh) were installed in the head box and at the entrance of the flume, respectively. The slope of the flume could be varied in combination with the variation in the flow conditions.

To obtain stably stratified flow, saturated steam at 373K was mildly condensed on the free surface of the open channel flow in the region where the flow is in the fully developed condition. Steam was supplied from a steam box located at a distance 1.6m downstream from the inlet of the flume. The frame of the steam box is shown in figure 2.3. The rate of condensation was less than 8.8×10^4 $J/m^2 \cdot s$ and, with a simple calculation, the effect of the condensation was confirmed to be negligible at the measuring station.

Figure 2.4 shows a block diagram of the measuring system used in this study. The measurements were performed at the center of the flume, at distance 3.0m downstream from the end of the steam box (x=0 in figure 2.2). For velocity measurement a DISA 55L laser Doppler velocimeter with a DISA 55L02 flow direction adapter was used. It worked in the fringe mode. The Doppler signals were processed with a DISA 55L35 frequency tracker. The laser used here was a Spectra-Physics 5 mW He-Ne laser(model 120). The split laser beams were passed through the optical glass plates installed at the side walls and were focussed on the center line of the flume by means of a 600 mm lens with the beam intersection angle of 4.4°. In the case of the measurement of the lateral velocity component the beams were passed through the optical glass plate installed at the flume floor and were focussed by a 130 mm lens. The intersection angle was 22° and the scattered light was collected above the free surface. The

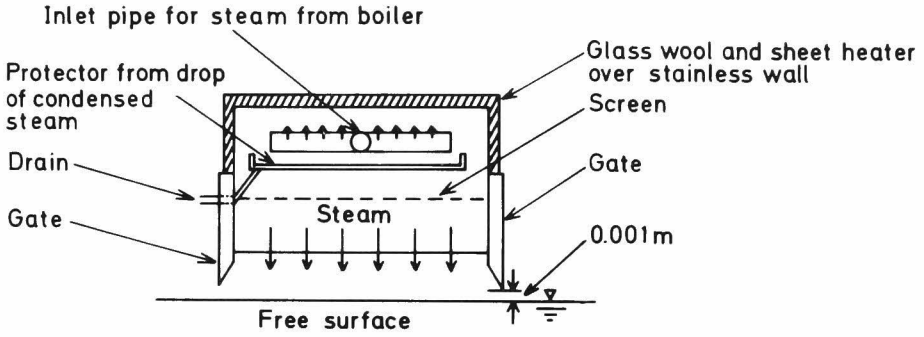

Figure 2.3. Frame of steam box.

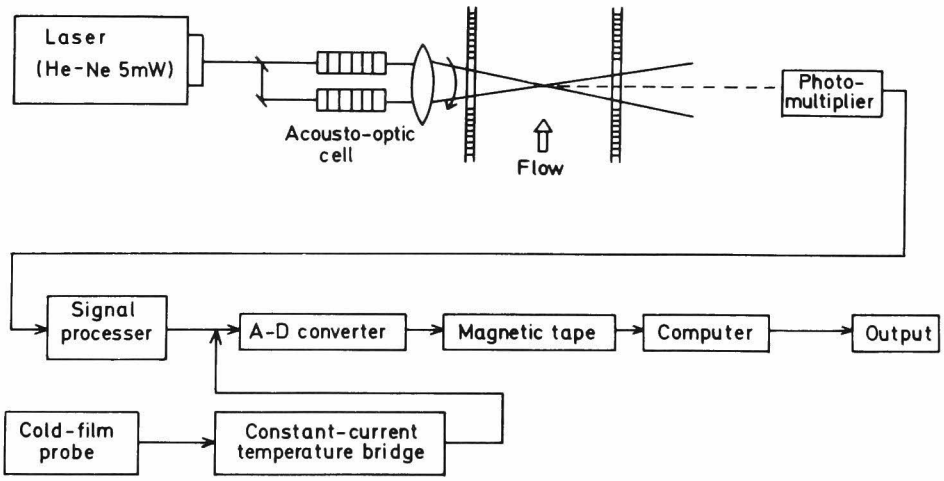

Figure 2.4. Block diagram of measuring system.

beam intersection was traversed vertically by a traversing mechanism. The Reynolds stress was measured by the Doppler velocimeter following a method analogous to that when using a single slanting hot-wire for the same purpose(Durst & Whitelaw[21]). In addition to this measurement, simultaneous measurements of the streamwise and vertical velocity components were made by a DISA 55M hot-film anemometry system with a DISA 55M14 temperature compensator in combination with the laser Doppler velocimetry.

When laser Doppler techniques are applied to non-isothermal flows, the laser beams encounter a succession of hot and cold pockets formed by turbulence eddies of various sizes and various temperatures, which modify phase and direction of the laser beams, and result in a measured apparent velocity. The correction for the apparent velocity due to the beam intersection effect was accomplished by the method which will be presented in chapter 5.

The time-averaged and fluctuating temperatures were measured by using a miniature conical, cold-film probe(TSI Model 1264) operated by a DISA 55M20 constant current temperature bridge.

The voltage outputs from the instruments were directly transmitted to a TEAC DP-4000 data acquisition system in which the signals were digitized and stored on magnetic tape. The sampling interval and the sample size were 0.01 second and about 25000, respectively. Statistical processing of the digitized data recorded on the magnetic tape was made with the FACOM OS IV/F4 computer system in the Data Processing Center of Kyoto University. In order to compute the power and cross spectral density functions, the standard Fourier transform relation with a Hanning lag-window weighting function(Bendat & Piersol[22]) was used.

2.2.2 Flow conditions

Flow conditions in the present investigation are listed in table 2.1. The flow depth, δ, was maintained at approximately 0.04m throughout the flume. The cross-sectional mean velocities $\overline{U}_{ave}$ ranged from 0.069m/s to 0.104m/s, so that the Reynolds numbers,Re, were 8600 to 17000 and the hydraulic Froude numbers,Fr, were less than 0.24; therefore,the flows investigated were turbulent flows under hydraulically subcritical condition. In table 2.1 the bulk Richardson number, $\overline{Ri}$, is equal to the reciprocal of the densimetric Froude number and its zero value means a neutral flow. The friction velocity,u*,was evaluated by using the so-called velocity profile method suggested by Clauser[23]. The two-dimensionality of the flows was checked by measuring the time-averaged velocity and temperature, and was confirmed in the wide region except in the region near the side walls. Such secondary circulation flow as shown by Schiller & Sayre[12] was not observed.
Symbols corresponding to experimental runs in table 2.1 will be used in the subsequent figures in this chapter.

2.3. Results and Discussion

2.3.1 Distributions of turbulence quantities

Time-averaged velocity and temperature

Figures 2.5 and 2.6 show typical distributions of the time-averaged velocities and temperatures in a strongly stable flow. $\overline{U}_{max}$ in figure 2.5 denotes the maximum time-averaged velocity. In this flow configuration a temperature gradient is established

Table 2.1. Flow conditions in stably stratified flows.

Run No.	Symbol	$\overline{Ri} \times 10^{-2}$[-]	Re[-]	$\delta \times 10^{-2}$[m]	$R \times 10^{-2}$[m]	$\overline{U}_{ave} \times 10^{-2}$[m/s]	$u^* \times 10^{-3}$[m/s]
I	△	0.0 (neutral)	8600	4.0	3.1	7.1	4.6
II	◔	1.35 (stable)	9100	4.0	3.2	7.3	4.7
III	○	2.31 (stable)	9800	4.0	3.1	7.4	4.7
IV	◐	6.39 (stable)	17000	3.9	3.1	10.4	6.1
V	●	15.3 (stable)	10500	3.9	3.1	6.9	4.3
VI	◕	19.0 (stable)	14800	3.9	3.1	7.8	4.7
VII	◒	21.3 (stable)	12600	3.8	3.1	7.4	4.5
VIII	◓	26.3 (stable)	12700	3.9	3.1	7.4	4.5
IX	◑	26.9 (stable)	14900	3.9	3.1	7.9	4.8

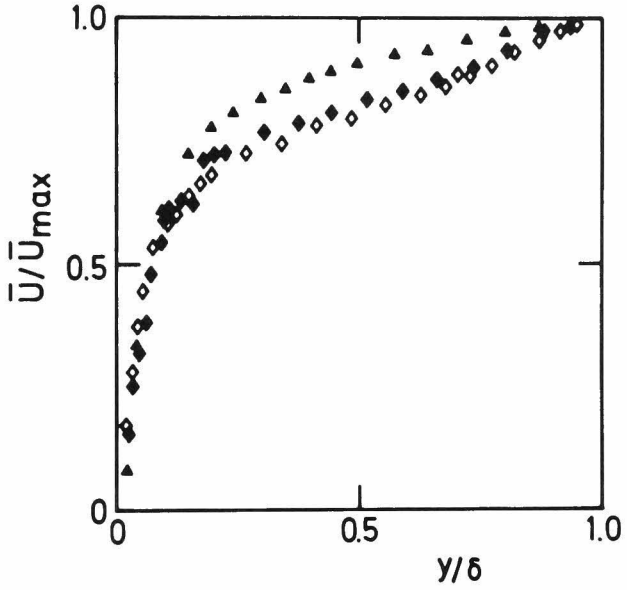

Figure 2.5. Typical distributions of the time-averaged velocities.

$\overline{Ri}$ = 2.5×10^{-2} , Re = 10100

◇ x/δ = 75.0 , ◆ x/δ = 62.5 , ▲ neutral flow

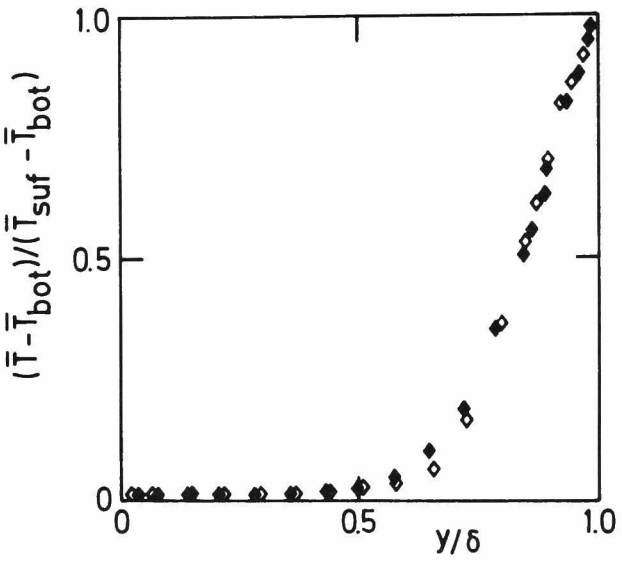

Figure 2.6. Typical distributions of the time-averaged temperatures.

Symbols as in figure 2.5.

near the free surface where the velocity gradient is comparatively small. In the strongly stable condition the temperature profile becomes steeper in the upper region of $y/\delta \gtrsim 0.6$ and a larger velocity gradient appears near the free surface than that in the neutral flow case. This is typical of the contrast with the neutral flow case. Plane-homogeneity in the sense that the distributions of the time-averaged velocity and temperature do not change noticeably in the flow direction may be approximately realized in the present experiments.

Turbulence intensities

Figure 2.7 shows the distributions of the r.m.s. values of the streamwise velocity fluctuation, u, normalized by the friction velocity, u*. The nondimensional r.m.s. value of the streamwise velocity fluctuation, u'/u*, decreases with increasing stability (increasing $\overline{Ri}$). The transport equation for the square value of the corresponding velocity component is written as

$$\frac{\overline{Du^2}}{Dt} = 2\overline{uv}\frac{\partial \overline{U}}{\partial y} + 2\overline{\frac{p}{\rho}\frac{\partial u}{\partial x}} \quad 2\nu\overline{\frac{\partial u}{\partial x_k}\frac{\partial u}{\partial x_k}} \quad \frac{\partial}{\partial x_k}\left[\overline{u^2 u_k} - \nu\frac{\partial \overline{u^2}}{\partial x_k} + 2\delta_{1k}\overline{\frac{up}{\rho}}\right], \quad (2\text{-}1)$$

where p is the pressure fluctuation, ν the kinematic viscosity, ρ the density of the fluid, δ_{ij} the Kronecker delta and repeated indices mean the summation convention. The first term on the right side of equation(2-1) represents the production by shear , the second the redisribution through pressure fluctuation, the third the viscous dissipation and the last represents the diffusion by turbulence fluctuation. Although it is not possible to estimate all of these terms, a remarkable decrease in the production by shear can be observed in figure 2.8 and this seems to cause the decrease of u'/u* with $\overline{Ri}$. In a strongly stable flow(Run VIII),a peak appears in the

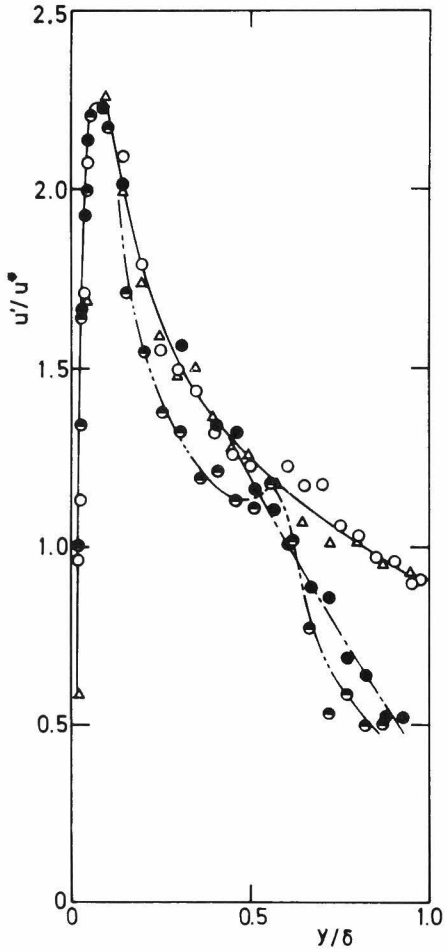

Figure 2.7. Distributions of the r.m.s. values of streamwise velocity fluctuations.
△ $\overline{Ri}$ = 0.0 , ○ $\overline{Ri}$ = 2.31×10^{-2},
● $\overline{Ri}$ = 1.53×10^{-1}, ◓ $\overline{Ri}$ = 2.63×10^{-1}

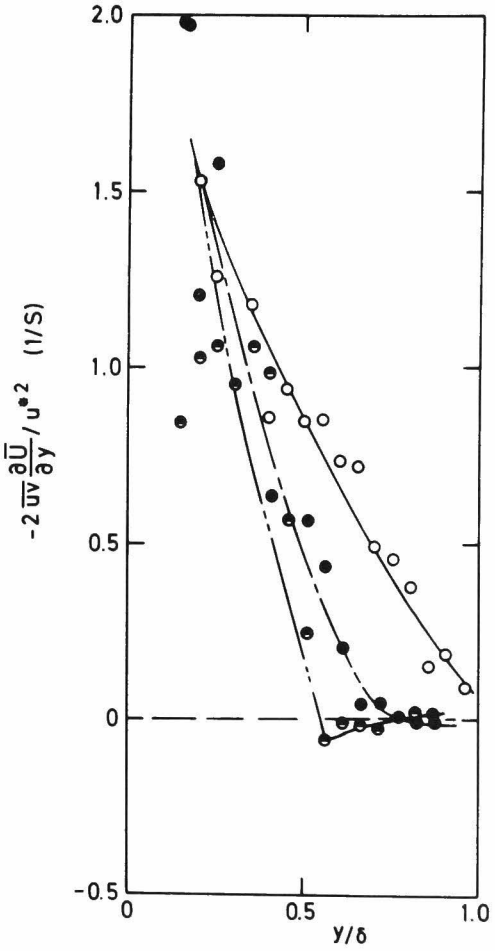

Figure 2.8. Distributions of the shear production term, $-2\overline{uv}(\partial \bar{U}/\partial y)/u^{*2}$.
Symbols as in figure 2.7.

u'/u* distribution at about y/δ=0.6.

As seen from figure 2.9, the nondimensional r.m.s. value of the vertical velocity fluctuation, v'/u*, decreases with increasing $\overline{Ri}$, while in the strongly stable conditions it clearly increases in the region $0.5 \lesssim y/\delta \lesssim 0.7$. This may be understood through the transport equation of $\overline{v^2}$,

$$\frac{\overline{Dv^2}}{Dt} = 2\beta g\overline{v\theta} + 2\overline{\frac{p}{\rho}\frac{\partial v}{\partial y}} \quad 2\nu\overline{\frac{\partial v}{\partial x_k}\frac{\partial v}{\partial x_k}} \quad \frac{\partial}{\partial x_k}[\overline{v^2 u_k} - \nu\frac{\partial\overline{v^2}}{\partial x_k} + 2\delta_{2k}\overline{\frac{vp}{\rho}}], \quad (2\text{-}2)$$

where θ is the temperature fluctuation.
The first term on the right of equation(2-2) is the so-called buoyancy term and represents the production or extraction of energy by buoyancy. Figure 2.10 shows the change of this buoyancy term with $\overline{Ri}$. In weakly stable conditions, the buoyancy works so as to extract turbulence energy. However, in extremely stable stratification it contributes to the production of $\overline{v^2}$. The increasing energy of $\overline{v^2}$ due to the positive buoyancy term may be redistributed to $\overline{u^2}$ through the pressure-force term and may result in the peak of u'/u* at about y/δ=0.6.

Figure 2.11 shows the distributions of the r.m.s. value of the lateral velocity fluctuation,w'. The decrease of w'/u* with stability shows that the lateral turbulence is suppressed in stable conditions.

Figure 2.12 shows the distributions of the r.m.s. value of the temperature fluctuation normalized by the temperature difference, i.e., $\theta'/(\overline{T}_{suf}-\overline{T}_{bot})$. It may be seen that $\theta'/(\overline{T}_{suf}-\overline{T}_{bot})$ decreases in the stable surface region and that the peak of the distribution moves inward from the free surface with increasing stability. Such

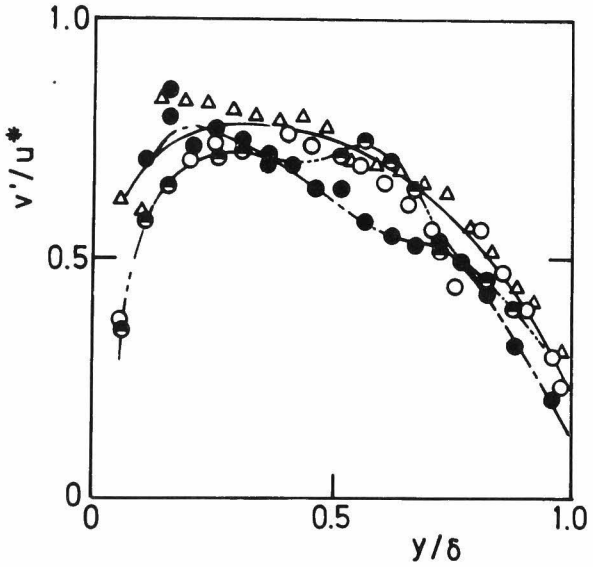

Figure 2.9. Distributions of the r.m.s. values of vertical velocity fluctuations.

△ $\overline{Ri}$ = 0.0 , ○ $\overline{Ri}$ = 2.31×10^{-2} ,

● $\overline{Ri}$ = 1.53×10^{-1} , ◓ $\overline{Ri}$ = 2.63×10^{-1} .

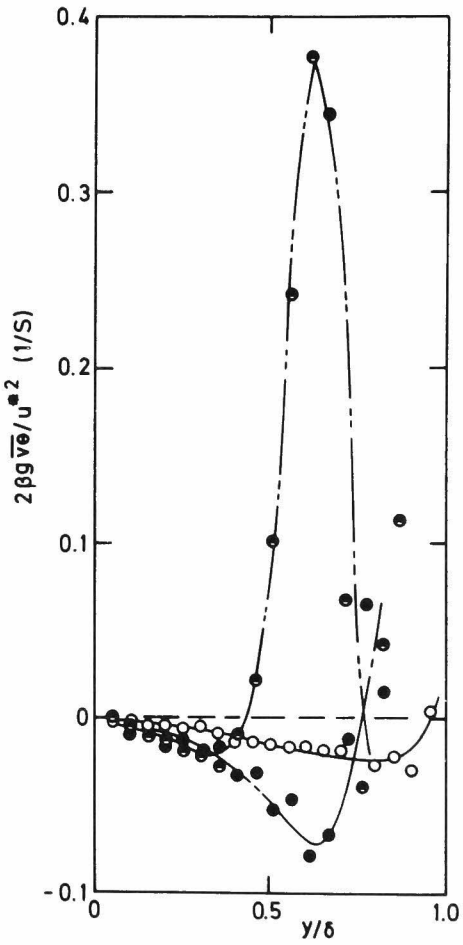

Figure 2.10. Distributions of the buoyancy term, $2\beta g\overline{v\theta}/u^{*2}$.
Symbols as in figure 2.9.

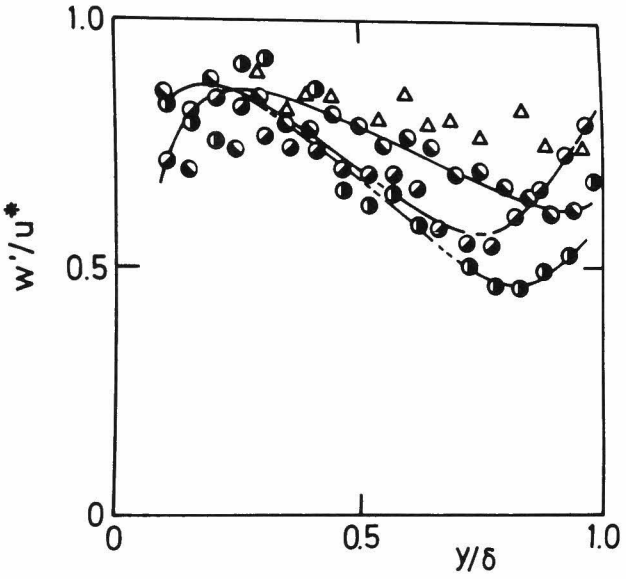

Figure 2.11. Distributions of the r.m.s. values of lateral velocity fluctuations.

△ $\overline{Ri}$ = 0.0 , ◔ $\overline{Ri}$ = 1.35×10^{-2} ,

◑ $\overline{Ri}$ = 1.90×10^{-1} , ◑ $\overline{Ri}$ = 2.69×10^{1} .

behavior may be explained by using the following transport equation of $\overline{\theta^2}$,

$$\frac{D\overline{\theta^2}}{Dt} = -2\overline{v\theta}\frac{\partial\overline{T}}{\partial y} - 2K\overline{\frac{\partial\theta}{\partial x_k}\frac{\partial\theta}{\partial x_k}} - \frac{\partial}{\partial x_k}[\overline{u_k\theta^2} - K\frac{\partial\overline{\theta^2}}{\partial x_k}], \qquad (2\text{-}3)$$

where K is the thermal diffusivity.
The distribution of the production term, $-2\overline{v\theta}(\partial\overline{T}/\partial y)/(\overline{T}_{suf}-\overline{T}_{bot})^2$, are shown in figure 2.13. The production term makes a positive contribution to $\overline{\theta^2}$ in a weakly stable flow(Run III), but in a strongly stable flow(Run VIII) it makes a negative contribution. This supports the result that $\theta'/(\overline{T}_{suf}-\overline{T}_{bot})$ decreases with increasing stability, as shown in figure 2.12.

Correlation coefficients of the Reynolds stress and heat fluxes

Figure 2.14 shows the distributions of the correlation coefficient of the Reynolds stress, $R_{uv} = -\overline{uv}/u'v'$.
The correlation coefficient, R_{uv}, decreases with increasing $\overline{Ri}$ and ultimately becomes negative in a strongly stable flow(Run VIII). The change of the sign is striking, that is, the turbulent transport of momentum occurs against the time-averaged velocity gradient. Here again it may be explained by taking into account the buoyancy term of the transport equation of $-\overline{uv}$,

$$\frac{D(-\overline{uv})}{Dt} = \overline{v^2}\frac{\partial\overline{U}}{\partial y} - \beta g\overline{u\theta} - 2\nu\overline{\frac{\partial u}{\partial x_k}\frac{\partial v}{\partial x_k}} + \overline{\frac{p}{\rho}(\frac{\partial u}{\partial y} + \frac{\partial v}{\partial x})} - \frac{\partial}{\partial x_k}[\overline{uvu_k}$$

$$\nu\frac{\partial\overline{uv}}{\partial x_k} + \delta_{1k}\overline{\frac{vp}{\rho}} + \delta_{2k}\overline{\frac{up}{\rho}}], \qquad (2\text{-}4)$$

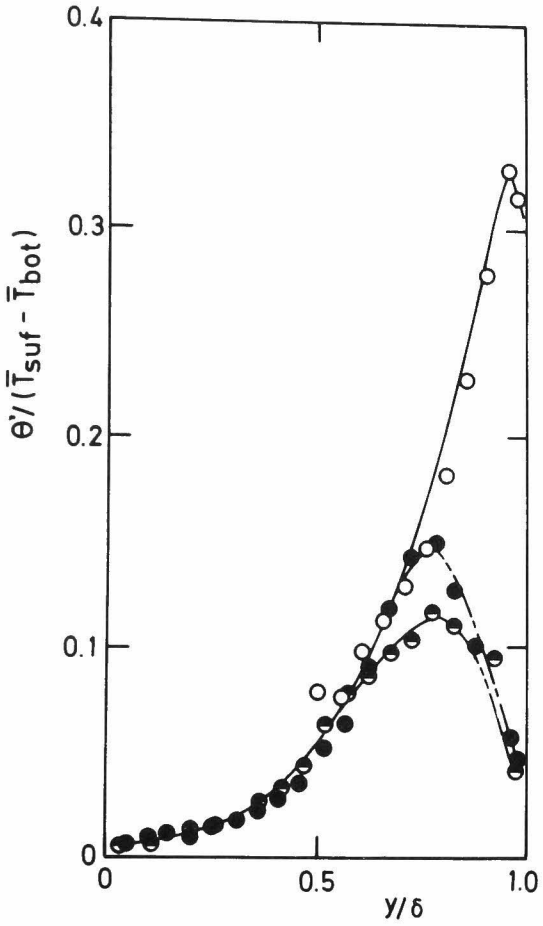

Figure 2.12. Distributions of the r.m.s. values of temperature fluctuations.
○ $\overline{Ri}$ = 2.31×10^{-2} , ● $\overline{Ri}$ = 1.53×10^{-1} ,
◓ $\overline{Ri}$ = 2.63×10^{-1}.

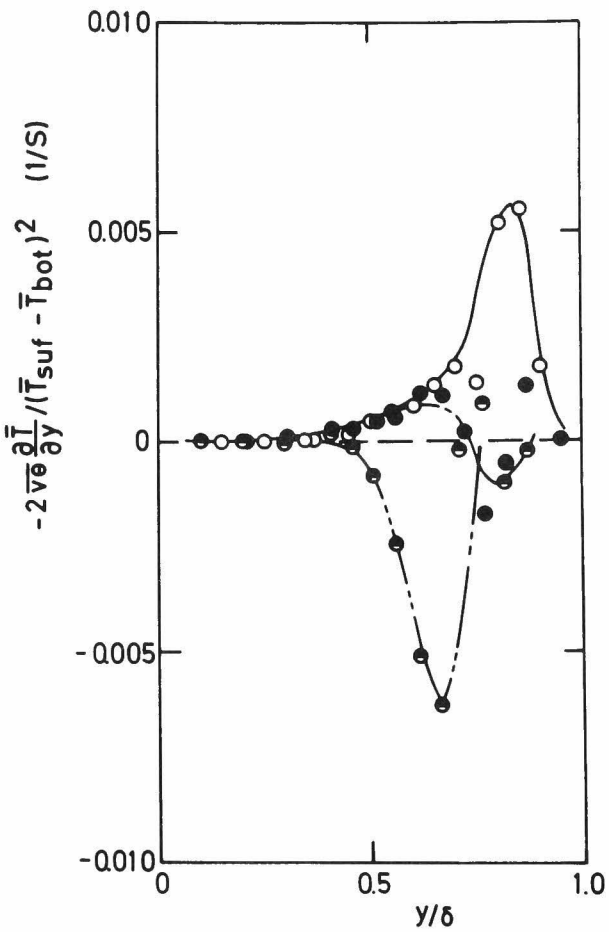

Figure 2.13. Distributions of the production term, $-2\overline{v\theta}(\partial\overline{T}/\partial y)/(\overline{T}_{suf}-\overline{T}_{bot})^2$. Symbols as in figure 2.12.

The distributions of the buoyancy term are shown in figure 2.15. The buoyancy term makes a negative contribution and reduces R_{uv} with increasing stability. The change of the sign of R_{uv} will be discussed briefly in subsection 2.3.2.

Figure 2.16 shows the distributions of the correlation coefficient of the streamwise heat flux, $R_{u\theta} = \overline{u\theta}/u'\theta'$. With increasing stability, the correlation coefficient, $R_{u\theta}$, increases in the region of $y/\delta \lesssim 0.6$ and decreases near the free surface. This is also related to the behavior of the production term in the transport equation of $\overline{u\theta}$,

$$\frac{D\overline{u\theta}}{Dt} = [\overline{uv}\frac{\partial\overline{T}}{\partial y} + \overline{v\theta}\frac{\partial\overline{U}}{\partial y}] \quad (K + \nu)\overline{\frac{\partial\theta}{\partial x_k}\frac{\partial u}{\partial x_k}} + \overline{\frac{p}{\rho}\frac{\partial\theta}{\partial x}}$$

$$\frac{\partial}{\partial x_k}[\overline{uu_k\theta} + \overline{\frac{p\theta}{\rho}}\,\delta_{1k}] \qquad (2\text{-}5)$$

The behavior of the production term can be clearly seen in figure 2.17.

Figure 2.18 shows the distributions of the correlation coefficient of the vertical heat flux, $R_{v\theta} = -\overline{v\theta}/v'\theta'$. The correlation coefficient, $R_{v\theta}$, decreases remarkably with increasing stability and ultimately becomes negative in strongly stable conditions. Similar behavior was observed in the distribution of R_{uv}, but in this case a negative correlation is more obvious and larger amounts of heat may be transferred against the mean temperature gradient. This can be attributed to the large increases of the buoyancy term(see figure 2.19) in the transport equation of $-\overline{v\theta}$,

$$\frac{D(-\overline{v\theta})}{Dt} = \overline{v^2}\frac{\partial\overline{T}}{\partial y} - \beta g\overline{\theta^2} + (K + \nu)\overline{\frac{\partial\theta}{\partial x_k}\frac{\partial v}{\partial x_k}} + \overline{\frac{p}{\rho}\frac{\partial\theta}{\partial y}} \quad \frac{\partial}{\partial x_k}[\overline{vu_k\theta}$$

$$+ \overline{\frac{p\theta}{\rho}}\,\delta_{2k}]. \qquad (2\text{-}6)$$

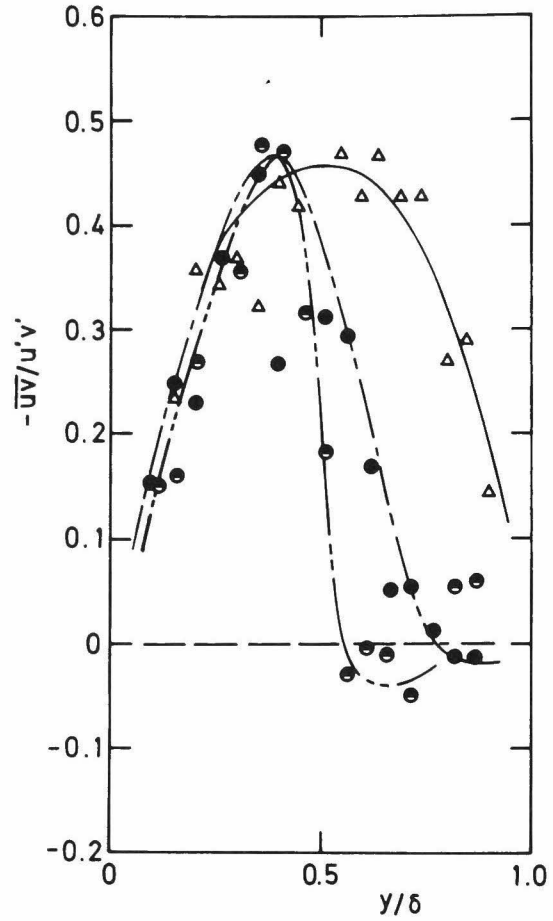

Figure 2.14. Distributions of the correlation coefficient of the Reynolds stress.
△ $\overline{Ri}$ = 0.0 , ● $\overline{Ri}$ = 1.53×10^{-1} ,
◓ $\overline{Ri}$ = 2.63×10^{-1}.

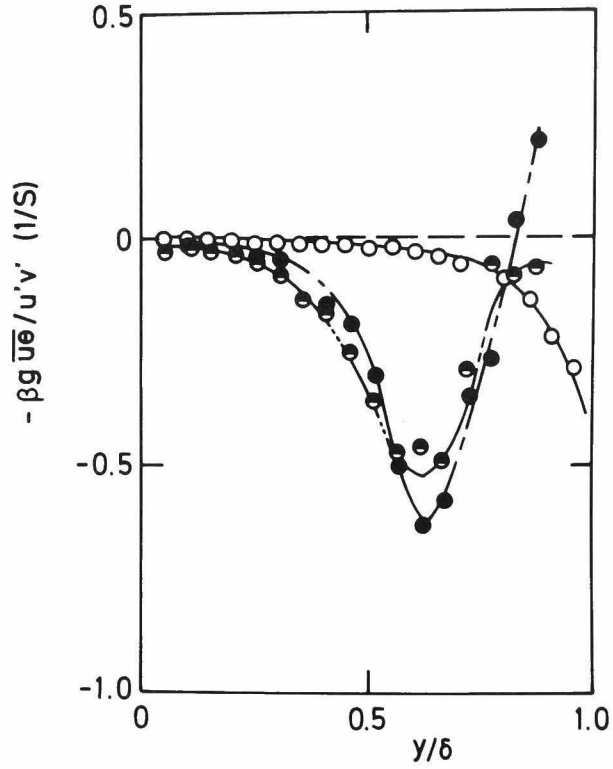

Figure 2.15. Distributions of the buoyancy term, $-\beta g\overline{u\theta}/u'v'$.
○ $\overline{Ri}$ = 2.31×10^{-2} , ● $\overline{Ri}$ = 1.53×10^{-1}
◓ $\overline{Ri}$ = 2.63×10^{-1} .

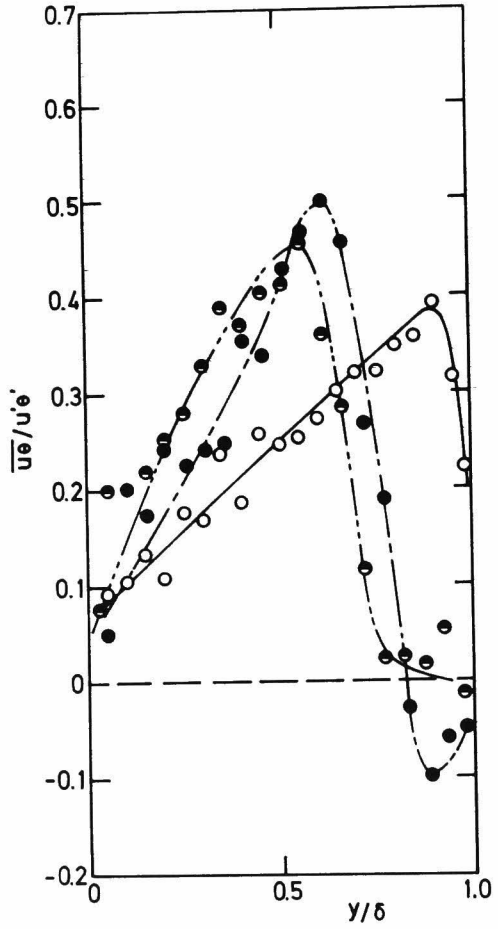

Figure 2.16. Distributions of the correlation coefficient of the streamwise heat flux.

○ $\overline{Ri}$ = 2.31×10^{-2} , ● $\overline{Ri}$ = 1.53×10^{-1} ,

◓ $\overline{Ri}$ = 2.63×10^{-1}

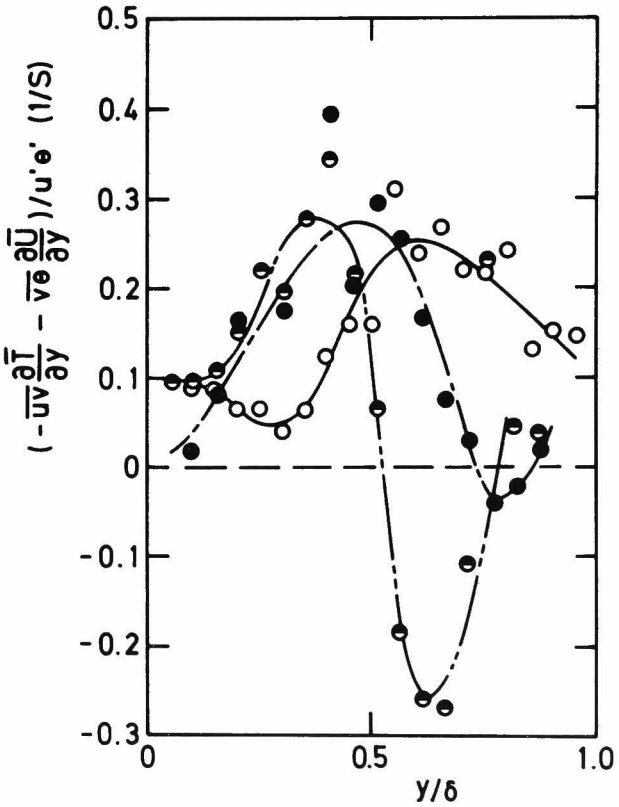

Figure 2.17. Distributions of the production term, $(-\overline{uv}\partial\overline{T}/\partial y - \overline{v\theta}\partial\overline{U}/\partial y)/u'\theta'$. Symbols as in figure 2.16.

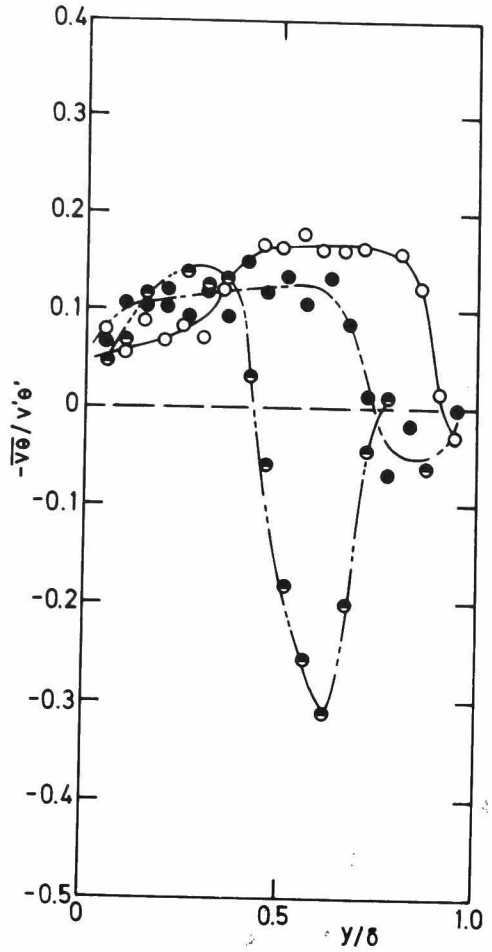

Figure 2.18. Distributions of the correlation coefficient of the vertical heat flux.
○ $\overline{Ri}$ = 2.31x10^{-2} , ● $\overline{Ri}$ = 1.53x10^{-1} ,
◓ $\overline{Ri}$ = 2.63x10^{-1} .

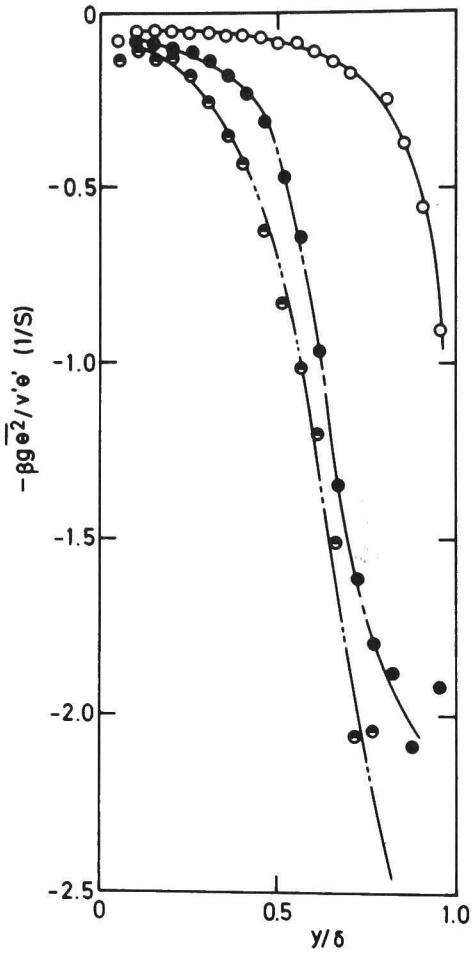

Figure 2.19. Distributions of the buoyancy term, $-\beta g\overline{\theta^2}/v'\theta'$.
Symbols as in figure 2.18.

The change of the sign of $R_{v\theta}$ will be also discussed in subsection 2.3.2.

Turbulence kinetic energy

The turbulence kinetic energy balance equation for two-dimensional stratified flow with high Reynolds number, in which the work by the viscous shear stresses of the turbulent motion can be neglected, is given by

$$\frac{\overline{Dq^2/2}}{Dt} = -\overline{uv}\frac{\partial \overline{U}}{\partial y} + \beta g \overline{v\theta} \quad \frac{\partial}{\partial y}\overline{[v(\frac{p}{\rho} + \frac{q^2}{2})]} \quad \overline{\nu(\frac{\partial u_i}{\partial x_j} + \frac{\partial u_j}{\partial x_i})\frac{\partial u_j}{\partial x_i}} \quad , \quad (2\text{-}7)$$

where $\overline{q^2}=\overline{u^2}+\overline{v^2}+\overline{w^2}$. The first term on the right is the turbulent shear energy production term, the second the buoyancy energy production term, the third the diffusion term, and the last is the viscous dissipation term.

The energy dissipation was estimated from the spectral density of the streamwise velocity fluctuation using the Kolmogoroff hypothesis for the inertial subrange, i.e.,

$$S_{uu}(k) = \chi \varepsilon^{2/3} k^{5/3} \quad (2\text{-}8)$$

where ε is the viscous dissipation and k is the wave number defined by $k=2\pi f/\overline{U}$ (f: the frequency). The value of $\chi = 0.517$, suggested by Gibson[24], was used in this estimation. When the shear production, buoyancy production and viscous dissipation are known, we can calculate the diffusion of energy from equation(2-7) on the assumption that the flow is steady and well-developed, that is, when the convection term in equation(2-7) can be ignored. However, since

the present stable flows are not strictly well-developed, the diffusion term calculated from equation(2-7) should be considered as the diffusion term involving small convection. It should also be noted that the conclusions derived from equation(2-7) are of a more or less qualitative nature because of the approximations involved in the calculations of the dissipation.

Each term in equation(2-7) is made dimensionless by δ/u^{*3} and plotted against y/δ in figures 2.20, 2.21 and 2.22 for two stable flows(Run VIII and Run V) and a neutral flow(Run I), respectively.

In the strongly stable flow(Run VIII) the production by mean shear is reduced significantly with the distance from the wall and goes to zero in the region of $y/\delta \gtrsim 0.7$. In the region near $y/\delta=0.6$ the shear production term makes a negative contribution. The buoyancy production term makes a large positive contribution in the thin layer from $0.45 \lesssim y/\delta \lesssim 0.75$ in which the correlation coefficient of the vertical heat flux, $R_{v\theta}$, has a negative value as shown in figure 2.18. In the range of $y/\delta \gtrsim 0.75$ the production by buoyancy becomes substantially zero, and a wavelike motion appears which will be discussed in subsection 2.3.2. The energy dissipation decreases near the free surface and has small peak at the position where the production by buoyancy has a maximum value. From the distribution of the diffusion term it can be seen that the energy produced by mean shear in the lower region of $y/\delta \lesssim 0.5$ is diffused into both the upper region of $y/\delta \gtrsim 0.5$ and the wall region of $y/\delta \lesssim 0.2$.

In the moderately stable flow(Run V) shown in figure 2.21 the shear production term makes a positive contribution and is almost balanced by the dissipation. The buoyancy production term makes a negative contribution in the whole range of y/δ. A change of the sign of the production terms as is seen in figure 2.20 does not appear in this flow. The diffusion term shows the diffusion of the

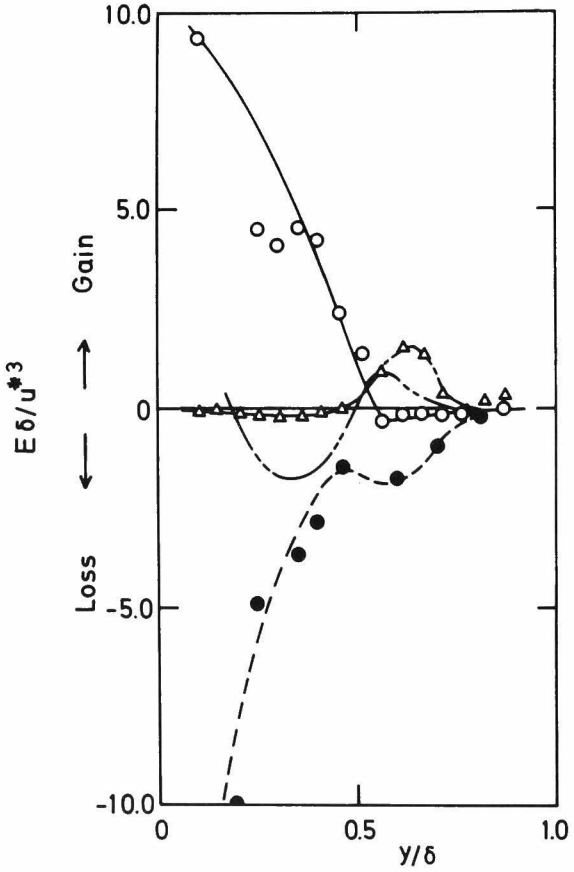

Figure 2.20. Turbulence kinetic energy balance.
(in a strongly stable flow)
Run VIII

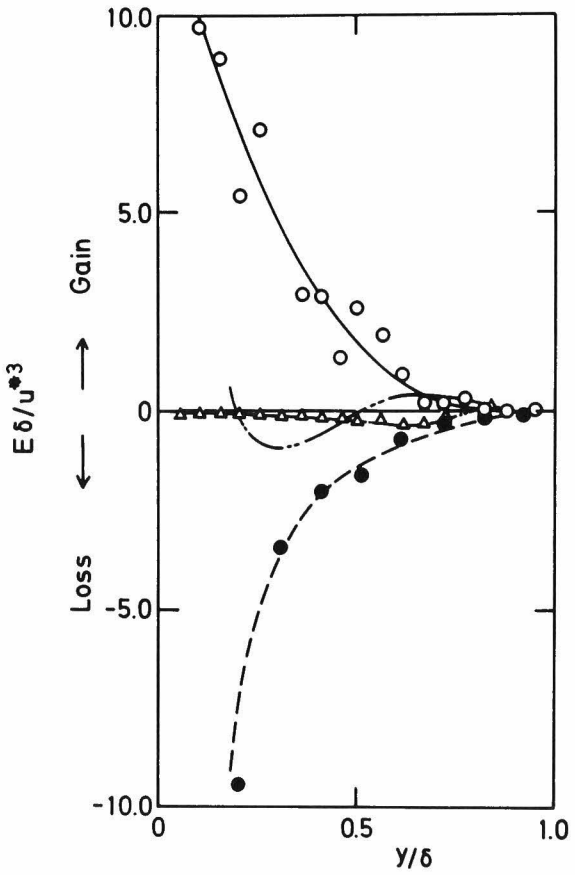

Figure 2.21. Turbulence kinetic energy balance.
(in a moderately stable flow)
Run V

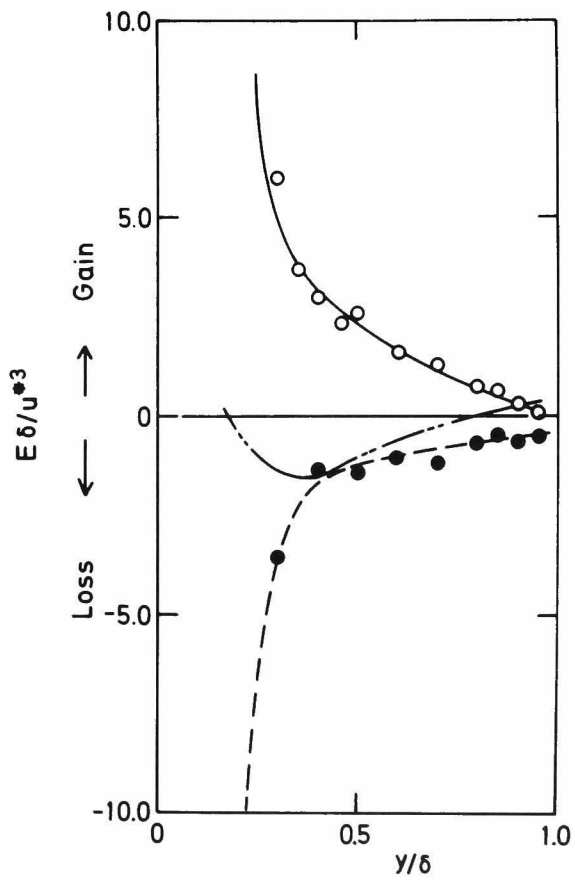

Figure 2.22. Turbulence kinetic energy balance.
(in a neutral flow)
Run I

—○— shear production, —·—△—·— buoyancy production, — — ● — — dissipation, ——··—— diffusion.

energy produced by mean shear toward both the upper region and the region adjacent to the wall.

In the neutral flow(Run I) shown in figure 2.22, the shear production term is larger than those shown in figures 2.20 and 2.21, and the energy is diffused toward both the free surface region of $y/\delta \gtrsim 0.8$ and the region near the wall.

It should be noted that the diffusion term depicted in figures 2.20 to 2.22 involves the effect of the transport of energy by pressure force which is difficult to measure. However, the vertical flux of the turbulent kinetic energy, $\overline{vq^2}$, can be calculated on the assumption that $\overline{vq^2} \simeq \overline{v(u^2+2v^2)}$.

Figures 2.23 and 2.24 show the distributions of the vertical flux in a strongly stable flow(Run VIII) and a neutral flow(Run I), respectively. The vertical energy flux is positive in the entire region except near the free surface and the wall region, and has a sharp peak in the region of $0.2 \lesssim y/\delta \lesssim 0.3$, in both the strongly stable and the neutral flow cases. This means that the turbulence kinetic energy produced by shear is transferred upward into the entire region. In the strongly stable flow, a blunt secondary peak appears in the region near $y/\delta=0.6$. It may be due to the large amount of the buoyancy production shown in figure 2.20.

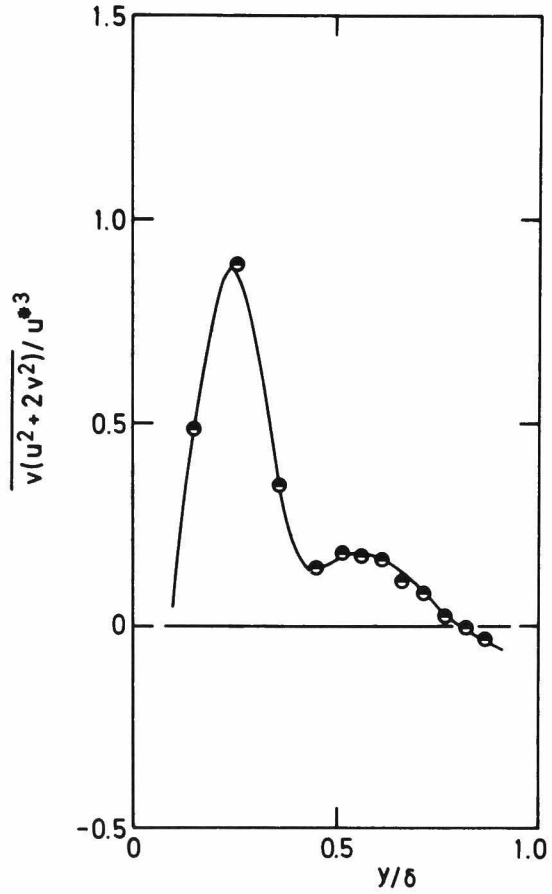

Figure 2.23. Distributions of the vertical flux of turbulence kinetic energy. (in a strongly stable flow, Run VIII)

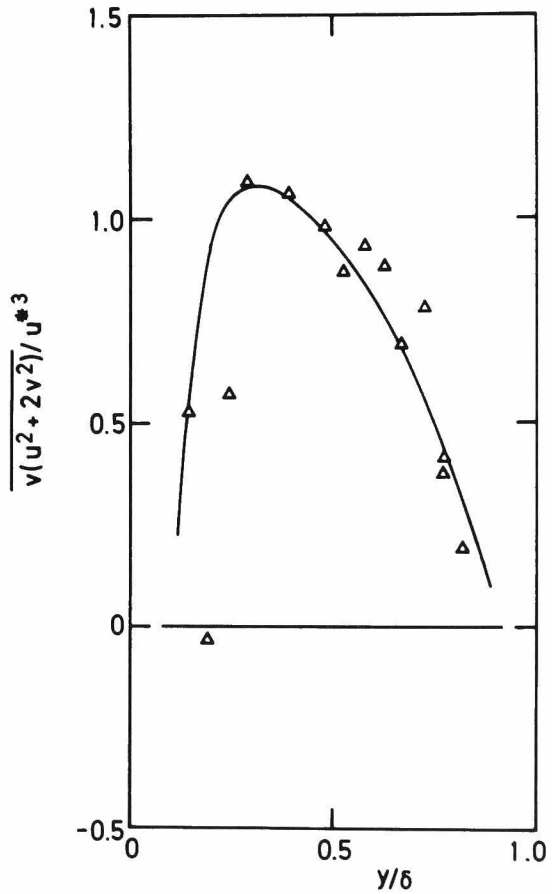

Figure 2.24. Distributions of the vertical flux of turbulence kinetic energy. (in a neutral flow, Run I)

2.3.2 Turbulence structure

Probability density distributions, skewness and flatness factors

Figures 2.25, 2.26 and 2.27 show the probability density functions of the streamwise and vertical velocity fluctuations and temperature fluctuations at four positions in a strongly stable flow(Run VIII). The probability density, $P\sigma$, of a random variable $\sigma(t)$ is normalized as

$$\int_{-\infty}^{\infty} P\sigma(\sigma/(\overline{\sigma^2})^{1/2})\,d(\sigma/(\overline{\sigma^2})^{1/2}) = 1.$$

The probability density functions of u and v, i.e., Pu and Pv, are approximately symmetrical in shape, and it is surprising that those functions hardly change from those in the neutral case which shows a shape similar to that obtained in a pipe (Ueda & Mizushina,[25])... In contrast with these facts, the probability density function of θ, P_θ, departs greatly from normality.

The change of the probability density functions with stability may be seen more clearly by introducing the skewness factor $S(\sigma)$ and the flatness factor $F(\sigma)$. Those are defined as the third and the fourth moments of $P\sigma$ and calculated by $S(\sigma) = \overline{\sigma^3}/(\overline{\sigma^2})^{3/2}$ and $F(\sigma) = \overline{\sigma^4}/(\overline{\sigma^2})^2$, respectively.

Figures 2.28, 2.29 and 2.30 compare the distributions of these moments for different degrees of stability, i.e., for a weakly stable flow(Run III) and a strongly stable flow(Run VIII). For the normal probability the flatness and the skewness factor are 3.0 and 0.0, respectively, and are drawn as the dashed lines in those figures. As seen in the probability density functions of θ, both the skewness and the flatness factors of the temperature fluctuation deviate greatly from the values for normal probability. Large values of $F(\theta)$ in the lower part of the flow were attributed to the intermittent

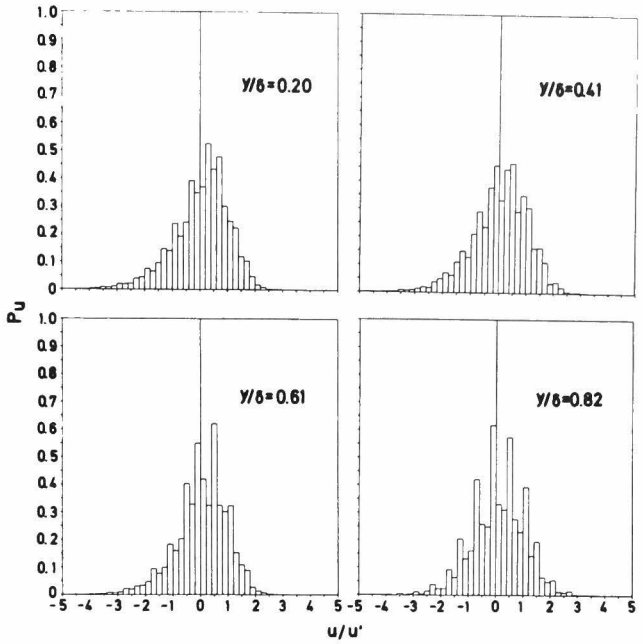

Figure 2.25. Probability density function of streamwise velocity fluctuations. (Run VIII)

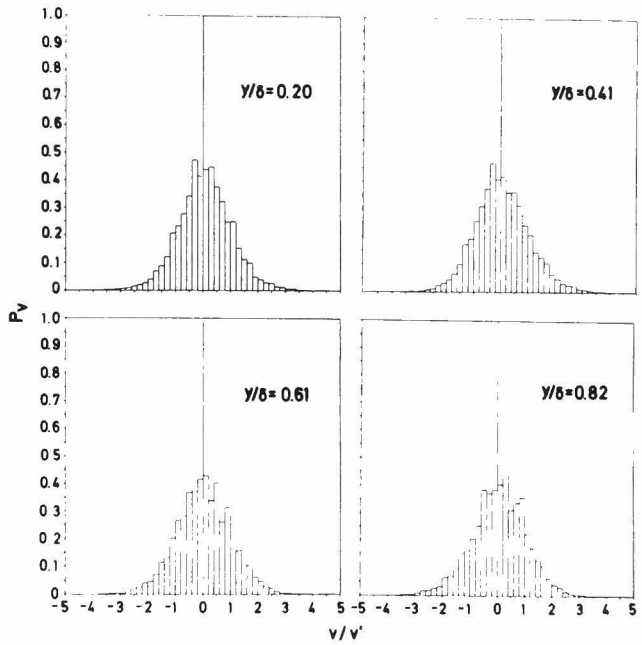

Figure 2.26. Probability density function of vertical velocity fluctuations. (Run VIII)

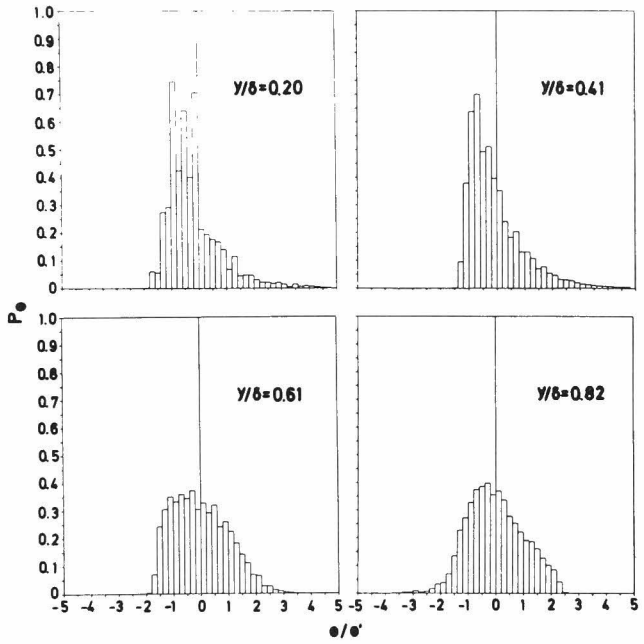

Figure 2.27. Probability density function of temperature fluctuations. (Run VIII)

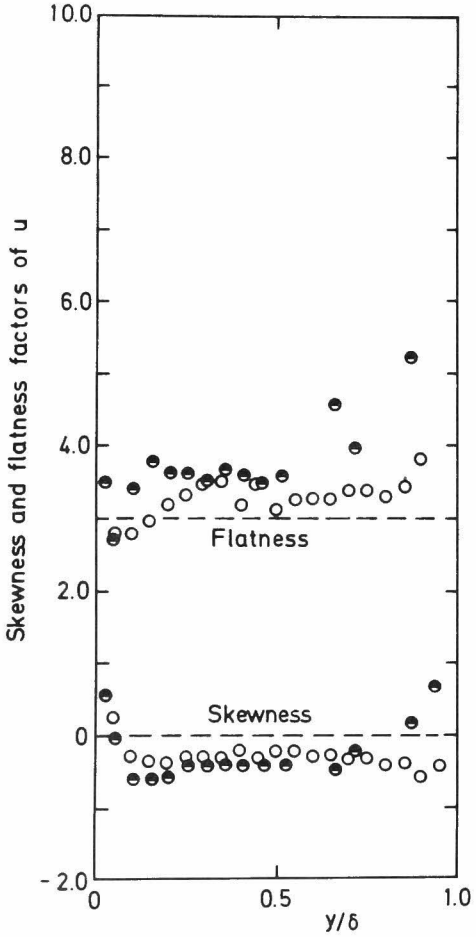

Figure 2.28. Skewness and flatness factors of streamwise velocity fluctuations.

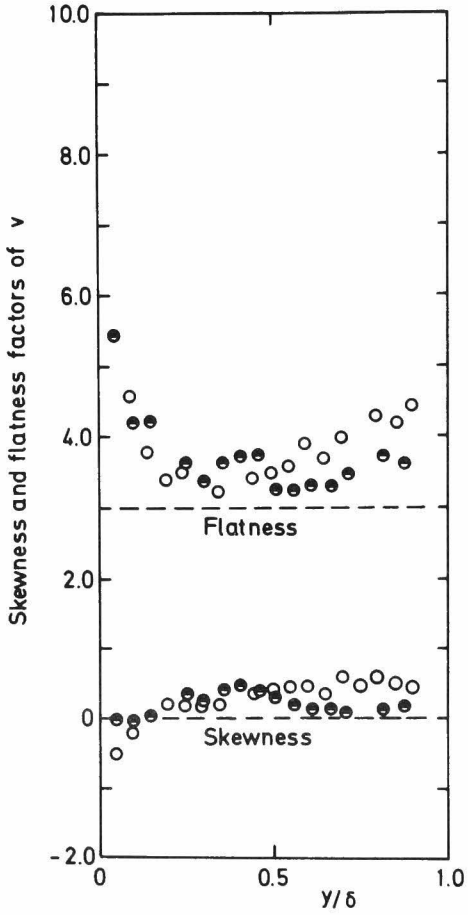

Figure 2.29. Skewness and flatness factors of vertical velocity fluctuations.

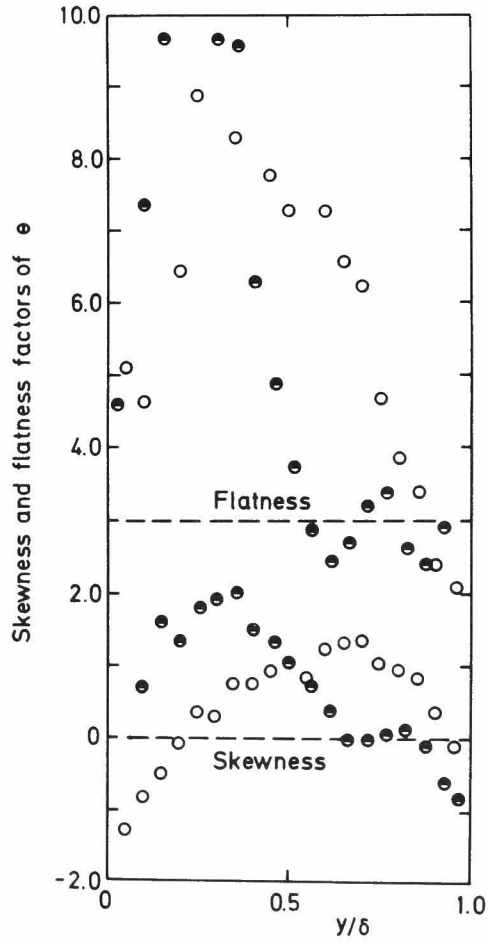

Figure 2.30. Skewness and flatness factors of temperature fluctuations.

○ $\overline{Ri} = 2.31 \times 10^{-2}$, ◓ $\overline{Ri} = 2.63 \times 10^{-1}$.

nature of the temperature fluctuation, which was first pointed out by Batchelor & Townsend[26].

Figure 2.31 shows the records of the temperature fluctuation at various positions from the wall. In the lower part hot spots appear intermittently and are presumed to be the finger-like motions observed visually by Linden[27].

In the strongly stable region of $y/\delta \gtrsim 0.7$ of Run VIII, $F(\theta)$ and $S(\theta)$ approach the normal values. There, $F(v)$ and $S(v)$ are also close to 3.0 and 0.0, respectively. As seen in figure 2.31, the record of the temperature fluctuation in the upper region of $y/\delta \gtrsim 0.7$ has no remarkable spike at all and suggests the presence of wavelike motions as will be discussed subsequently(also see Willis & Deardorff [28] and La Fond[29]).

Joint probability density functions

The joint probability density, $P\sigma_1\sigma_2$, of random variables $\sigma_1(t)$ and $\sigma_2(t)$ is such that the following integral

$$\int_{-\infty}^{\infty}\int_{-\infty}^{\infty} P\sigma_1\sigma_2(\sigma_1/(\overline{\sigma_1^2})^{1/2},\sigma_2/(\overline{\sigma_2^2})^{1/2})\, d(\sigma_1/(\overline{\sigma_1^2})^{1/2})\, d(\sigma_2/(\overline{\sigma_2^2})^{1/2})$$

is equal to unity.

Puv, Pvθ and Puθ are calculated for a strongly stable flow (Run VIII) and shown in figures 2.32, 2.33 and 2.34, respectively. The outermost and innermost rings delineate the probability of occurrences of 0.01 and 0.20, respectively. The distributions of Puv at $y/\delta=0.26$ and 0.46 are similar to those obtained by Ueda & Mizushina[25] in the fully turbulent region of pipe flow. In the upper region where local stability is very large, Puv becomes more circular. This is in accordance with the reduced correlation between

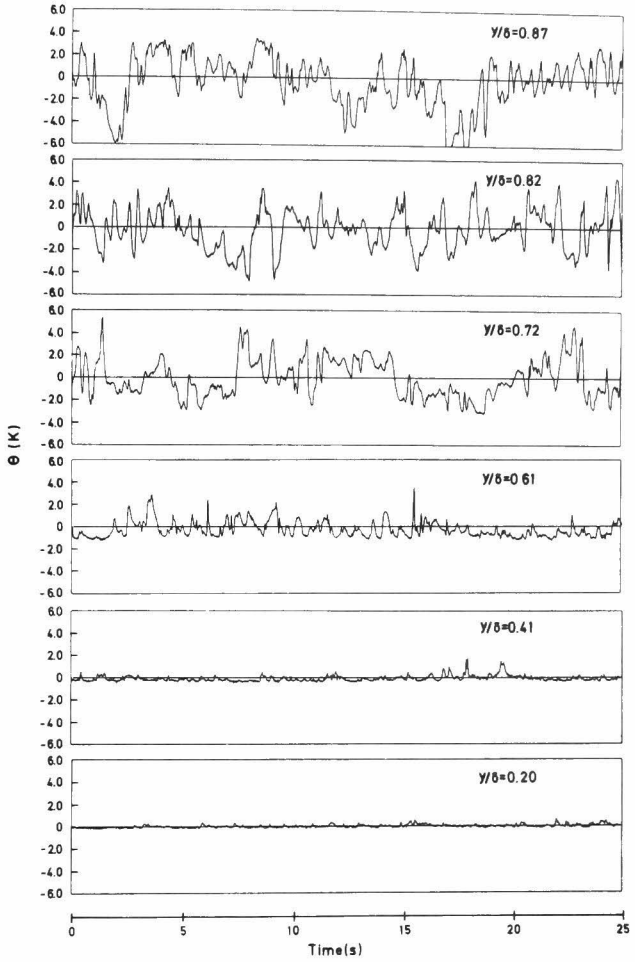

Figure 2.31. Records of temperature fluctuations in a strongly stable flow. (Run VIII)

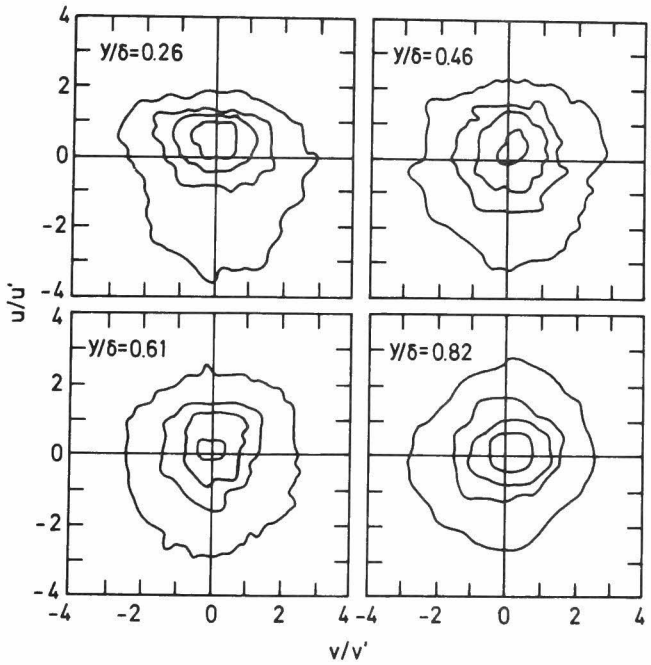

Figure 2.32. Joint probability density functions of u and v. (Run VIII)

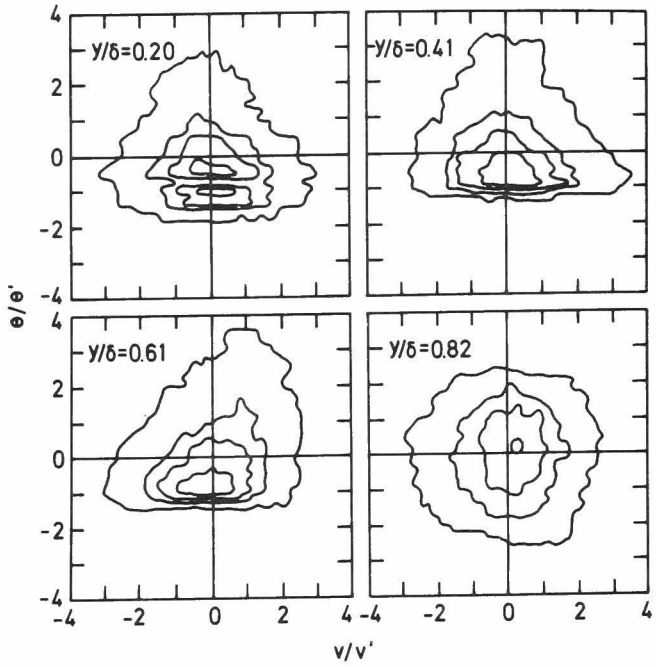

Figure 2.33. Joint probability density functions of v and θ. (Run VIII)

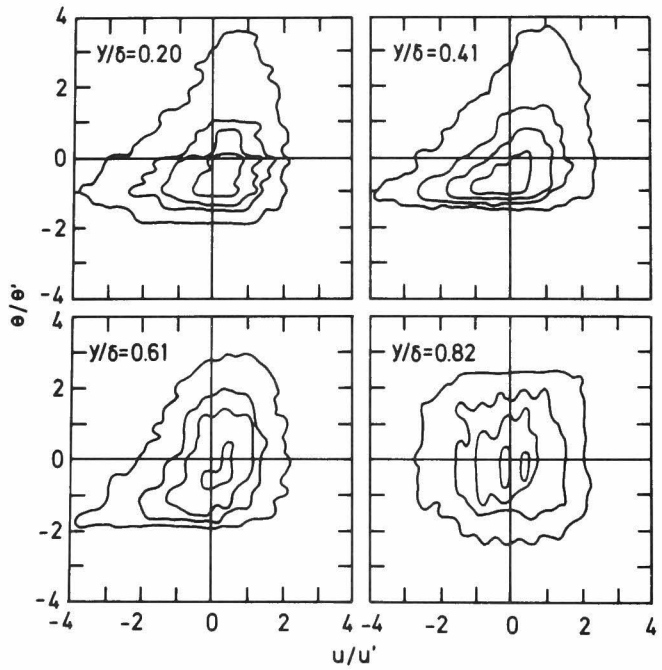

Figure 2.34. Joint probability density functions of u and θ. (Run VIII)

u and v. Such a circular shape is also seen in the joint probability density functions of v and θ at the position of $y/\delta=0.82$.

Since the probability density distribution of θ is so skewed, the joint probability density functions of u-θ and v-θ deviate greatly from normality. Because of the strong stability heat is hardly transferred into the lower region and the time-averaged temperature is almost uniform in the region of $y/\delta \lesssim 0.6$. Thus, temperature fluctuations with negative sign are limited there, whereas positive temperature fluctuations associated with the spikes of temperature fluctuation as shown in figure 2.31 are large. It is surprising that the area under the outermost ring in the region of $\theta>0$ and $v>0$ spreads at $y/\delta=0.61$ and most of the large spikes in the time record of the temperature in figure 2.31 have higher temperatures than the time-averaged temperatures in the somewhat upper region.
This means that the eddies with high temperatures may intermittently rise due to positive buoyancy force, and this intermittent motion may be due to the breakdown of the wavelike motion by shear instability.

Here, the question arises as to where such eddies come from, that is, how are such high temperature fluctuations generated ?
The detailed mechanism will be discussed in the subsequent paragraph.

Phase angle and coherence

Stewart[18], Bretherton[30], Pao[17], McBean & Miyake[6] and others have suggested that internal wave motions and turbulence co-exist in a stably stratified flow. To distinguish between turbulence and internal waves they used the velocity-temperature coherence-phase relationships. Indeed, the most promising sorting technique available is to analyze the phase angle with vertical velocity-temperature coherence. In the wave motions the v-θ coherence should

be high and the phase angle should be equal to $\pm\pi/2$, while the fully turbulent motion has a phase angle of either near zero or near $\pm\pi$(Stewart[18] and McBean & Miyake[6]).

Figure 2.35 shows the v-θ phase angles and coherences as a function of wavenumber k for four positions in a strongly stable flow(Run VIII). The phase angles at $y/\delta=0.20$ are near $-\pi$ except for the range of high wavenumbers. This means that the turbulent motions predominate in the lower region. Plates 2.1 and 2.2, obtained by hydrogen bubble technique, support this fact.

In the upper region of $y/\delta \gtrsim 0.8$, the phase angles are approximately $-\pi/2$ and the coherences become somewhat higher in the extended region of the wavenumber, i.e., $k \lesssim 10^2$. Here, the wavenumber of $k=10^2$ corresponds to the Väisälä frequency $N=(\beta g \partial\overline{T}/\partial y)^{1/2}$, which is the upper limit of the frequency of the internal waves and is shown by the arrow in figure 2.35. These phase-coherence relationships suggest that the wavelike motions become predominant in the upper region. This was also confirmed by flow visualization, as shown in plate 2.1, in which the flow pattern of the wavelike motions without vertical mixing can be clearly recognized.

In the intermediate region of $y/\delta \simeq 0.6$, the phase angles approach zero in the low wavenumber region and coherences become extremely high. These high coherences without phase shift are mainly attributed to the intermittent spikes of the temperature fluctuation which may be caused by the breakdown of the wavelike motions shown in plate 2.2. This breakdown intermittently appears in the stable region of $0.5 \lesssim y/\delta \lesssim 0.8$ where the time-averaged temperature gradients begin to increase rapidly.

Figure 2.36 shows the u-θ phase angles and coherences. In the upper region of $y/\delta \gtrsim 0.8$ where the wavelike motions are predominant, the streamwise velocity fluctuation has so small correlation with the temperature fluctuation that their coherences remain at a low

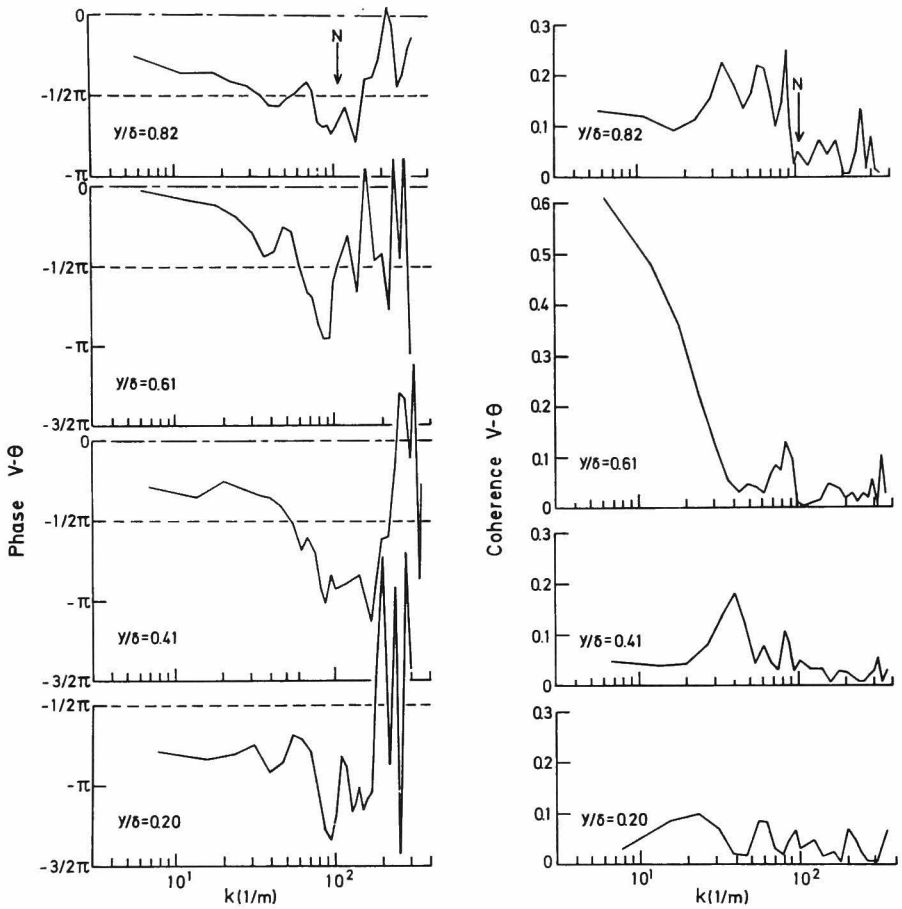

Figure 2.35. v-θ phase angles and coherences. (Run VIII)
N: Vaisala frequency

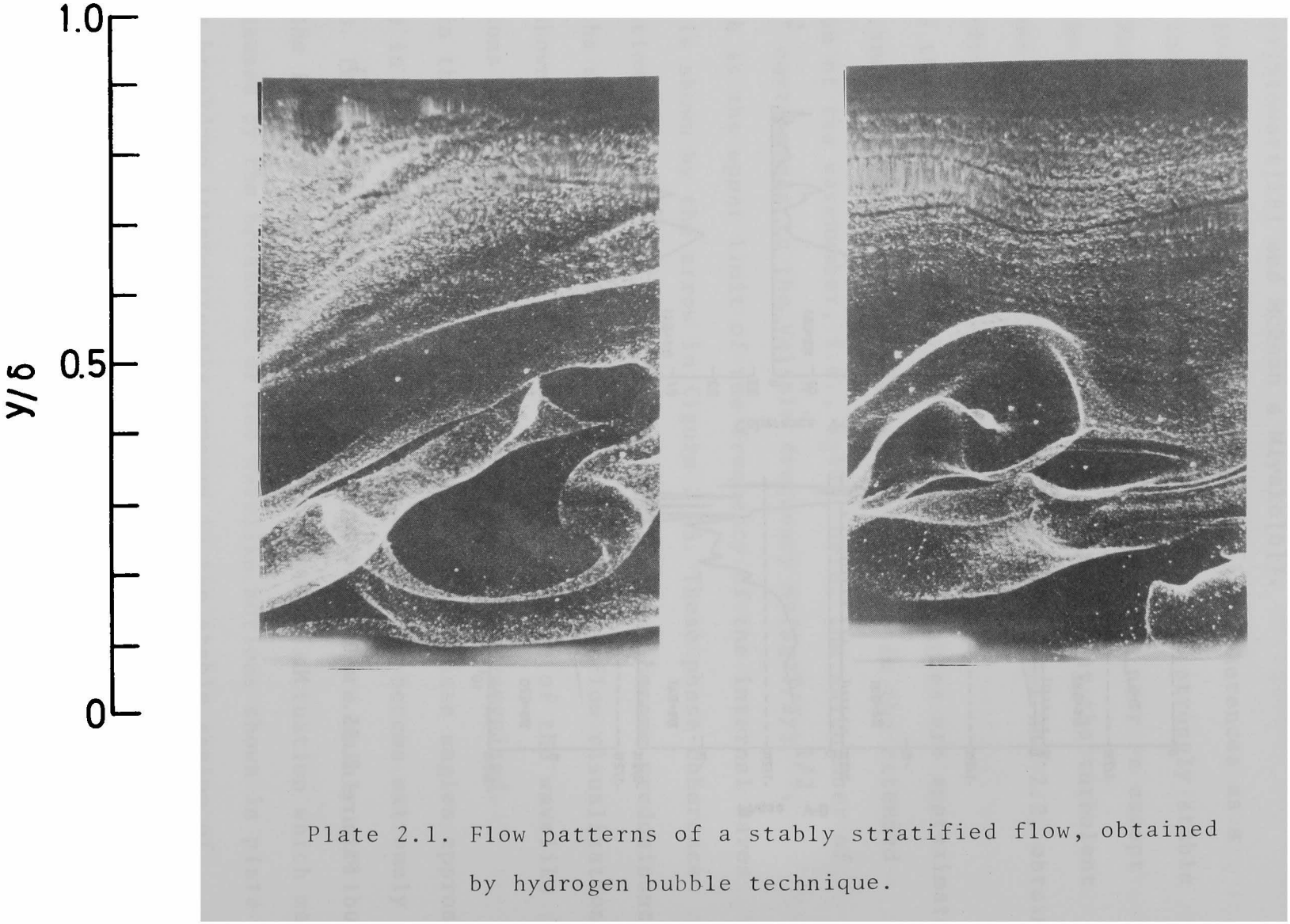

Plate 2.1. Flow patterns of a stably stratified flow, obtained by hydrogen bubble technique.

Plate 2.2. Flow patterns of breakdown of wavelike motion by shear instability, obtained by hydrogen bubble technique.

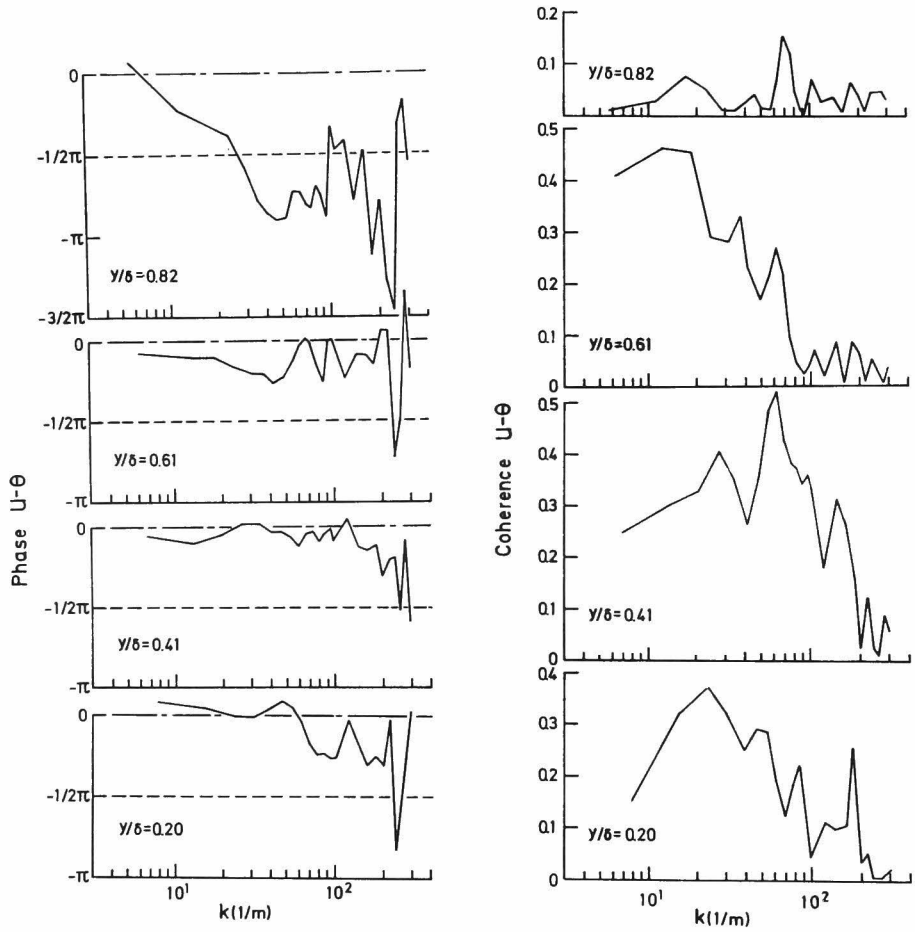

Figure 2.36. u-θ phase angles and coherences. (Run VIII)

level and the phase angles have no constant value. Whereas in the lower region of $y/\delta<0.6$ the coherences are extremely high and the phase angles are almost zero.

The u-v phase angles and coherences are shown in figure 2.37. The phase angles at $y/\delta=0.26$ are near $-\pi$ except for the highest wavenumber region and the coherences are relatively high. This is also a characteristic feature of turbulent motion as suggested by Ueda & Mizushina[25]. At $y/\delta=0.61$, however, very scattered phase angles and low coherences between u and v are observed. This is in contrast to the relationship of v and θ, and suggests that vertical motions of the eddies accompanied with the positive spikes of the temperature fluctuation are not dependent on the streamwise motions.

If the fluid motions consist of linear internal waves, the phase angles must be $\pm\pi/2$ and the coherence must be high. In the upper region of the flow where the wavelike motions are presumed to be dominant the measured phase angles range from 0 to $-\pi/2$ and do not coincide with the values for linear waves. However, the coherence attains to rather high level and the wavenumber region in which these relationships persist extends to $k=10^2$. From this it may be inferred that these wavelike motions are composed of motions with various frequencies below the Väisälä value and induce no vertical mixing, except at the instant of wave breakdown.

Behavior of eddies with large positive spike of temperature fluctuation

Figure 2.38 shows a simultaneous recording of the instantaneous values of θ, v and $v\theta$ at $y/\delta=0.61$ in a strongly stable flow(Run VIII). The θ-signal exhibits intermittent positive spikes. The v-signal

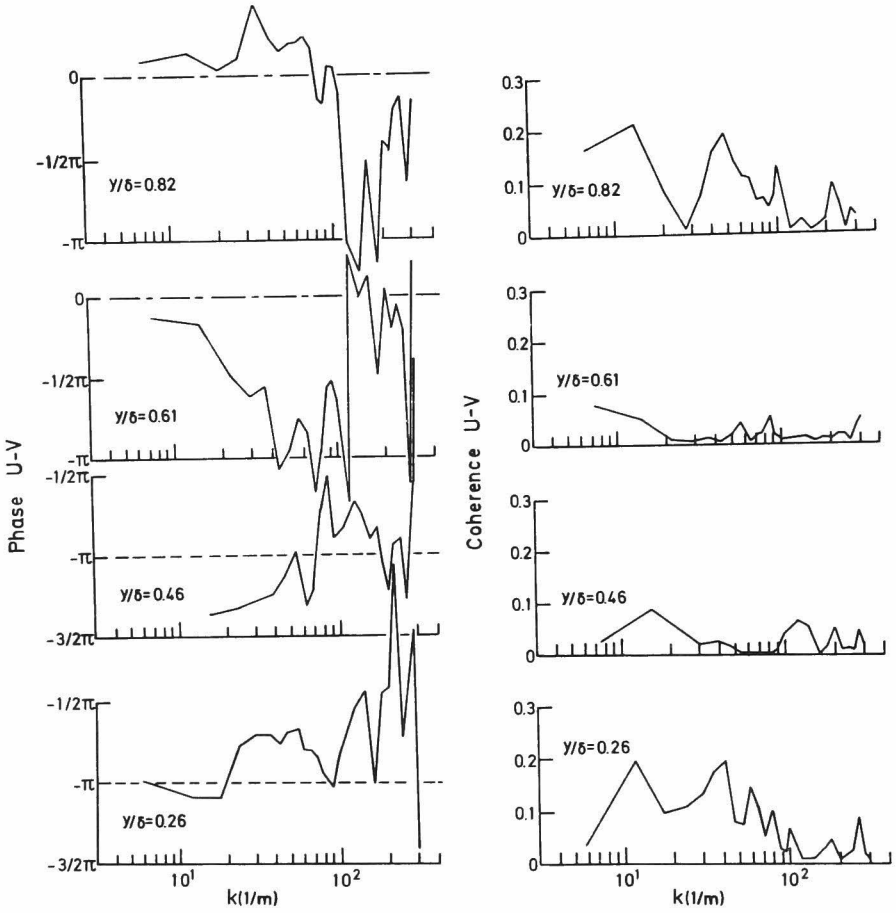

Figure 2.37. u-v phase angles and coherences. (Run VIII)

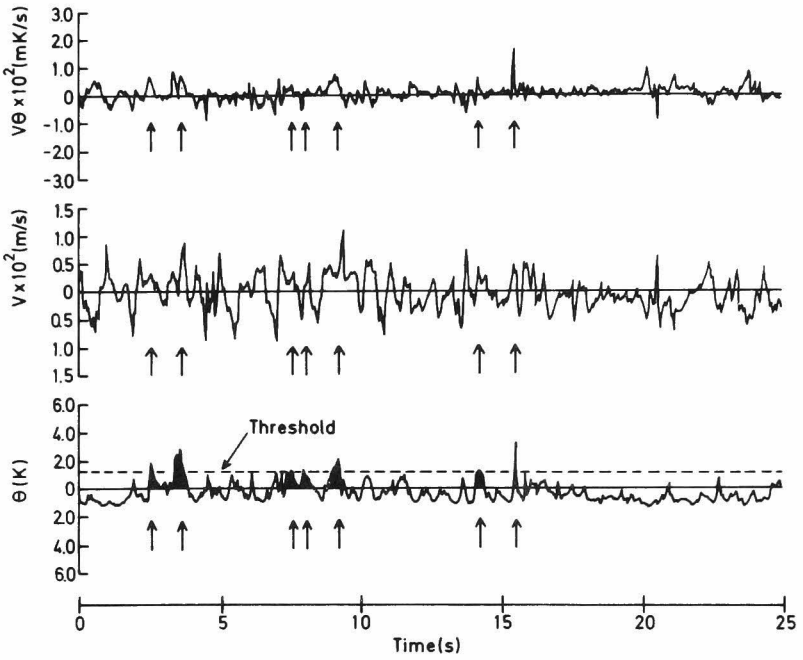

Figure 2.38. Simultaneous recording of the instantaneous values of θ, v and $v\theta$ at $y/\delta=0.61$ in a strongly stable flow. (Run VIII)
dashed line; threshold level for conditional averaging procedure.

looks like a typical turbulence signal, but the positive spikes of θ are accompanied by the positive peaks of v, and result in the positive $v\theta$-products shown by the arrows in the figure. These positive $v\theta$-products cause the upward heat transfer against the time-averaged temperature gradient(see figure 2.18).

In order to show the contribution of the positive $v\theta$-product to the upward heat transfer in the strongly stable flow(Run VIII) more clearly, a threshold level was set with the magnitude of the r.m.s. value of θ in the θ-trace, as shown by a dashed line in the figure. The heat flux due to the intermittent eddies with higher temperature fluctuations than the threshold level, $-\overline{v\theta}_c$, is calculated and plotted in figure 2.39 normalized by $v'\theta'$. Here, the solid circles denote the total heat flux attributable to the whole eddies, that is, the distribution of $-\overline{v\theta}/v'\theta'$ of Run VIII in figure 2.18. It may be seen that in the region near $y/\delta=0.6$, the contribution of $-\overline{v\theta}_c$ attains about 75% of the total heat flux and supports the presumption that the upward motions of the eddies with the intermittent positive spikes of temperature fluctuation cause the upward heat transfer against the time-averaged temperature gradient. In the upper region of $y/\delta \gtrsim 0.7$, the values of $-\overline{v\theta}_c$ are not plotted, since these spikes disappear in the temperature traces, as shown in figure 2.31.

Next we discuss where these eddies with intermittent positive θ-spikes are carried from and how such spikes are generated.

Figures 2.40 and 2.41 show the variations of the distributions of $-\overline{v\theta}/v'\theta'$ and θ' with the streamwise direction in a strongly stable flow which has a stability close to that of Run VIII. They reflect the process of the developing stratification. In the upstream region, a stably stratified flow develops downstream and the very hot fluids near the free surface may plunge into the inner part of the flow because of turbulent motions. The hot fluids may be stored in the flow because of a presence of wavelike motion

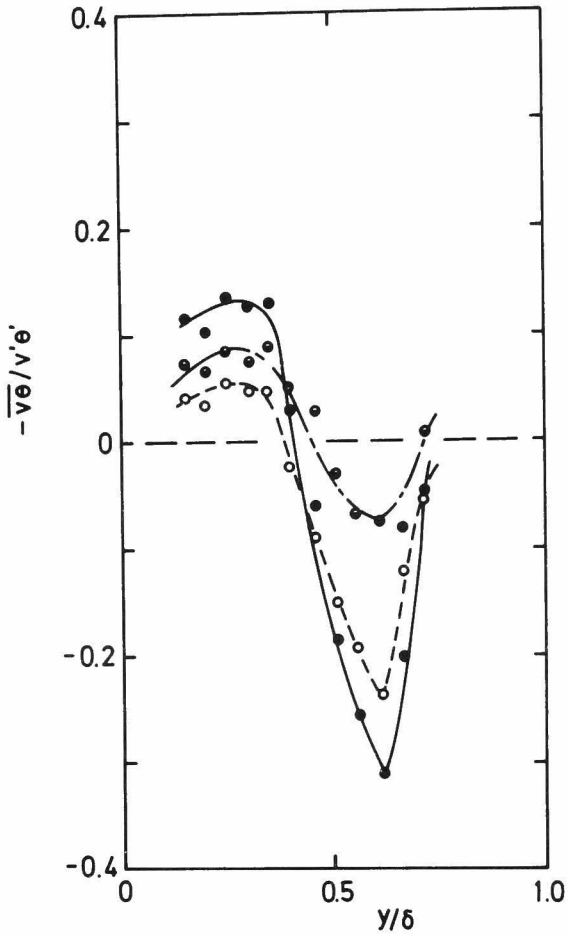

Figure 2.39. Nondimensional vertical heat flux by the intermittent eddies with larger temperature fluctuations than the threshold level.

—●— $-\overline{v\theta}/v'\theta'$ in figure 2.18 by whole eddies

--○- $-\overline{v\theta}_c/v'\theta'$ by intermittent eddies with larger temperature than the threshold level in figure 2.38.

—-●-·- $-\overline{v\theta}/v'\theta'$ plus $\overline{v\theta}_c/v'\theta'$

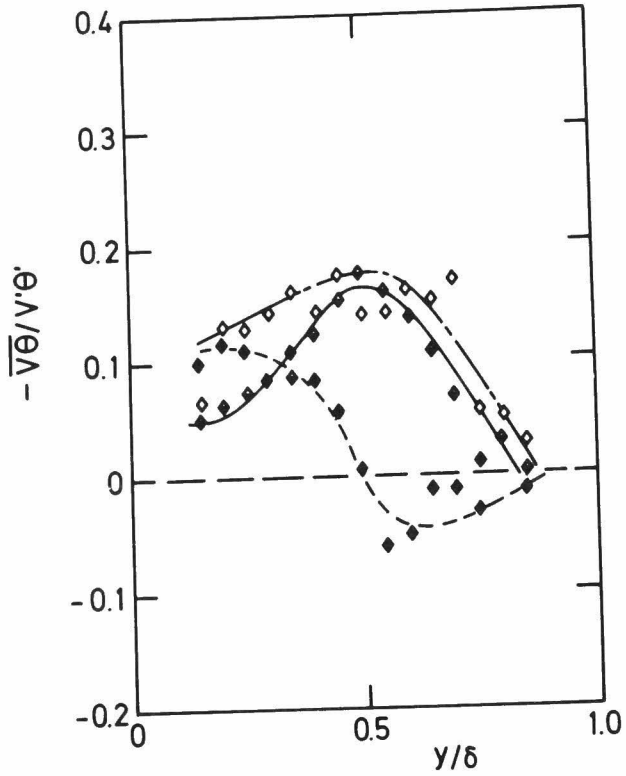

Figure 2.40. Variations of $-\overline{v\theta}/v'\theta'$ against x/δ.

◆ x/δ= 37.5 , ◆ x/δ= 50.0 , ◇ x/δ= 75.0.

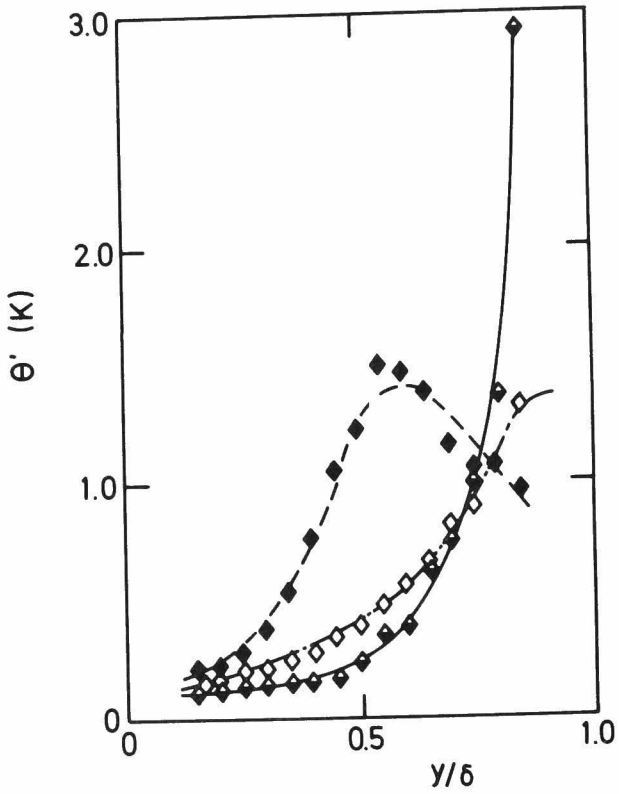

Figure 2.41. Variations of θ' against x/δ.
Symbols as in figure 2.40.

with extremely strong stability. Then, the number of the hot fluids stored in the wavelike layer may increase with increasing y/δ, and it may form the mean temperature gradient and intermittent temperature fluctuations near $y/\delta=0.6$, as shown in figures 2.6 and 2.31. The hot fluids stored in the wavlike layer are carried downstream by the convective motion, and the wavelike layer may be accelerated downstream. In the region near $x/\delta=50$, the wavelike motion may break down by shear instability near the lower edge of the wavelike layer (see plate 2.2). Then, the breakdown may cause the buoyancy-driven upward motion of the hot eddies stored in the lower region of the wavelike layer. On the other hand, the downward motion of the fluids in the upper layer of $y/\delta \gtrsim 0.7$ will be also happen. However, it should be noted that the probability of the downward motion of hot fluids stored in the upper layer will become low due to the buoyancy effect. These behaviors may cause the upward heat transfer against the time-averaged temperature gradient, and the mechanism may be similar to that suggested by Deardorff et al. [31], Willis & Deardorff[28], Zeman & Lumley[32] and Lenschow[33].

In the downstream region near $x/\delta=75$, the hot eddies may become absent because of the upward motions in the region of $x/\delta \simeq 50.0$. Thus, $-\overline{v\theta}/v'\theta'$ becomes positive in the whole range of y/δ and θ' decreases in the region of $y/\delta \lesssim 0.8$.

Such variations of θ' and $-\overline{v\theta}/v'\theta'$ with x/δ seem to exhibit the strong inhomogeneity in the flow direction. It should be noted, however, that these variations are small in comparison with the variations in the vertical direction.

The change of the sign of $-\overline{uv}/u'v'$ may be attributed to the same mechanism, that is, the upward motion of the eddies with the positive spikes of temperature fluctuation may cause the upward momentum transfer against the time-averaged velocity gradient. However, this

is not definite because of the lack of simultaneous measurements of u, v and θ.

2.3.3 Correlation of turbulence quantities with local gradient Richardson number

As mentioned in the previous section, the flow is not completely homogeneous but may be regarded as one of the most ideal flows, close to plane-homogeneity. From this fact together with the assumption that the turbulence structure is determined by the local level of stability, turbulence quantities will be correlated by using the local gradient Richardson number, Ri. In figure 2.42 the turbulence quantities are plotted against the local gradient Richardson number. The values measured in the layer of $0.4 \lesssim y/\delta \lesssim 0.75$ were adapted in the correlation, since even in the neutral case the turbulence quantities change largely except in that layer and the local Richardson number can be more reliably estimated in that layer.

The ratio of the time-averaged square value of the vertical velocity fluctuation to that of the streamwise velocity fluctuation, $\overline{v^2}/\overline{u^2}$, decreases slightly as the stratification shifts from neutral to weakly stable conditions and then increases as Ri becomes larger. Whereas the ratio of $\overline{w^2}/\overline{u^2}$ is almost constant in the whole range of Ri. The fact that the vertical motion is more promoted than the horizontal motion under strongly stable conditions can be easily understood, since the vertical motions are more strongly promoted by the buoyancy force due to the upward heat transfer, as shown in figure 2.10.

The correlation coefficient of the Reynolds stress, $-\overline{uv}/u'v'$, decreases with increasing Ri and becomes negative in the range of

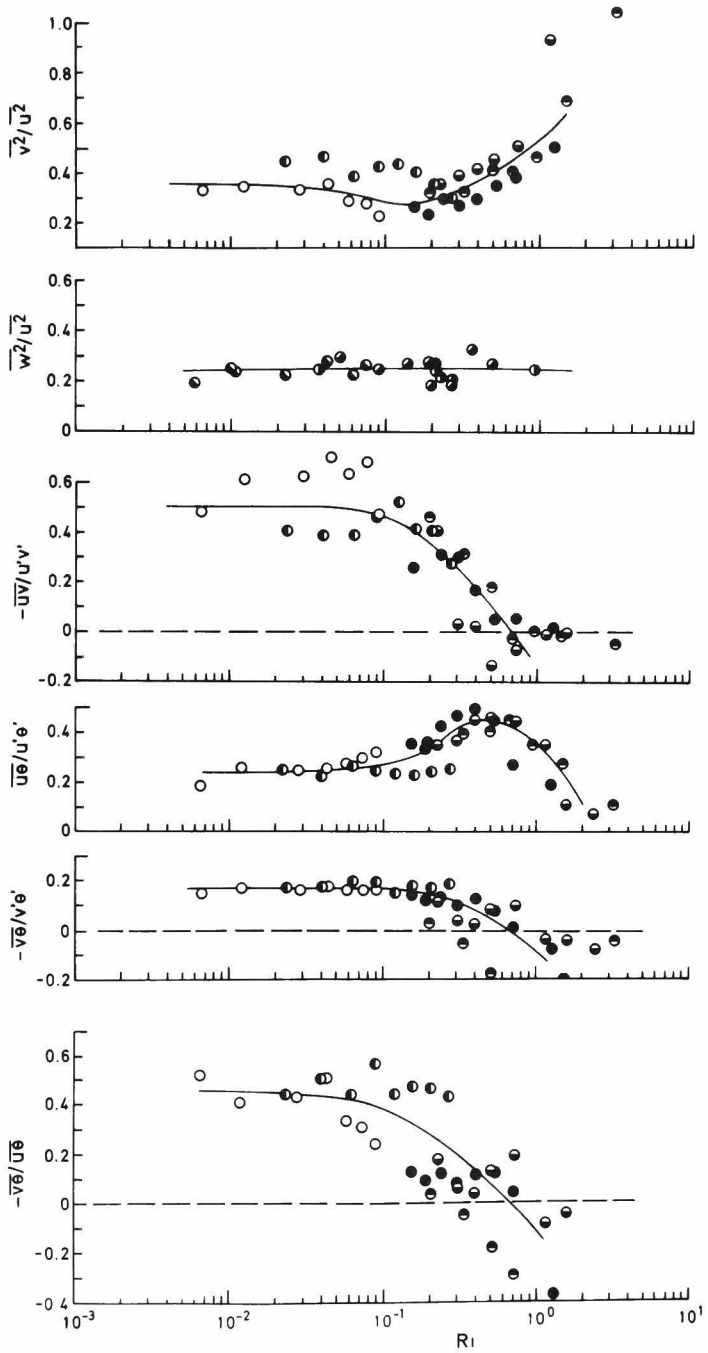

Figure 2.42. Correlation of the turbulence quantities with the local gradient Richardson number.

——— best fitting curve

Symbols as in table 2.1.

$Ri \gtrsim 0.7$. A similar behavior is seen in the distribution of the correlation coefficient of the vertical heat flux, $-\overline{v\theta}/v'\theta'$. That is, the vertical transfers of momentum and heat are suppressed in weakly stable conditions, and in the extremely stable range of $Ri \gtrsim 0.7$ they occur against their time-averaged gradients. Whereas, the correlation coefficient of the streamwise heat flux, $\overline{u\theta}/u'\theta'$, shows a different behavior; it increases once and then decreases under strongly stable conditions.

The ratio of the vertical heat flux to the streamwise one, $-\overline{v\theta}/\overline{u\theta}$, decreases rapidly with increasing stability and ultimately crosses the zero values.

Thus, the turbulence quantities can be well correlated with the Richardson number, Ri, despite the imperfect development of the flow in the strongly stable conditions. In fact, the values of $-\overline{v\theta}/v'\theta'$ measured at three stations of x/δ are also correlated with Ri, as shown in figure 2.43. Thus, the local gradient Richardson number may be regarded as the predominant parameter for representing the effects of stability, and the change of the turbulence quantities with Ri is expected to be universal and to offer the information useful in the closure problem in turbulence.

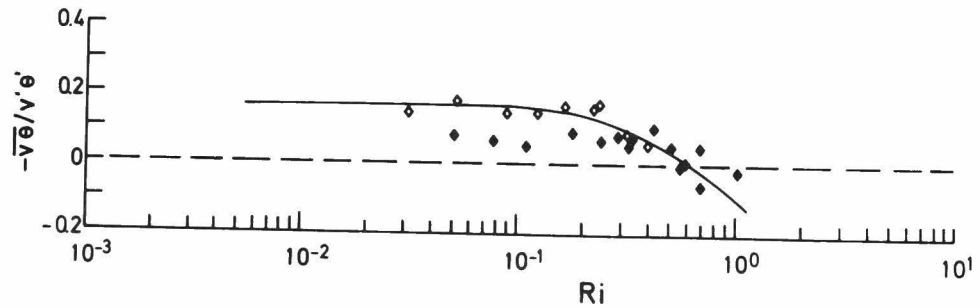

Figure 2.43. Correlation of $-\overline{v\theta}/v'\theta'$ with Ri at three stations.

◇ $x/\delta=50.0$, ◆ $x/\delta=62.5$, ◆ $x/\delta=70.0$

——— best fitting curve from figure 2.42.

2.4 Conclusion

The turbulence structure under the stably stratified conditions have been investigated in an open channel flow in which the thermal stratification is established by the vapor condensation at the free surface. The main results investigated here can be summarized as follows.

1. Distributions of turbulence quantities are strongly affected by buoyancy, and their variations with bulk Richardson number, $\overline{Ri}$, can be interpreted by using the contribution terms in their transport equations.

2. In a strongly stable flow, fluctuating motions consist of turbulence and wavelike motions. In the upper layer with large temperature gradient, wavelike motions are predominant, while turbulent motions prevail in the weakly stratified lower layer. At the boundary between the upper and lower layers the intermittent upward motions of the hot eddies with large positive spikes of temperature fluctuation are caused by the breakdown of the wavelike motion and by the buoyancy-driven force, and transfer heat and momentum against the temperature and velocity gradients.

3. The local gradient Richardson number, Ri, is the predominant parameter for representing the buoyancy effects on the turbulence structure in stably stratified flows, and the variations of the turbulence quantities are correlated well with Ri.

CHAPTER 3 TURBULENCE STRUCTURE IN UNSTABLY STRATIFIED FLOW

3.1 Introduction

This chapter concerns the investigation of turbulence structure in unstably stratified flow. In this flow buoyancy produces turbulence energy and so enhances the vertical turbulent transport of heat. Buoyancy effects on the eddy diffusivities have been investigated by some workers; Charnock[1], Businger et al.[2], Wyngaard & Cote'[4], Pruitt et al.[7] and Ueda et al.[34] in the field observations, and Arya[10] in the wind tunnel. However, the number of the previous papers dealing with the direct turbulence measurements is comparatively small; Haugen et al.[3] and Arya[10], and the detailed turbulence structure of unstably stratified flow has not yet been clarified.

Extensive investigations have been performed in flow without shear, i.e., in the turbulent free convection over a horizontal surface. In his pioneer work, Malkus[35,36] first dealt with it using the stability theory, and Howard[37] and Busse[38] extended this work. Recently Zeman & Lumley[32] and Lumley et al.[39] successfully applied an eddy-damped, quasi-Gaussian approximation to the equations for the third moments of turbulence quantities and predicted realistic inversion rise rates and heat flux profiles. Despite these, experimental information on the turbulence structure is limited to a few papers such as Townsend[40], Willis & Deardorff[41], Deardorff & Willis[42], etc.

The purpose of this chapter is to experimentally investigate the buoyancy effects on the turbulence structure in unstably stratified open channel flow and to clarify the mechanism of the enhancement of the turbulent transport.

Unstably stratified flow was obtained by putting heated water of

323-343K into the flume described in section 2.2 and permitting high heat flux from the evaporation at the free surface. Strongly unstable stratification was attained also in this flow case, since the temperature gradient is large near the free surface where the velocity gradient is small.
Various turbulence quantities are discussed by using two parameters; the bulk Richardson number, $\overline{Ri}$, and the local gradient Richardson number, Ri, and by estimating the contribution terms in their transport equations. Turbulence structure was also investigated by means of the same statistical analyses used in chapter 2.

3.2 Experiment

3.2.1 Experimental apparatus and measuring equipment

The experimental apparatus and the measuring equipment used here were the same used in chapter 2. Thus, only the main features of the flow system will be described here. Figure 3.1 illustrates the flow system of the experimental apparatus. Hot water of 323-343K was recirculated through the flume by a pump and the water temperature was kept to within $\pm$0.05K by controlling the flow rates of the cold water and the saturated steam in a temperature regulating tank. Unstable stratification was established by the evaporation cooling of the hot water at the free surface.
The measurements were performed at the center of the flume, at distance 4.2m downstream from the entrance. Velocity and temperature were measured by using the same laser Doppler velocimeter and constant-current thermometer described in chapter 2.

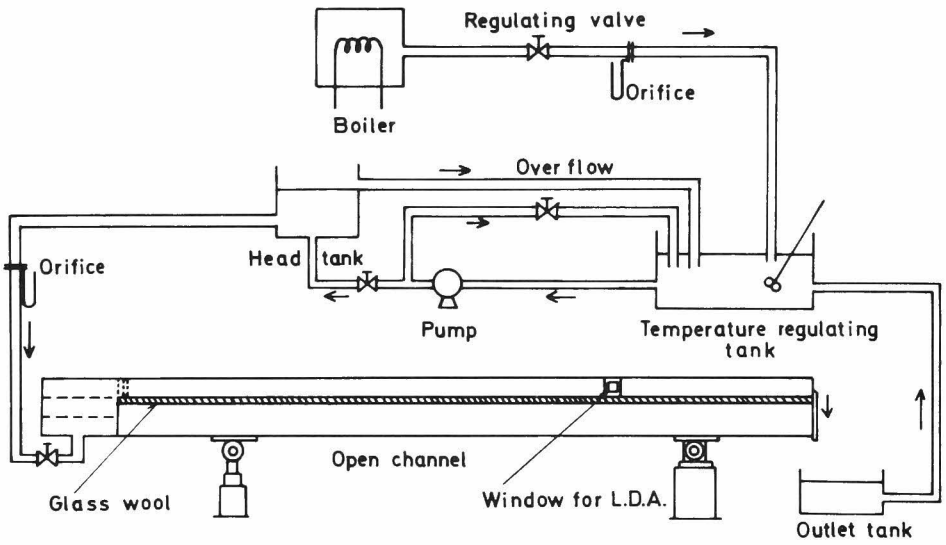

Figure 3.1. Flow system of experimental apparatus.

3.2.2 Flow conditions

Flow conditions for the present runs are given in table 3.1. The flow depth, δ, was maintained at approximately 0.04m. The cross-sectional mean velocities, $\overline{U}_{ave}$, ranged from 0.071m/s to 0.152m/s, so that the Reynolds numbers, Re, were 8600 to 41700 and that the hydraulic Froude numbers, Fr, were less than 0.24; therefore, all the flows were developed and subcritical turbulent flows. The symbols in table 3.1 will be used in the subsequent figures in this chapter.

3.3 Results and Discussion

3.3.1 Distributions of turbulence quantities

Time-averaged velocity and temperature

In the present flow configuration, if the flowing fluid temperature is high, the evaporation cooling occurs at the free surface and unstable stratification is established. In this case, strongly unstable flow under well developed-conditions is easily attained. Typical distributions of the time-averaged velocity and temperature are presented in figures 3.2 and 3.3. In the upper region, the velocity gradient becomes smaller than that in the neutral flow case, where the temperature gradient becomes larger. This is due to the promotion of the vertical mixing by the buoyancy force.

Turbulence intensities

The distributions of the turbulence intensities, i.e., r.m.s. values of the streamwise, vertical and lateral velocity fluctuations,

Table 3.1. Flow conditions in unstably stratified flows.

Run No.	Symbol	$\overline{Ri} \times 10^{-2}$[-]	Re[-]	$\delta \times 10^{-2}$[m]	$R \times 10^{-2}$[m]	$\overline{U}_{ave} \times 10^{-2}$[m/s]	$u^* \times 10^{-3}$[m/s]
I	△	0.0 (neutral)	8600	4.0	3.1	7.1	4.6
II	□	-1.23(unstable)	41700	4.0	3.2	15.2	8.0
III	▨	-2.03(unstable)	18300	3.9	3.1	8.0	4.6
IV	▨	-2.96(unstable)	17700	4.0	3.2	7.8	4.6
V	■	-3.53(unstable)	21200	4.0	3.2	7.9	4.5
VI	◧	-3.70(unstable)	21300	4.0	3.2	7.8	4.5
VII	▬	-3.90(unstable)	23200	4.0	3.2	7.8	4.4
VIII	◪	-4.63(unstable)	24200	4.1	3.2	7.6	4.2
IX	◪	-4.90(unstable)	23700	4.0	3.1	7.9	4.5

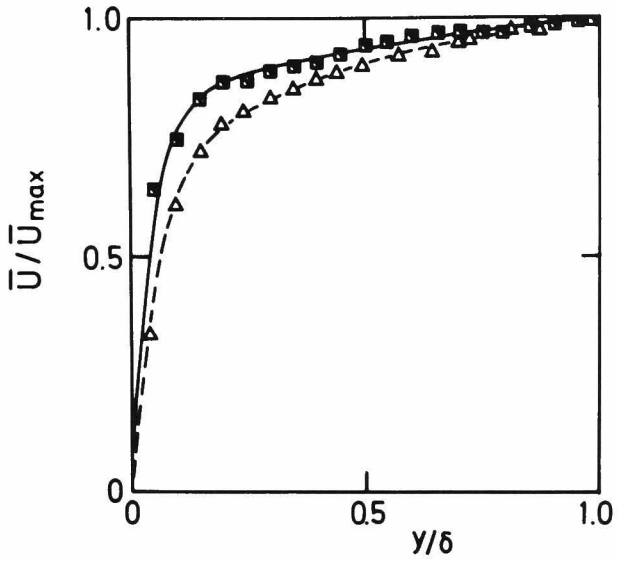

Figure 3.2. Typical distributions of the time-averaged velocities.
△ $\overline{Ri}$ = 0.0 , ◪ $\overline{Ri}$ = -4.90x10 ^{2}.

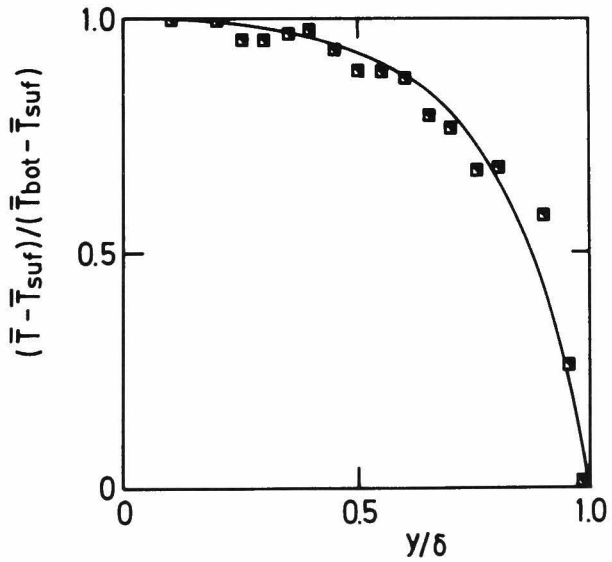

Figure 3.3. Typical distribution of the time-averaged temperature.
Symbols as in figure 3.2.

u, v and w normalized by the friction velocity are shown in figures 3.4, 3.5 and 3.6, respectively. Indeed, the intensities of all the fluctuating velocity components increase with increasing instability of the flow, that is , minus bulk Richardson number ($-\overline{Ri}$).
This is clearly seen in plate 3.1 which was obtained by hydrogen bubble technique. The unstably stratified flow contains violent streaks of bubbles indicating so promoted turbulence in the upper half region of the flow.

To understand the process of the turbulence promotion by the buoyancy force we will examine the energy production attributable to mean shear and buoyancy by using the respective transport equations (2-1) and (2-2) for the square values of the fluctuating velocity components.
The buoyancy production term, $2\beta g\overline{v\theta}/u^{*2}$, arises in the transport equation (2-2) for the square value of the vertical velocity component and the shear production term, $-2\overline{uv}\partial\overline{U}/\partial y/u^{*2}$, in the transport equation (2-1) of the square value of the streamwise velocity component.....
The distributions of those terms are shown in figures 3.7 and 3.8, respectively. The buoyancy production increases noticeably with increasing instability and provides much energy to the vertical motion. This seems to enhance the turbulence energy, which is probably redistributed to $\overline{u^2}$ and $\overline{w^2}$ through the pressure-force terms in the respective transport equations.

On the other hand, shear production has a tendency to decrease in the central region of the flow. In unstably stratified conditions the turbulence motion is enhanced, but at the same time the velocity gradient is reduced by the promotion of the vertical turbulent mixing, so that the total effect is for shear production to decrease.

Figure 3.9 shows the distributions of the r.m.s. value of the temperature fluctuation normalized by the temperature difference,

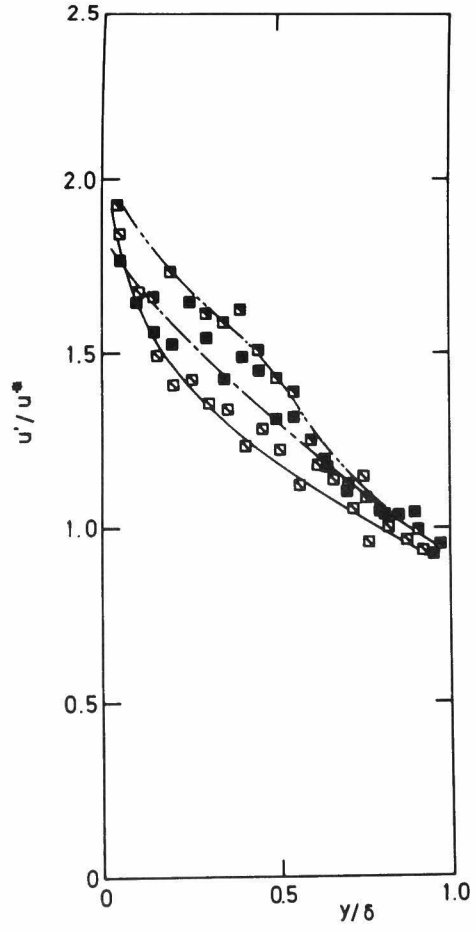

Figure 3.4. Distributions of the r.m.s. values of streamwise velocity fluctuations.

$\overline{Ri}=-2.03\times10^{-2}$, $\overline{Ri}=-3.53\times10^{-2}$, $\overline{Ri}=-4.90\times10^{-2}$.

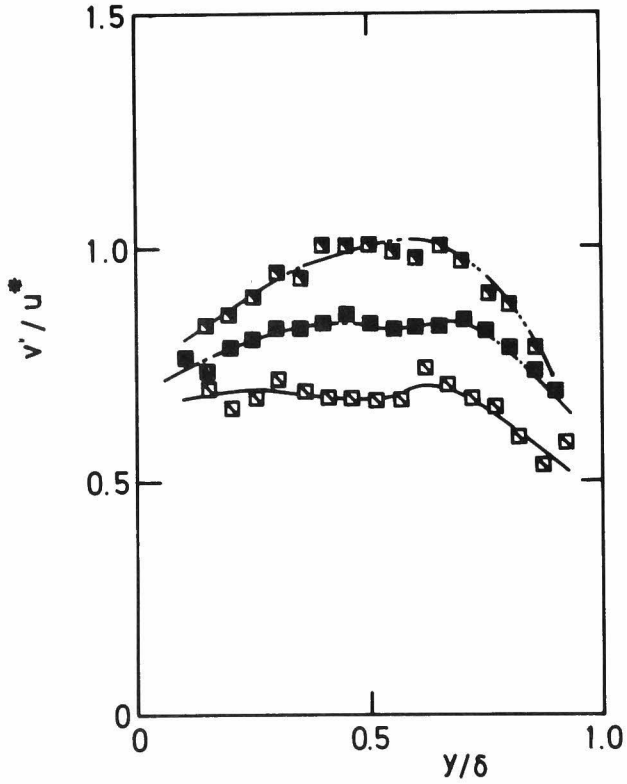

Figure 3.5. Distributions of the r.m.s. values of vertical velocity fluctuations.

Symbols as in figure 3.4.

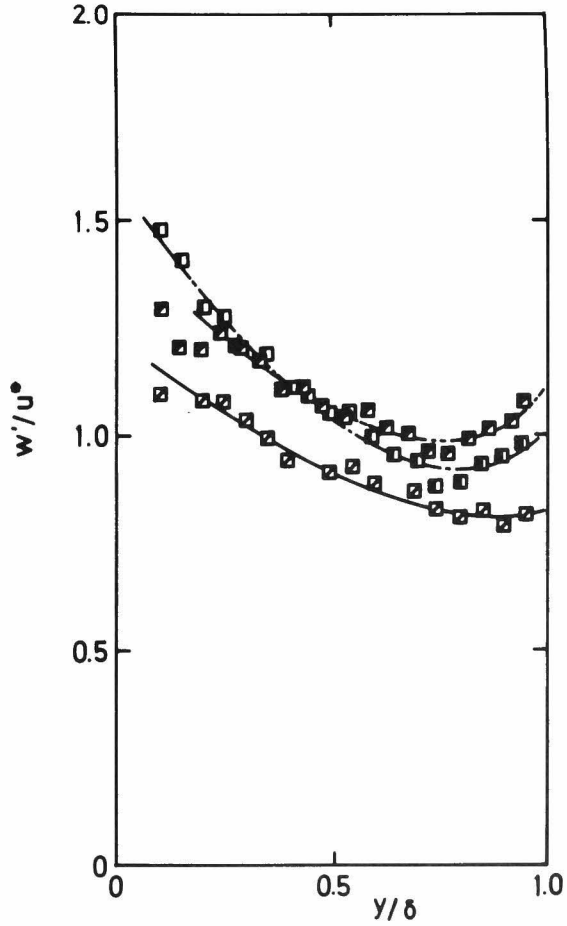

Figure 3.6. Distributions of the r.m.s. values of lateral velocity fluctuations.

$\overline{Ri}=-2.96\times10^{-2}$, $\overline{Ri}=-3.70\times10^{-2}$, $\overline{Ri}=-4.63\times10^{-2}$.

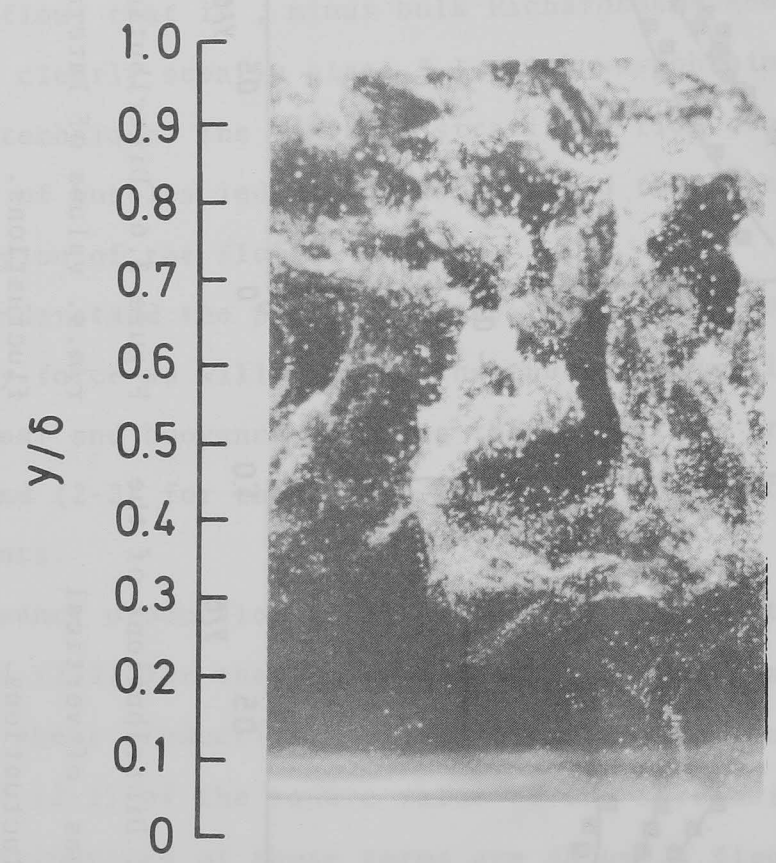

Plate 3.1. Flow pattern of an unstably stratified flow, obtained by hydrogen bubble technique.

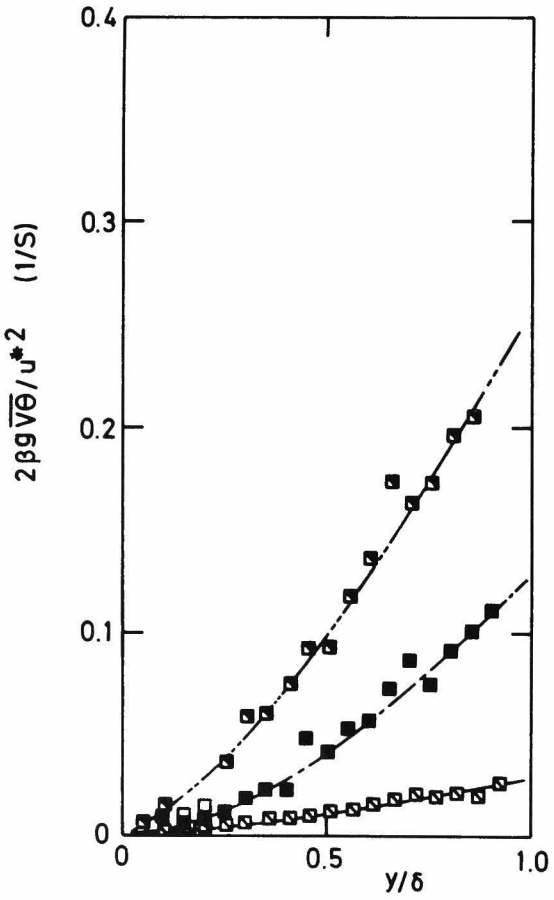

Figure 3.7. Distributions of the buoyancy term, $-2\beta g\overline{v\theta}/u^{*2}$.

$\overline{Ri} = -2.03\times10^{-2}$, $\overline{Ri} = -3.53\times10^{-2}$, $\overline{Ri} = -4.90\times10^{-2}$.

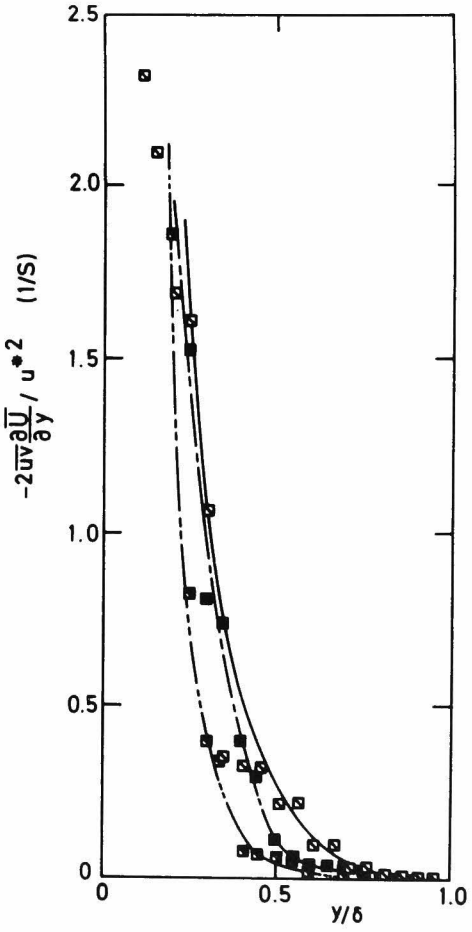

Figure 3.8. Distributions of the shear production term, $-2\overline{uv}(\partial\overline{U}/\partial y)/u^{*2}$. Symbols as in figure 3.7.

$\theta'/(\overline{T}_{bot}-\overline{T}_{suf})$. The variation of $\theta'/(\overline{T}_{bot}-\overline{T}_{suf})$ with $\overline{Ri}$ is very small. This may be due to that the influential contribution term, i.e., the production term, $2\overline{v\theta}(\partial\overline{T}/\partial y)/(\overline{T}_{bot}-\overline{T}_{suf})^2$, in equation (2-3) does not almost change, as shown in figure 3.10.

Correlation coefficients of the Reynolds stress and heat fluxes

Figure 3.11 shows the distributions of the correlation coefficient of the Reynolds stress, $R_{uv} = -\overline{uv}/u'v'$. The correlation coefficient R_{uv} decreases with increasing instability (increasing $-\overline{Ri}$). Again, this fact may be understood by examing the production terms of the transport equation (2-4) of $-\overline{uv}$.
The production rates by shear and buoyancy are represented by $\overline{v^2}\partial\overline{U}/\partial y$ and $\beta g\overline{u\theta}$, respectively. As seen in figure 3.12, the production by shear normalized by u'v' decreases remarkably with instability.
On the other hand, the buoyancy production shown in figure 3.13 increases with increasing instability, but it is one order of magnitude smaller than the shear production. Therefore, the reduction of the shear production is suspected to cause the variation of R_{uv}.

Figure 3.14 shows the distributions of the correlation coefficent of the streamwise heat flux, $-R_{u\theta}=-\overline{u\theta}/u'\theta'$, (note the negative value of $\overline{u\theta}$ in unstably stratified flow case). In the upper region of $y/\delta \gtrsim 0.6$, $-R_{u\theta}$ decreases with increasing instability, and in the lower region its behavior is contrary. Here again we will introduce the production term, $(\overline{uv}\partial\overline{T}/\partial y + \overline{v\theta}\partial\overline{U}/\partial y)/u'\theta'$, in the transport equation (2-5) of $-\overline{u\theta}$, as shown in figure 3.15. The variation of the production term with instability is, however, very small , and we cannot interpret the behavior of $-R_{u\theta}$ only with the production term. The residuary contribution terms in the equation (2-5) may be more predominant to

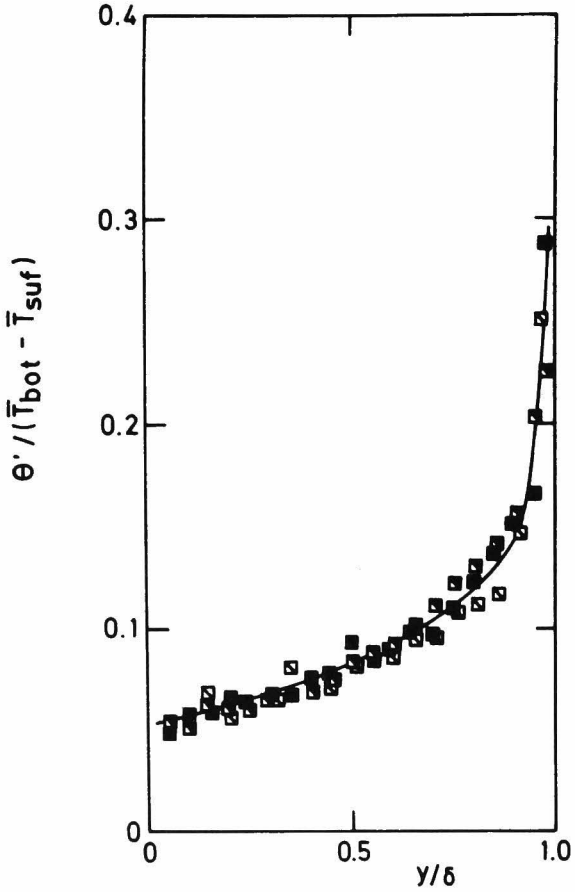

Figure 3.9. Distributions of the r.m.s. values of temperature fluctuations.
▨ $\overline{Ri} = -2.03\times10^{-2}$, ■ $\overline{Ri} = -3.53\times10^{-2}$,
◪ $\overline{Ri} = -4.90\times10^{-2}$.

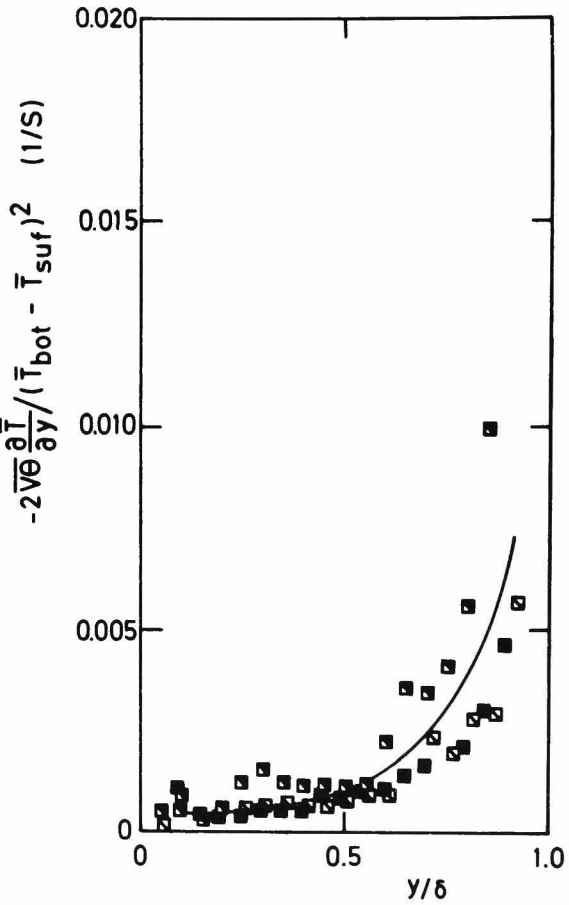

Figure 3.10. Distributions of the production term, $-2\overline{v\theta}(\partial\overline{T}/\partial y)/(\overline{T}_{bot}-\overline{T}_{suf})^2$. Symbols as in figure 3.9.

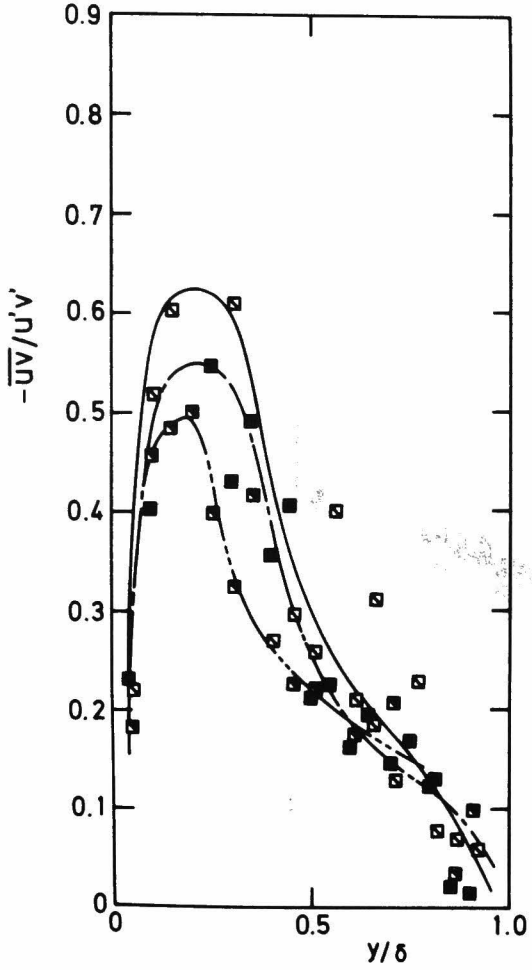

Figure 3.11. Distributions of the correlation coefficient of the Reynolds stress.

▨ $\overline{Ri} = -2.03\times10^{-2}$, ■ $\overline{Ri} = -3.53\times10^{-2}$

▩ $\overline{Ri} = -4.90\times10^{-2}$.

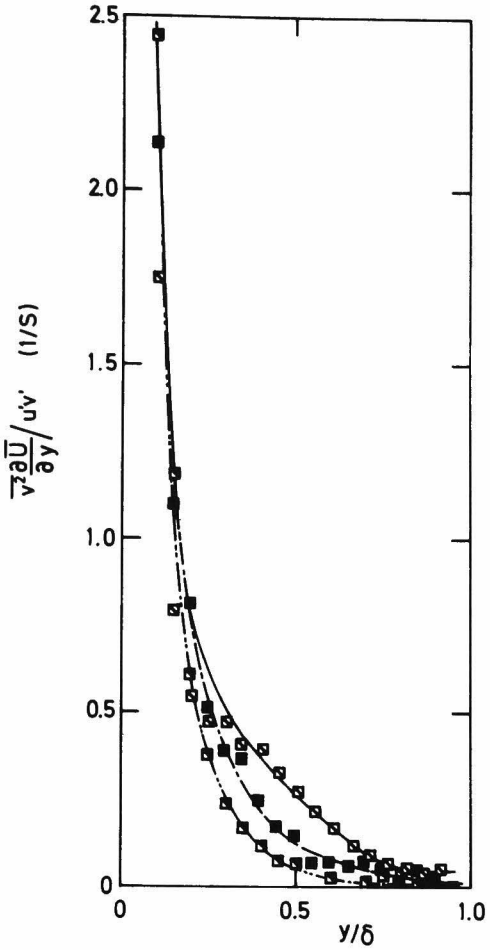

Figure 3.12. Distributions of the shear production term, $\overline{v^2}(\partial\overline{U}/\partial y)/u'v'$.

Symbols as in figure 3.11.

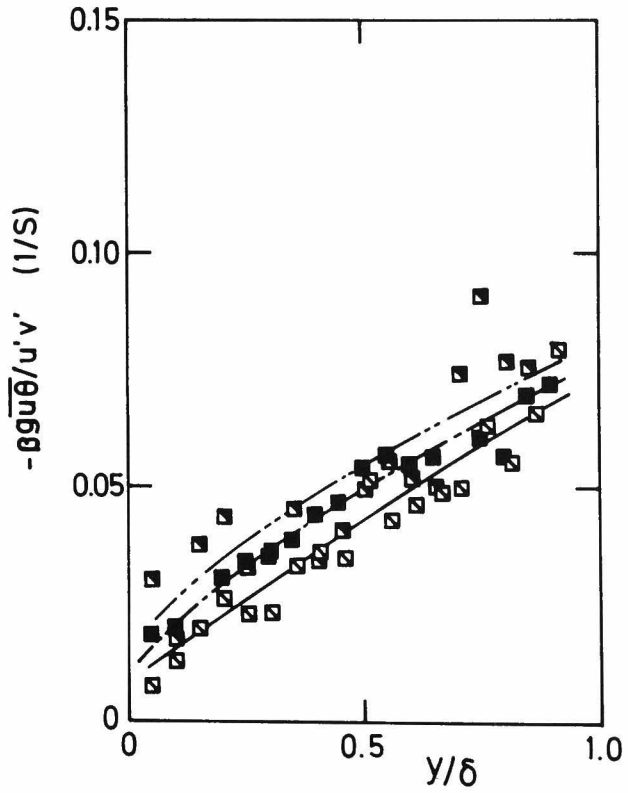

Figure 3.13. Distributions of the buoyancy production term, $-\beta g\overline{u\theta}/u'v'$.

Symbols as in figure 3.11.

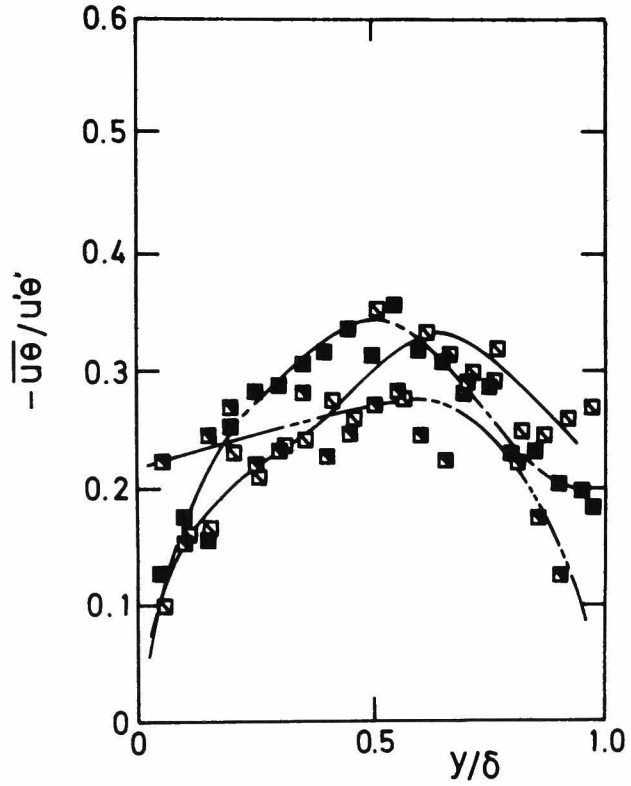

Figure 3.14. Distributions of the correlation coefficient of the streamwise heat flux. ▨ $\overline{Ri}$ = -2.03×10^{-2}, ■ $\overline{Ri}$ = -3.53×10^{-2}, ▨ $\overline{Ri}$ = -4.90×10^{-2}.

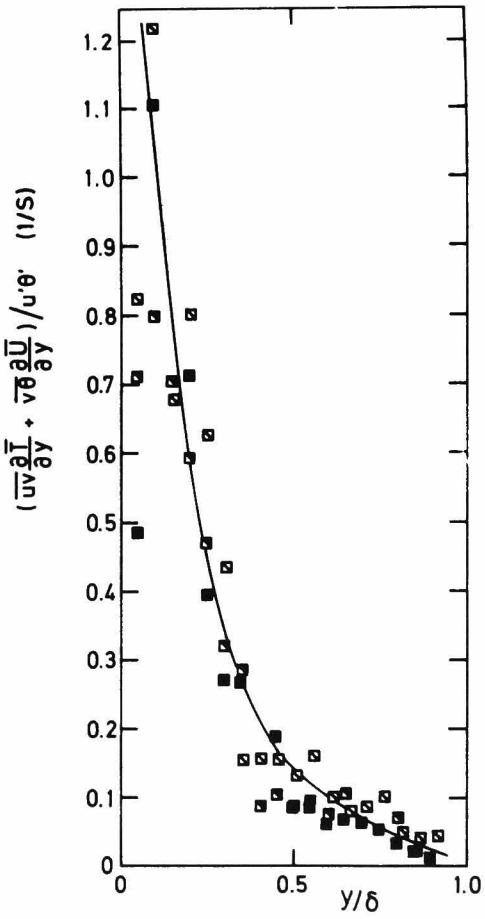

Figure 3.15. Distributions of the production term, $(\overline{uv}\partial\overline{T}/\partial y + \overline{v\theta}\partial\overline{U}/\partial y)/u'\theta'$. Symbols as in figure 3.14.

$-R_{u\theta}$.

Figure 3.16 shows the distributions of the correlation coefficient of the vertical heat flux, $-R_{v\theta} = \overline{v\theta}/v'\theta'$, (note the positive $\overline{v\theta}$ in unstably stratified flow case). The correlation coefficient $-R_{v\theta}$ increases significantly with increasing instability. Such behavior may be understood intuitively by considering the buoyancy-driven motion, that is , the positive temperature fluctuation is attributable to the upward motion and vice versa. This will be discussed from the aspect of the joint probability density of v and θ in the next section. However, the increase of the $-R_{v\theta}$ may also be interpreted through the behavior of the production term in the transport equation (2-6). In fact, the buoyancy production term $\beta g\overline{\theta^2}/v'\theta'$, increases significantly with instability as shown in figure 3.17.

Turbulence kinetic energy

Each term in the turbulence kinetic energy balance equation(2-7) is made dimensionless with δ/u_*^3, and plotted against y/δ in figure 3.18 for a strongly unstable flow(Run IX). In this diagram, the energy dissipation and the diffusion of the turbulence energy were calculated with the same procedure used in subsection 2.3.1. When we compare figure 3.18 for the strongly unstable case with the neutral case(figure 2.22), it is most striking that the buoyancy energy production makes a remarkable contribution in the turbulence energy balance in the bulk of the flow, especially in the region of $y/\delta>0.5$. In addition, the turbulent diffusion term contributes positively in the central region of $0.3<y/\delta<0.6$. This means that the turbulence energy produced by shear and buoyancy comes from the wall and free surface sides. In the turbulent diffusion term the

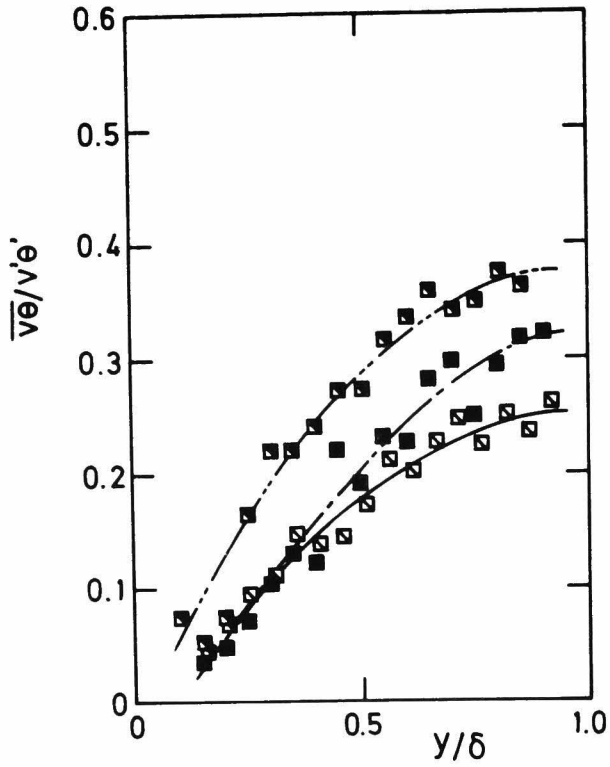

Figure 3.16. Distributions of the correlation coefficient of the vertical heat flux.

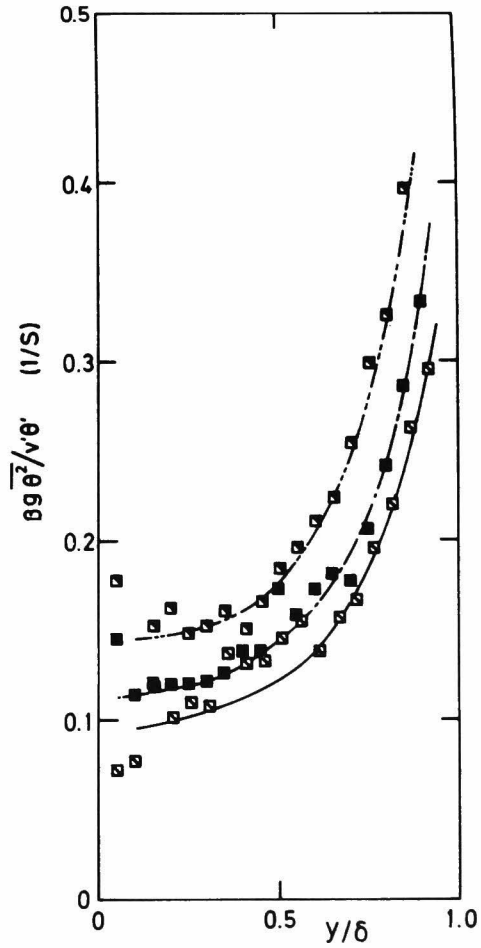

Figure 3.17. Distributions of the buoyancy production term, $\beta g\overline{\theta^2}/v'\theta'$.

▨ $\overline{Ri} = -2.03\times10^{-2}$, ■ $\overline{Ri} = -3.53\times10^{-2}$, ▩ $\overline{Ri} = -4.90\times10^{-2}$.

contribution by the pressure fluctuation cannot be examined experimentally, but the vertical flux of the kinetic energy by the turbulent motion can be estimated easily. The vertical flux of the turbulent kinetic energy $\overline{vq^2}$ was calculated on the assumption that $\overline{vq^2} \simeq \overline{v(u^2+2v^2)}$ and is plotted in figure 3.19 for strongly unstable flow(Run IX). From this figure it is clearly confirmed that the energy produced in this lower region is convected upward and the energy of the upper region is transferred into the central region.

3.3.2 Turbulence structure

Probability and joint probability density distributions, skewness and flatness factors

Figures 3.20, 3.21 and 3.22 show the probability density functions of the streamwise and vertical velocity fluctuations and the temperature fluctuation at four positions in a strongly unstable flow (Run IX). The probability density functions of u and v,i.e.,Pu and Pv normalized by the r.m.s. value of each variable, are similar to those in neutral flow(Ueda & Mizushina[25]); Pu shifts slightly on the positive u-side from the symmetry line and Pv closely approximates a normal distribution. On the contrary,Pθ deviates greatly from normality and has an extremely long skirt on the negative θ-side. These are more clearly demonstrated by the skewness and flatness factors. Figures 3.23, 3.24 and 3.25 show these factors for Pu, Pv and Pθ in a weakly unstable flow(Run III) and a strongly unstable flow(Run IX).
Since values of the skewness and flatness factors are 0.0 and 3.0, respectively for normal distribution, as shown by the dashed lines in the figures, the deviation of the measured distributions of Pθ

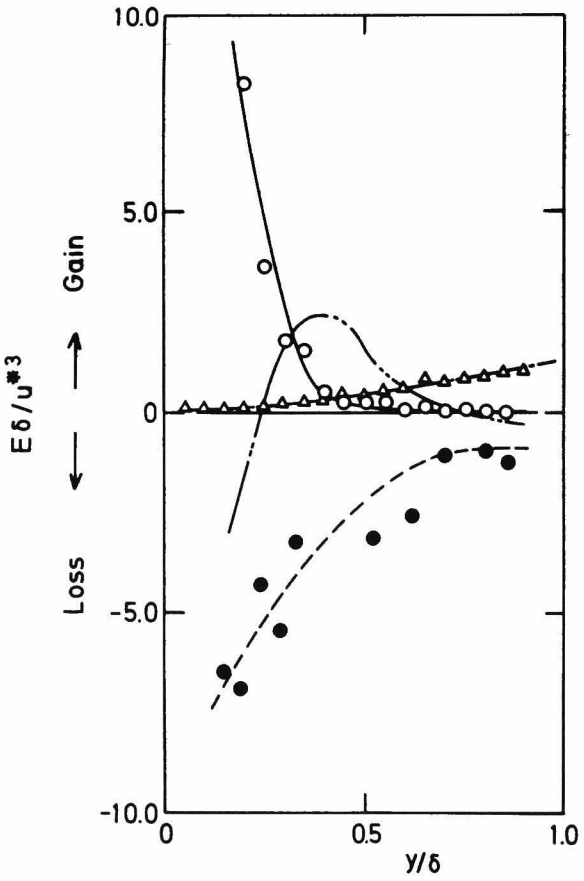

Figure 3.18. Turbulence kinetic energy balance.
(in a strongly unstable flow)
Run IX

—○— shear production, -·-△-·- buoyancy production,
--●-- dissipation , —··— diffusion.

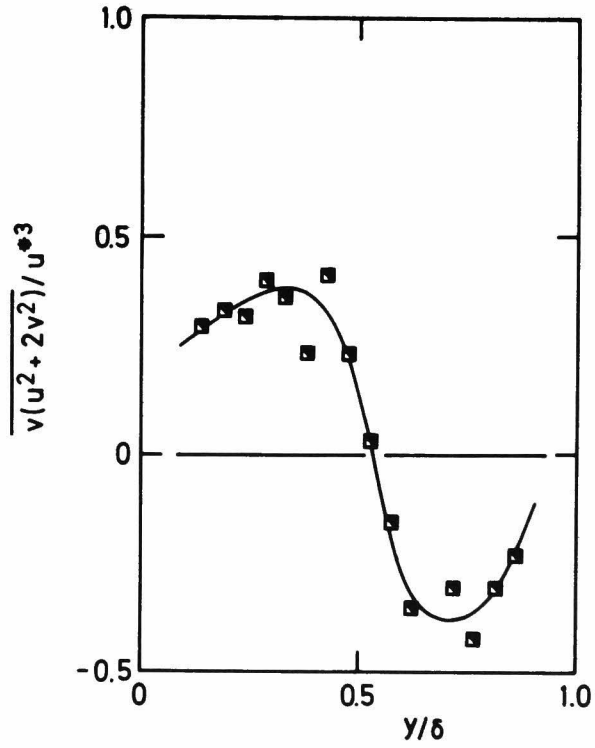

Figure 3.19. Distributions of the vertical flux of turbulence kinetic energy.
(in a strongly unstable flow)
Run IX

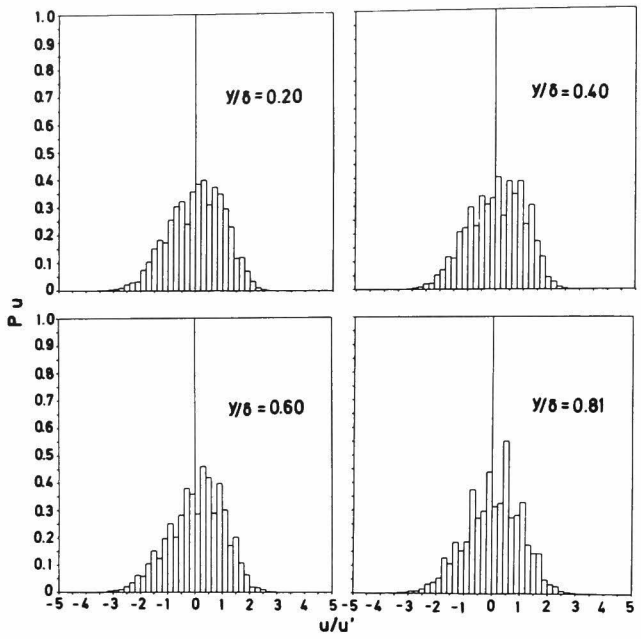

Figure 3.20. Probability density function of streamwise velocity fluctuations. (Run IX)

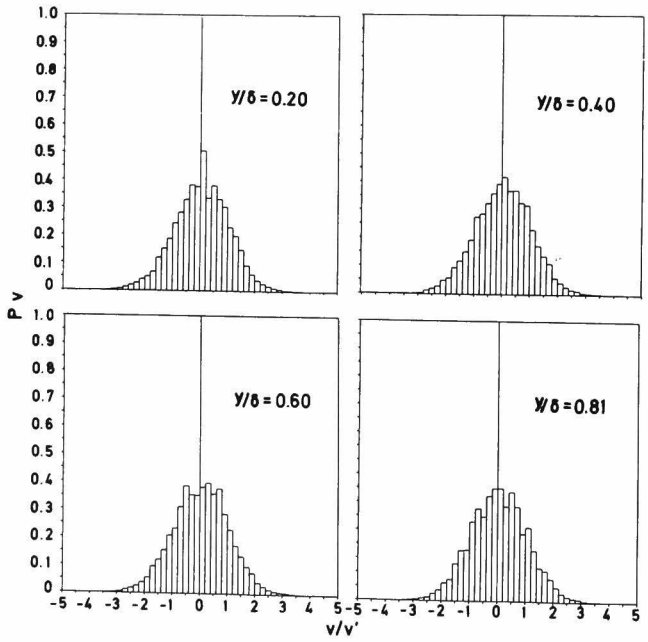

Figure 3.21. Probability density function of vertical velocity fluctuations. (Run IX)

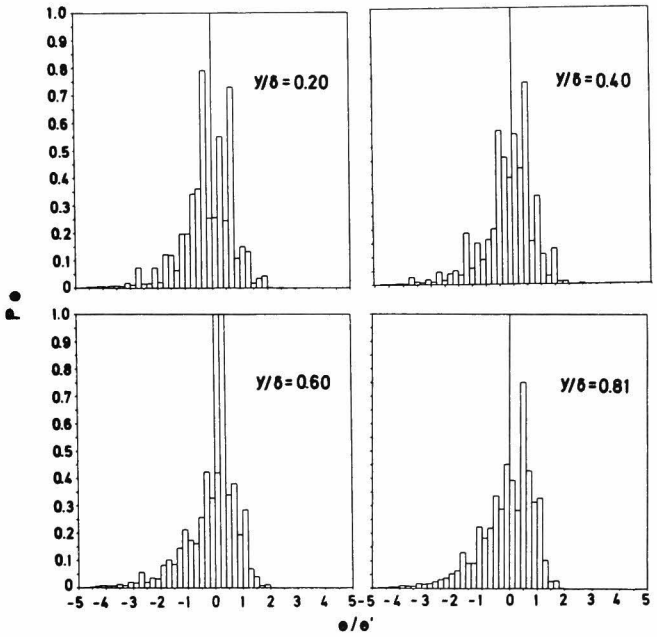

Figure 3.22. Probability density function of temperature fluctuations. (Run IX)

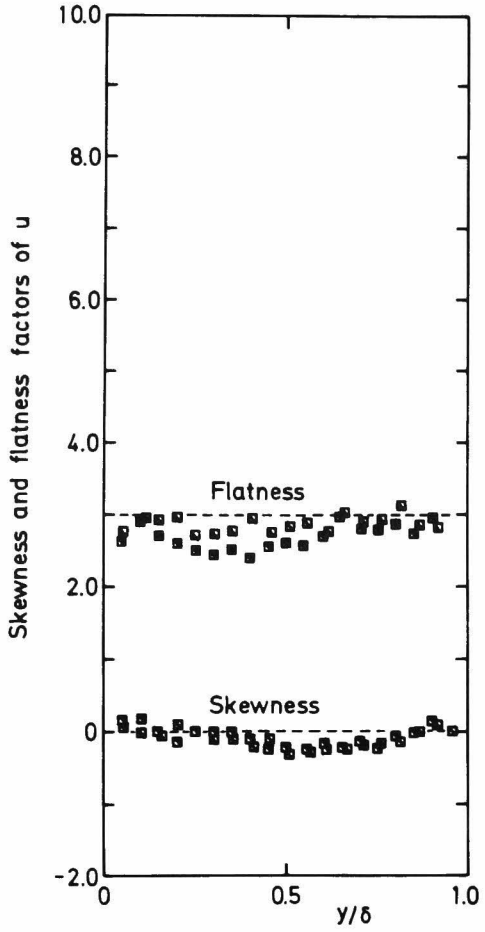

Figure 3.23. Skewness and flatness factors of streamwise velocity fluctuations.

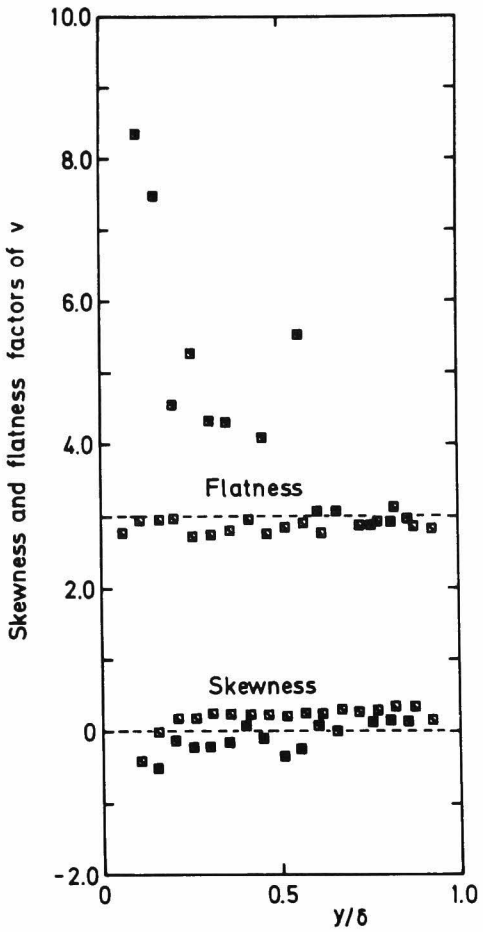

Figure 3.24. Skewness and flatness factors of vertical velocity fluctuations.

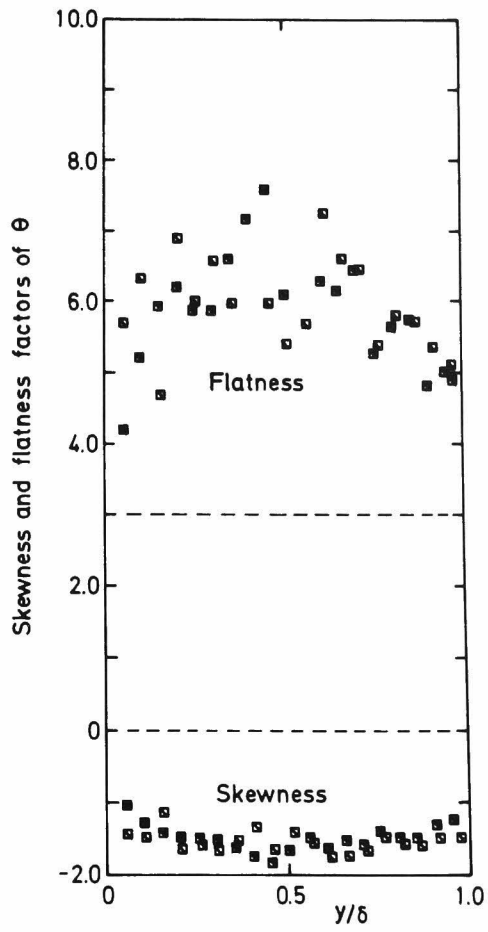

Figure 3.25. Skewness and flatness factors of temperature fluctuations.

■ $\overline{Ri} = -4.90 \times 10^{-2}$, ▨ $\overline{Ri} = -2.03 \times 10^{-2}$.

from normality is so obvious. As pointed out by Batchelor & Townsend [26], large value of the flatness factor may be due to the intermittent nature of the fluctuating signal.

We can see the abnormal fluctuations with the intermittent negative spikes in the θ signal, which is shown in figure 3.26 as a simultaneous recording of the instantaneous values of θ, v and $v\theta$ at $y/\delta=0.60$ in a strongly unstable flow (Run IX). The intermittent negative spikes of θ are accompanied by the negative values of v fluctuation, and result in a positive $v\theta$-product as noted by arrows in the figure. The spikes in the θ and $v\theta$ signals are the most prominent feature in unstably stratified flow. Physically, this means that the downward motion of the eddies with negative temperature fluctuation is predominant. The mechanism may be clearly represented in the joint probability functions, $P_{v\theta}$, as shown in figure 3.27.
In neary neutral stratification(e.g., $y/\delta=0.20$), $P_{v\theta}$ is distributed equally in all the quadrants. However, as the instability increases, it becomes distributed unsymmetrically in the first and third quadrants. The spread of the area under the outermost ring in the third quadrant is especially large. This suggests that the motion in unstably stratified flow statistically consists of upward movement of hot eddies and downward movement of cold eddies. The mechanism of the downward motion with negative large temperature spikes is important in the turbulence structure and the turbulent transport in strongly unstable stratification.
Similarly, the distributions of P_{uv} and $P_{u\theta}$ are shown in figures 3.28 and 3.29. In the upper region with strong instability, P_{uv} becomes more circular. This is corresponding to the reduced correlation between u and v, as shown in figure 3.11. It is seen that the shape of $P_{u\theta}$ does not almost change with y/δ.

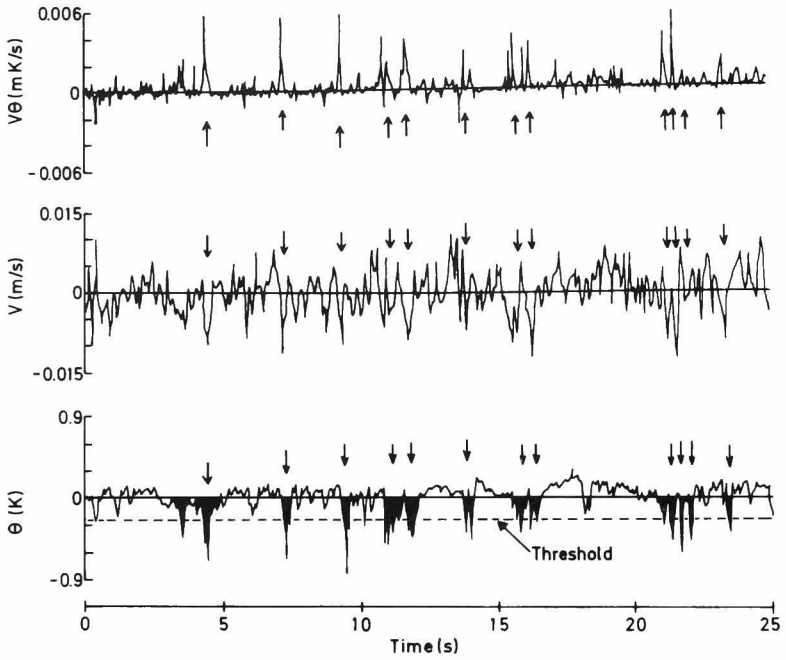

Figure 3.26. Simultaneous recording of the instantaneous values of θ, v and $v\theta$ at $y/\delta=0.6$ in a strongly unstable flow. (Run IX)
dashed line; threshold level for conditional averaging procedure.

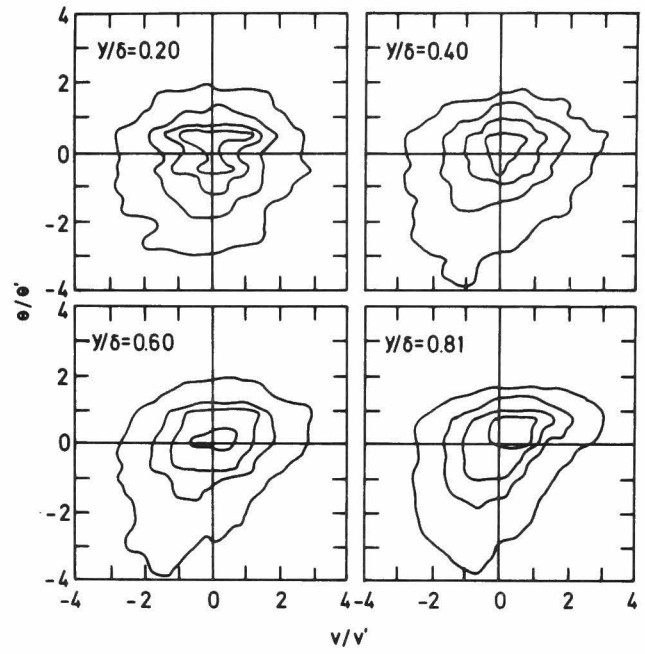

Figure 3.27. Joint probability density functions of v and θ.
(Run IX)

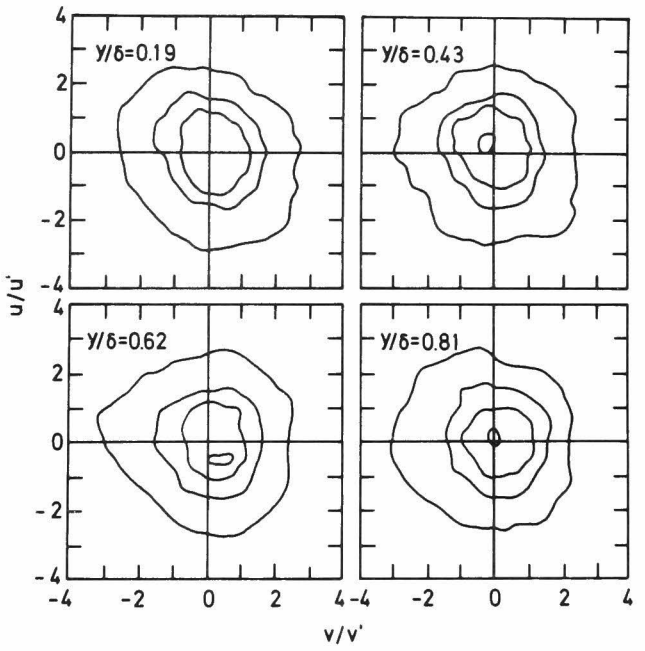

Figure 3.28. Joint probability density functions of u and v.
(Run IX)

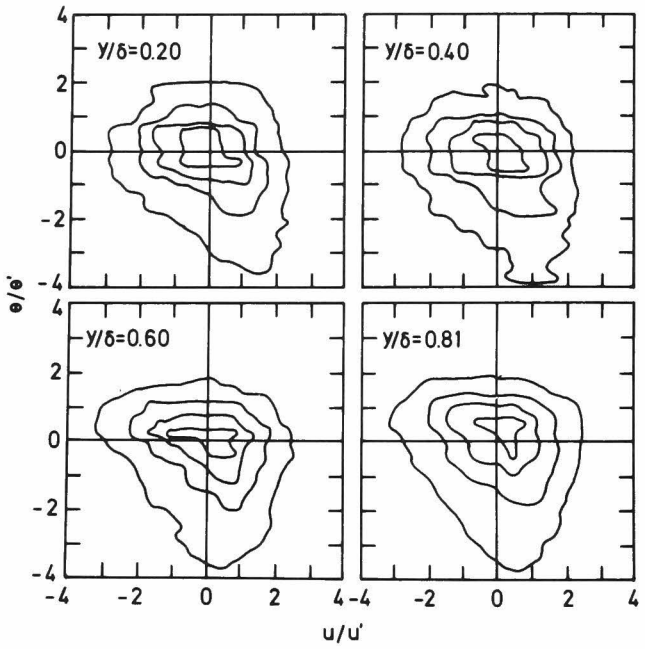

Figure 3.29. Joint probability density functions of u and θ. (Run IX)

Contribution of eddies with large negative spike of temperature fluctuation

To clarify the turbulent transfer mechanism related to the above mentioned downward motion of eddies with large negative spikes of temperature fluctuation, we set a threshold with the negative magnitude of the r.m.s. value of θ, θ', in the θ-trace(shown by a dashed line in figure 3.26). The vertical heat flux and the contribution of the eddies with negative temperature fluctuation larger than the threshold level were determined and are shown in figure 3.30. In the diagram, the solid circles denote the total heat flux in the vertical direction normalized by $v'\theta'$, and the open circles show the contribution of the intermittent eddies with negative spikes of temperature fluctuation. The contribution by the intermittent eddies is significant and occupies more than 70% of $-\overline{v\theta}/v'\theta'$ in the region near $y/\delta = 0.6$. This means the intermittent downward motion of the cold eddies are most significant in the buoyant convection.

Phase angle and coherence

To investigate the eddy motion in more detail, we discuss the turbulence behavior in wavenumber space.
Figure 3.31 shows the v-θ phase angles and coherences as a function of wavenumber k for four positions in a strongly unstable flow (Run IX). In the lower layer with nearly neutral stratification the phase shift is zero in the lower wavenumber region, and as the instability increases, the region of zero phase shift extends to the higher wavenumber region and ultimately occupies almost the whole wavenumber region in the upper layer of $y/\delta = 0.81$ with strongly

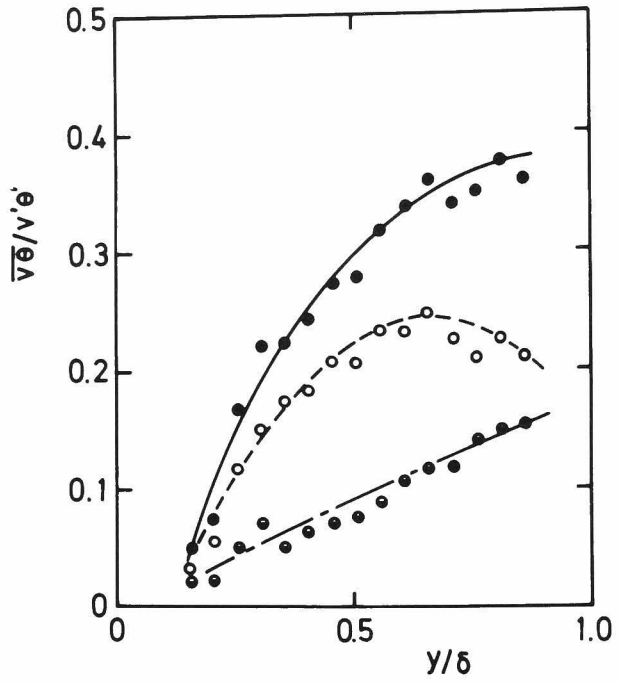

Figure 3.30. Nondimensional vertical heat flux by the intermittent eddies with negative large spikes of temperature fluctuation.

—●— $\overline{v\theta}/v'\theta'$ in figure 3.16 by whole eddies.

--○-- $\overline{v\theta}_c/v'\theta'$ by the intermittent eddies.

—·●·— $\overline{v\theta}/v'\theta'$ minus $\overline{v\theta}_c/v'\theta'$.

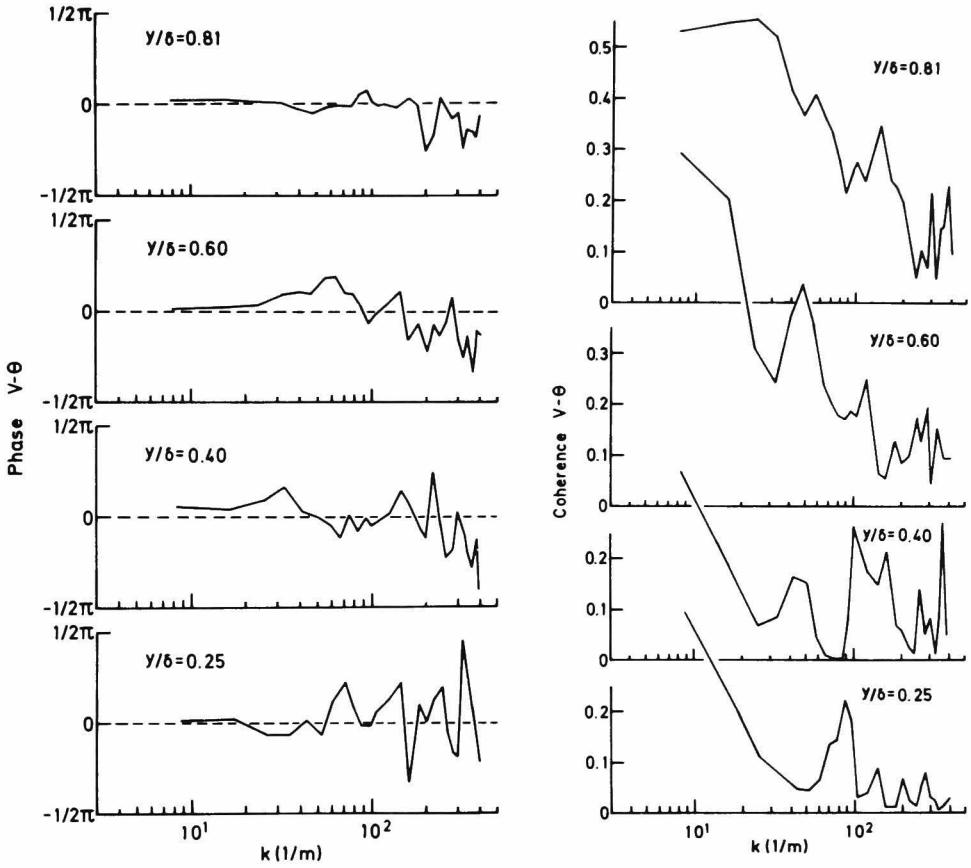

Figure 3.31. v-θ phase angles and coherences. (Run IX)

unstable stratification. The coherences also grow to higher levels with increasing instability, i.e., increasing y/δ. This behavior means that not only the large-scale eddies but also small-scale eddies are affected by the buoyancy force, and that the upward and downward motion of the eddies are enhanced by buoyancy. Thus, in the entire wavenumber region, the correlation between v and θ increases and we can see this high correlation in figures 3.16 and 3.34.

In contrast to the v-θ phase angles and coherences, the u-θ coherences become lower with increasing instability and the phase angles are scattered except in the lower wavenumber region (figure 3.32). This indicates that u and θ tend to behave independently in unstable flow.

Figure 3.33 shows the u-v phase angles and coherences. The phase angles in the lower layer of $y/\delta \lesssim 0.43$ are near $-\pi$ except in the range of high wavenumber. This shows that ordinary turbulence predominates in the lower layer of flow with weak instability. With increasing instability the coherences of u and v are reduced and at $y/\delta = 0.62$ the phase angles are very scattered and the coherences become very low. The behavior reflects the low correlation between u and v in the region near $y/\delta = 0.62$ of figure 3.11.

3.3.3 Correlation of turbulence quantities with local gradient Richardson number

From the view mentioned in subsection 2.3.3, turbulence quantities are plotted against the local gradient Richardson number in figure 3.34. Here, only the values measured in the layer of $0.4 < y/\delta < 0.75$ were adopted, since the turbulence in that layer is presumed to be free

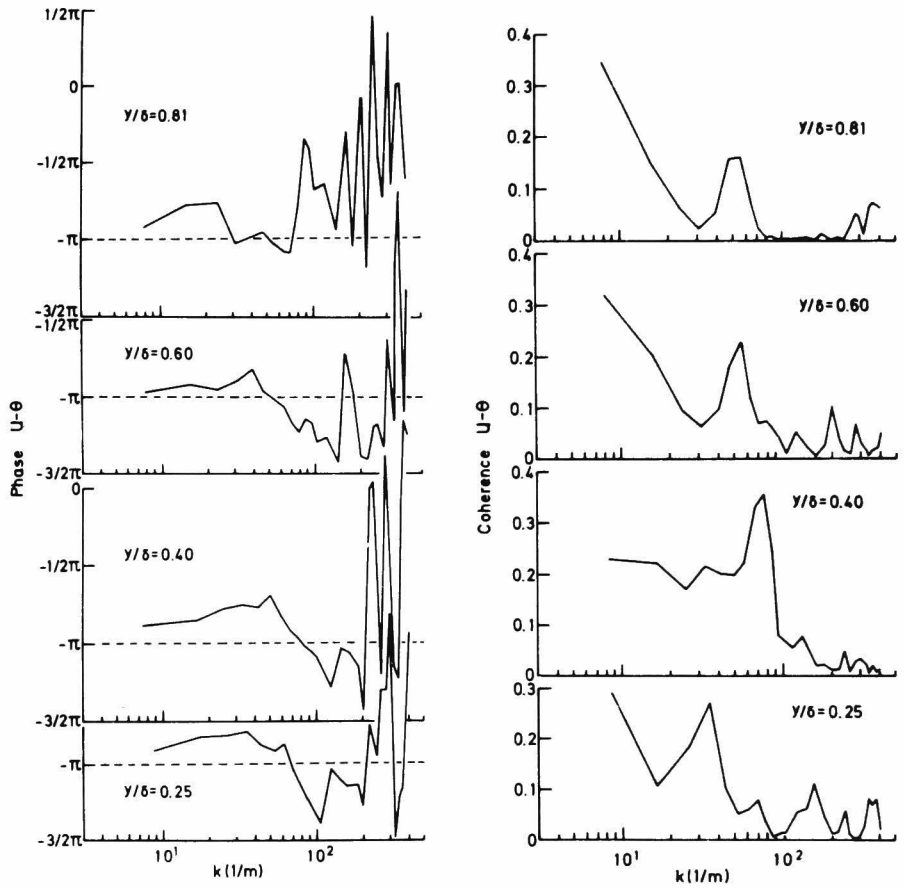

Figure 3.32. u-θ phase angles and coherences. (Run IX)

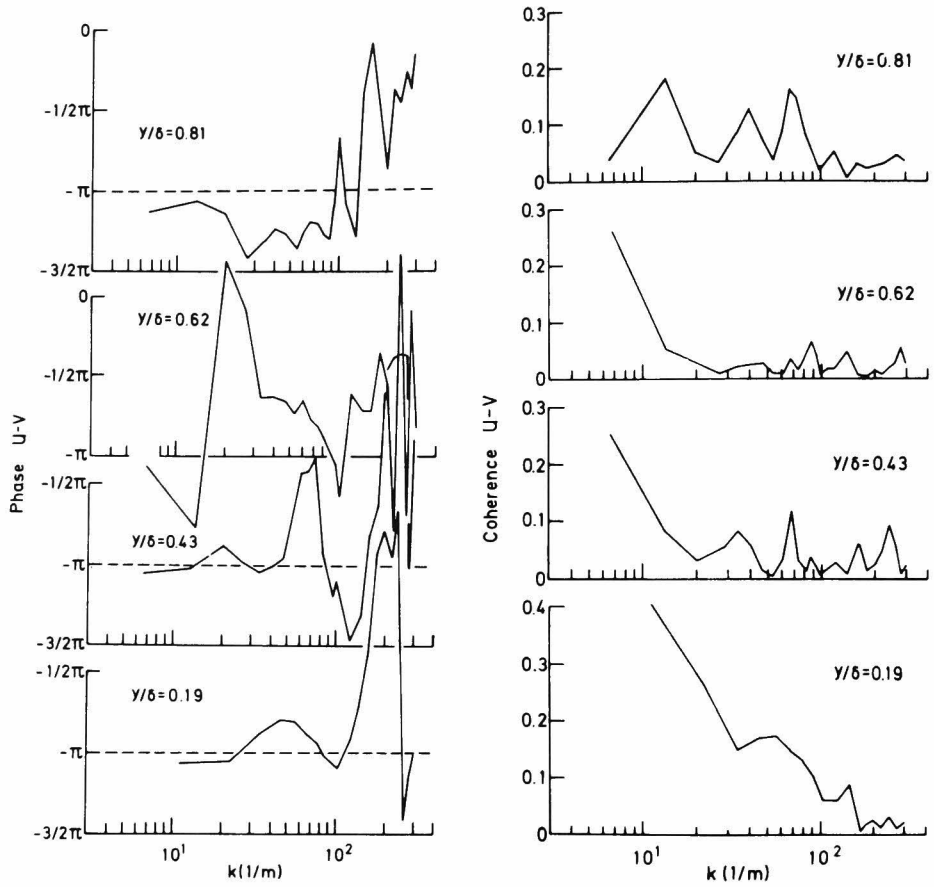

Figure 3.33. u-v phase angles and coherences. (Run IX)

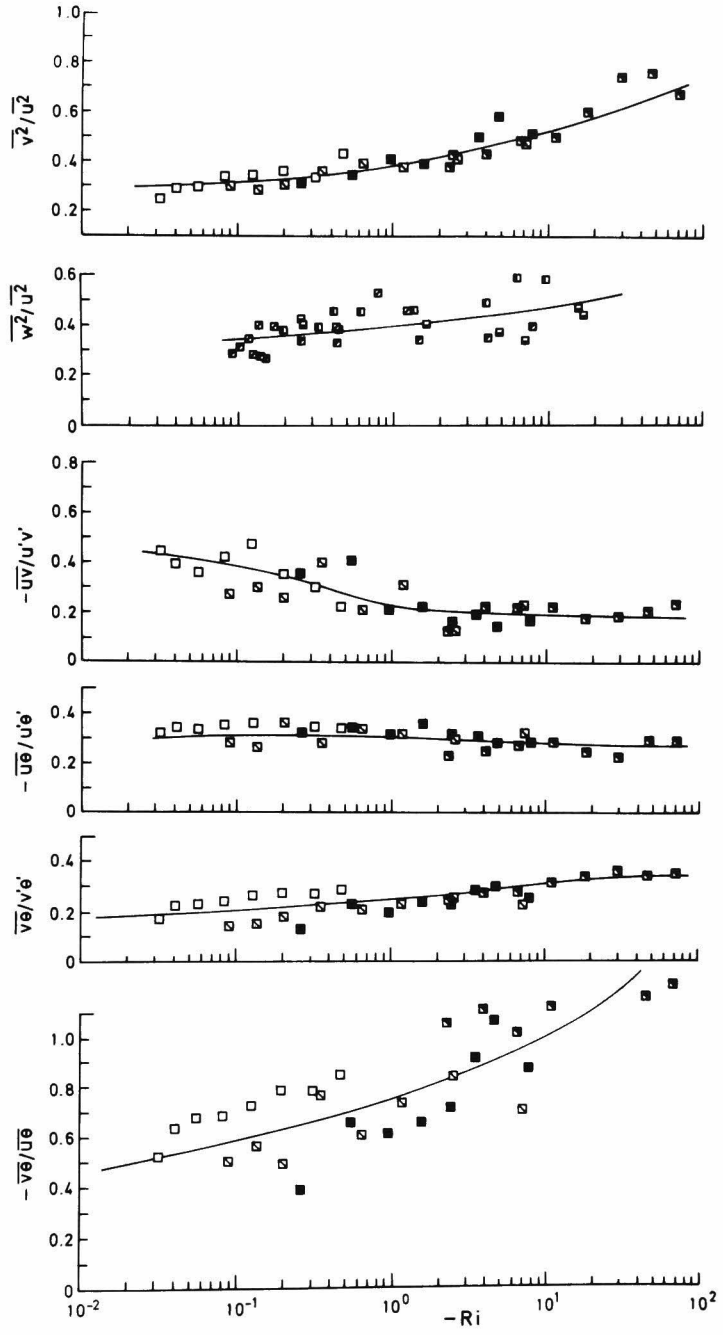

Figure 3.34. Correlation of the turbulence quantities with the local gradient Richardson number. Symbols as in table 3.1.

from the direct influences of the bottom wall and the free surface, and Ri can be more reliably estimated there.

The variations of the turbulence quantities can be well correlated by the local stability parameter Ri and do not depend on the bulk Richardson number $\overline{Ri}$ or Reynolds number Re. The ratio of the time-averaged square value of the velocity fluctuation in the vertical direction to that in the streamwise direction, $\overline{v^2}/\overline{u^2}$, increases as -Ri becomes larger, indicating that the vertical motion is enhanced with increasing instability. The ratio of $\overline{w^2}/\overline{u^2}$ also increases with increasing -Ri. The correlation coefficient of the Reynolds stress, $-\overline{uv}/u'v'$, decreases with increasing -Ri, suggesting that the motion in the streamwise direction is independent of the motion in the vertical direction, despite the promotion of turbulence motion. Similarly, the correlation of the streamwise heat flux, $\overline{u\theta}/u'\theta'$, decreases slightly with increasing instability.

In contrast to these variations, the correlation coefficient of the vertical heat flux, $-\overline{v\theta}/v'\theta'$, increases significantly with increasing -Ri. This is the most prominent feature in the unstably stratified flow. As discussed in the previous section, the turbulence structure and the turbulent transport are predominated by the upward motion of hot eddies and the downward motion of cold eddies. Thus, the ratio of the heat fluxes in the vertical and the streamwise directions, $-\overline{v\theta}/\overline{u\theta}$, increases noticeably with increasing instability and ultimately the vertical flux overcomes the streamwise flux.

Thus, the local gradient Richardson number may be regarded as the predominant parameter for representing the effects of stability also in unstably stratified flows, and the variations of the turbulence quantities as functions of Ri are expected to be universal.

3.4 Conclusion

The turbulence structure under unstably stratified conditions have been investigated in an open channel in which the thermal stratification is established by evaporation cooling with high heat flux at the free surface. Substantial changes in the turbulence structure are caused by the buoyancy-driven motion which enhances the turbulent transport. The distributions of turbulence quantities are strongly affected by the positive buoyancy, and their variations with the bulk Richardson number can be interpreted by investigating the production terms by shear and buoyancy in the respective transport equations.

In unstably stratified flow, the upward motion of the hot eddies and the downward motion of the cold eddies, or buoyancy-driven motion dominates the turbulence structure. In particular, the intermittent downward motion of the eddies with large negative spikes of temperature fluctuation are pronounced and contribute mainly to the turbulent transport of heat in the vertical direction. Thus, under strongly unstable stratification the vertical heat transfer becomes larger than that in the streamwise direction.

The local gradient Richardson number ,Ri ,is the predominant parameter for representing the effects of buoyancy on the turbulence structure in unstably stratified flows and the correlations of the turbulence quantities with Ri are universal and will offer a decisive guide for the turbulence closure problem.

CHAPTER 4 APPLICATION OF A SPECTRAL EQUATION MODEL TO STRATIFIED FLOWS

4.1 Introduction

Even with the more advanced digital computers, it is impossible to follow random fluctuations of turbulence based on the full time-dependent Navier-Stokes and energy equations. Time-averaged equations are, therefore, used for engineering calculations.
When carrying out the averaging procedure, we can see the appearance of the statistical correlations of fluctuating propertities such as turbulent momentum and heat fluxes in the equations. To make these time-averaged equations soluble, a great number of turbulence models that approximately describe these statistical correlations have been developed for various turbulent flows with forced or free convection, since Prandtl presented his mixing length model[42].

Turbulence models may be roughly divided into two types. One type is one-equation , two-equation and multi-equation turbulence models based on single-point correlation equations. Two-equation and multi-equation models have been used in most of the recent theoretical studies, e.g., Hanjalic & Launder[44], Rodi & Spalding[45], , Deardorff[14], Launder[15], Gibson & Launder[16] and others.
These models contain several empirical constants and approximated functions which can be determined only from experiments. It is, however, difficult to determine these universal constants and functions, exactly, since they may not be valid except in a restricted flow in which they were experimentally estimated.
The other type is spectral equation turbulence models based on multi-point correlation equations. The first spectral equation models have been developed by Deissler[46]. Deissler[47,48] and Fox[49] considered spectral equations based on two-point correlations

in homogeneous turbulence with low Reynolds number. The spectral equations can be easily solved under only two assumptions; the neglect of the inertial effects represented by the triple correlations and the homogeneity of the flow. The solutions of the spectral equations provide some insight into the effects of the correlations among the pressure, velocity and temperature fluctuations on the turbulent transport of momentum and heat, and into the turbulence quantities in wavenumber space. The spectral equation model, however, has a drawback that it is difficult to compare the calculated results with the experimental results in a steady state flow, since the time-dependent terms in the spectral equations cannot be neglected under the two assumptions mentioned above.

Deissler[50] has already applied the spectral equations to homogeneous stratified flow in the presence of a vertical body force due to a uniform temperature gradient. However, the calculations for the stratified turbulent flow with shear arising from the uniform velocity gradient have not yet been performed, despite great interest. In addition, the experimental results shown in chapters 2 and 3 suggest that the previous turbulence models by many workers may be inadequate for the calculation of stratified flows. It is, therefore, worthwhile to apply the spectral equations to stratified flows in the presence of the uniform temperature and velocity gradients.

The purpose of this chapter is to gain some insight into the buoyancy effects on turbulence quantities in stratified flows, by using the spectral equation model. The spectral equations were solved numerically with a large electric computer under the same assumptions as in Deissler [48]. The solution were presented as a function of the local gradient Richardson number, with a Prandtl number of 5 and a parameter τ_t of 6, and were compared with the

experimental results given in chapters 2 and 3.

4.2 Spectral Equations for Stratified Flow

4.2.1 Basic equations

Two-point correlation equations which include buoyancy effects are constructed from the Navier-Stokes, energy and continuity equations. The following correlation equations are obtained for an incompressible flow with vertical temperature and velocity gradients, under the assumptions of the homogeneity and weakness of turbulence,

$$\frac{\partial Q_{ij}}{\partial t} + \delta_{i1}Q_{2j}\frac{\partial \overline{U}}{\partial x_2} + \delta_{j1}Q_{i2}\frac{\partial \overline{U}}{\partial x_2} + \frac{\partial \overline{U}}{\partial x_2}\xi_2\frac{\partial}{\partial \xi_1}Q_{ij} = -\frac{1}{\rho}\left(\frac{\partial}{\partial \xi_i}Q_{ip} \quad \frac{\partial}{\partial \xi_i}Q_{jp}\right)$$

$$+\delta_{i2}\beta Q_{\theta j}g + \delta_{j2}\beta Q_{i\theta}g + 2\nu\frac{\partial^2 Q_{ij}}{\partial \xi_k \partial \xi_k} \quad , \tag{4-1}$$

$$\frac{\partial Q_{i\theta}}{\partial t} + Q_{i2}\frac{\partial \overline{T}}{\partial x_2} + \delta_{i1}Q_{2\theta}\frac{\partial \overline{U}}{\partial x_2} + \frac{\partial \overline{U}}{\partial x_2}\xi_2\frac{\partial}{\partial \xi_1}Q_{i\theta} = \frac{1}{\rho}\frac{\partial}{\partial \xi_i}Q_{p\theta} + \delta_{i2}\beta Q_{\theta\theta}g$$

$$+(\nu + K)\frac{\partial^2 Q_{i\theta}}{\partial \xi_k \partial \xi_k} \quad , \tag{4-2}$$

$$\frac{\partial Q_{\theta j}}{\partial t} + Q_{2j}\frac{\partial \overline{T}}{\partial x_2} + \delta_{j1}Q_{\theta 2}\frac{\partial \overline{U}}{\partial x_2} + \frac{\partial \overline{U}}{\partial x_2}\xi_2\frac{\partial}{\partial \xi_1}Q_{\theta j} = -\frac{1}{\rho}\frac{\partial Q_{\theta p}}{\partial \xi_j} + \delta_{j2}\beta Q_{\theta\theta}g$$

$$+(\nu + K)\frac{\partial^2 Q_{\theta j}}{\partial \xi_k \partial \xi_k} \tag{4-3}$$

and

$$\frac{\partial Q_{\theta\theta}}{\partial t} + Q_{\theta 2}\frac{\partial \overline{T}}{\partial x_2} + Q_{2\theta}\frac{\partial \overline{T}}{\partial x_2} + \frac{\partial \overline{U}}{\partial x_2}\xi_2\frac{\partial}{\partial \xi_1}Q_{\theta\theta} = 2K\frac{\partial^2 Q_{\theta\theta}}{\partial \xi_k \partial \xi_k} \quad , \tag{4-4}$$

where repeated indices mean the summation convention.

Expressions for the pressure-velocity and the pressure-temperature correlations are obtained by taking the divergence of the equation of motion.

$$\frac{1}{\rho}\frac{\partial^2 Q_{pj}}{\partial \xi_i \partial \xi_i} = 2\frac{\partial \bar{U}}{\partial x_2}\frac{\partial Q_{2j}}{\partial \xi_1} - \beta g \frac{\partial Q_{\theta j}}{\partial \xi_2} \tag{4-5}$$

$$\frac{1}{\rho}\frac{\partial^2 Q_{ip}}{\partial \xi_j \partial \xi_j} = -2\frac{\partial \bar{U}}{\partial x_2}\frac{\partial Q_{i2}}{\partial \xi_1} + \beta g \frac{\partial Q_{i\theta}}{\partial \xi_2} \tag{4-6}$$

$$\frac{1}{\rho}\frac{\partial^2 Q_{p\theta}}{\partial \xi_i \partial \xi_i} = 2\frac{\partial \bar{U}}{\partial x_2}\frac{\partial Q_{2\theta}}{\partial \xi_1} - \beta g \frac{\partial Q_{\theta\theta}}{\partial \xi_2} \tag{4-7}$$

$$\frac{1}{\rho}\frac{\partial^2 Q_{p\theta}}{\partial \xi_j \partial \xi_j} = -2\frac{\partial \bar{U}}{\partial x_2}\frac{\partial Q_{\theta 2}}{\partial \xi_1} + \beta g \frac{\partial Q_{\theta\theta}}{\partial \xi_2} \tag{4-8}$$

In order to reduce the correlation equations to simple differential equations, the following three-dimensional Fourier transforms were introduced;

$$Q_{ij}(\mathbf{r}) = \int_{-\infty}^{\infty} E_{ij}(\boldsymbol{\kappa}) \exp(i(\boldsymbol{\kappa}\cdot\mathbf{r}))\, d\boldsymbol{\kappa} \ , \tag{4-9}$$

$$Q_{\theta j}(\mathbf{r}) = \int_{-\infty}^{\infty} E_{\theta j}(\boldsymbol{\kappa}) \exp(i(\boldsymbol{\kappa}\cdot\mathbf{r}))\, d\boldsymbol{\kappa} \ , \tag{4-10}$$

$$Q_{i\theta}(\mathbf{r}) = \int_{-\infty}^{\infty} E_{i\theta}(\boldsymbol{\kappa}) \exp(i(\boldsymbol{\kappa}\cdot\mathbf{r}))\, d\boldsymbol{\kappa} \tag{4-11}$$

and

$$Q_{\theta\theta}(\mathbf{r}) = \int_{-\infty}^{\infty} E_{\theta\theta}(\boldsymbol{\kappa}) \exp(i(\boldsymbol{\kappa}\cdot\mathbf{r}))\, d\boldsymbol{\kappa} \ , \tag{4-12}$$

where $\boldsymbol{\kappa}$ is the wavenumber vector and $\mathbf{r}$ the distance vector from point A to point B $(=(\xi_1, \xi_2, \xi_3))$.

Substituting equations (4-5) (4-8) into equations (4-1) (4-4) and taking the Fourier transform, we can obtain the following differential equations with the nondimensional forms denoted in the list of symbols.

$$\frac{\partial E_{ij}}{\partial \tau} = \underbrace{\{\delta_{i1}E_{2j}+\delta_{j1}E_{i2}\}}_{I} + \underbrace{\{[k_j-\delta_{j2}k_1\tau][2k_1E_{i2}-Ri(k_2-k_1\tau)\tau_t E_{i\theta}]/\omega^2}_{II}$$

$$\underbrace{+\ [k_i-\delta_{i2}k_1\tau][2k_1E_{2j}-Ri(k_2-k_1\tau)\tau_t E_{\theta j}]/\omega^2\}}_{II} + \underbrace{\{\delta_{i2}Ri\tau_t E_{\theta j}}_{III}$$

$$\underbrace{+\ \delta_{j2}Ri\tau_t E_{i\theta}\}}_{III}\ \underbrace{2\omega^2 E_{ij}/\tau_t}_{IV} \qquad (4\text{-}13)$$

$$\frac{\partial E_{i\theta}}{\partial \tau} = \underbrace{-\{E_{i2}/\tau_t+\delta_{i1}E_{2\theta}\}}_{I} + \underbrace{\{[k_i-\delta_{i2}k_1\tau][2k_1E_{2\theta}-Ri(k_2\ k_1\tau)\tau_t E_{\theta\theta}]/\omega^2\}}_{II}$$

$$\underbrace{+\ \{\delta_{i2}Ri\tau_t E_{\theta\theta}\}}_{III}\ \underbrace{\{[1+\tfrac{1}{Pr}]\omega^2 E_{i\theta}/\tau_t\}}_{IV} \qquad (4\text{-}14)$$

$$\frac{\partial E_{\theta j}}{\partial \tau} = \underbrace{-\{E_{2j}/\tau_t+\delta_{j1}E_{\theta 2}\}}_{I} + \underbrace{\{[k_j-\delta_{j2}k_1\tau][2k_1E_{2j}-Ri(k_2-k_1\tau)\tau_t E_{\theta\theta}]/\omega^2\}}_{II}$$

$$\underbrace{+\{\delta_{j2}Ri\tau_t E_{\theta\theta}\}}_{III}\ \underbrace{\{[1+\tfrac{1}{Pr}]\omega^2 E_{\theta j}/\tau_t\}}_{IV} \qquad (4\text{-}15)$$

$$\frac{\partial E_{\theta\theta}}{\partial \tau} = \underbrace{\{[E_{\theta 2}+E_{2\theta}]/\tau_t\}}_{I}\ \underbrace{\{2\omega^2 E_{\theta\theta}/Pr\cdot\tau_t\}}_{IV} \qquad (4\text{-}16)$$

In equations(4-13)-(4-16), $\omega = [k_1^2+(k_2\ k_1\tau)^2+k_3^2]^{1/2}$ and Ri denotes the local gradient Richardson number and the meaning of the terms in the equations may be described as follows,

I = mean field term : production or extraction by vertical uniform velocity gradient or temperature gradient

II= pressure-force term : production or extraction by pressure-force of turbulence

III= buoyancy term : production or extraction by buoyancy

IV= dissipation term : dissipation

If we assume that the turbulence is isotropic at an initial time $t=t_0$, and $Q_{\theta j}$, $Q_{i\theta}$ and $Q_{\theta\theta}$ are equal to zero at $t=t_0$, we obtain the following initial conditions for the spectrum functions(see Deissler [48]).

$$E_{ij} = (\delta_{ij}\omega^2 - k_i k_j) \qquad \text{at } \tau=0 \tag{4-17}$$

$$E_{i\theta}=E_{\theta j}=E_{\theta\theta} = 0 \qquad \text{at } \tau=0 \tag{4-18}$$

Thus, equations (4-13)-(4-16) can be numerically solved with the initial conditions of equations (4-17) and (4-18).

When letting $r=0$ in equations (4-9)-(4-12) and integrating E_{ij}, $E_{i\theta}$, $E_{\theta j}$ and $E_{\theta\theta}$ over the surface of a sphere of radius ω, we obtain the following spectra averaged over all directions in wavenumber space.

$$S_{ij} = \int_0^{\pi} \int_0^{2\pi} E_{ij}\omega^2 \sin\gamma \, d\phi d\gamma \tag{4-19}$$

$$S_{i\theta} = \int_0^{\pi} \int_0^{2\pi} E_{i\theta}\omega^2 \sin\gamma \, d\phi d\gamma \tag{4-20}$$

$$S_{\theta\theta} = \int_0^{\pi} \int_0^{2\pi} E_{\theta\theta}\omega^2 \sin\gamma \, d\phi d\gamma \tag{4-21}$$

Furthermore, the integration of the spectra in equations (4-19)-(4-21) from $\omega=0$ to ∞ gives the following time-averaged quantities,

$$\overline{u_i u_j} = \frac{J_0}{\nu^{5/2}(t_t - t_0)^{5/2}} \int_0^\infty S_{ij}\, d\omega \quad , \tag{4-22}$$

$$\overline{u_i \theta} = \frac{J_0 b}{\nu^{5/2}(t_t - t_0)^{3/2}} \int_0^\infty S_{i\theta}\, d\omega \tag{4-23}$$

and

$$\overline{\theta^2} = \frac{J_0 b^2}{\nu^{5/2}(t_t - t_0)^{1/2}} \int_0^\infty S_{\theta\theta}\, d\omega \cdot \tag{4-24}$$

4.2.2 Determination of parameters

Calculations were performed for the Richardson numbers ranging from 1 to 0.3 and the Prandtl number of 5. The range of the local gradient Richardson number was arbitrarily selected so as to avoid the range of $Ri \gtrsim 0.3$ in which the time-averaged turbulence quantities show vibrating behavior and the value of Pr=5 was selected so as to correspond to the value of the water at the averaged temperature of 313K in the stratified flows discussed in chapters 2 and 3. It is difficult to determine a value of τ_t at which the computation is terminated and the calculated results are compared with experimental ones in a steady state flow. In this study, τ_t was determined from the comparison between the computed velocity correlation values at Ri=0 and the measured ones in neutral flows. The velocity correlation values in the fully turbulent channel flow measured by Laufer[51] and Nakagawa et al.[52] and the values of τ_t at which the calculated values agree with their experimental results are shown in table 4.1. In this study, the averaged value of τ_t = 6 was used for

Table 4.1. Values of τ_t corresponding to the experimental results.

	$\overline{u_1^2}/\frac{1}{3}\overline{u_i u_i}$	$\overline{u_2^2}/\frac{1}{3}\overline{u_i u_i}$	$\overline{u_3^2}/\frac{1}{3}\overline{u_i u_i}$	$-\overline{u_1 u_2}/\frac{1}{3}\overline{u_i u_i}$
by Laufer[51]	1.58	0.64	0.78	0.44
τ_t	4.80	3.10	11.3	4.30
by Nakagawa et al.[52]	1.74	0.49	0.77	0.51
τ_t	6.30	3.80	11.3	4.30

all calculations.

4.2.3 Method of calculation

Solutions of the differential equations (4-13)-(4-16) were numerically obtained by using the Kutta-Merson method by Lukenhart [53]. The integrations of equations (4-19)-(4-24) were calculated by a simple trapezoidal formula. Very small error due to the numerical calculations was accepted because it takes a vast computation time to gain a very high accuracy.

4.3 Results and Discussion

4.3.1 Turbulence kinetic energy and time-averaged square values of velocity and temperature fluctuations

Figure 4.1 shows the distributions of the turbulence kinetic energy $\overline{q^2}/2(=(\overline{u^2}+\overline{v^2}+\overline{w^2})/2)$ normalized by that ,$\overline{q_n^2}$, in neutral conditions and the time-averaged square values of the velocity fluctuations normalized by $\overline{q^2}/2$.

In stable conditions, the turbulence kinetic energy decreases with increasing stability. This is mainly due to the decrease of the shear production term in the energy equation, as shown in figure 4.2. The buoyancy production term works so as to extract turbulence energy in the range of $Ri \lesssim 0.16$, and at more stable range it contributes to the production of it, as seen from figure 4.2. However, the contributions of the buoyancy term to $\overline{q^2}/2$ are small in comparison with the shear production and viscous dissipation, because the buoyancy term contributes primarily to the variation

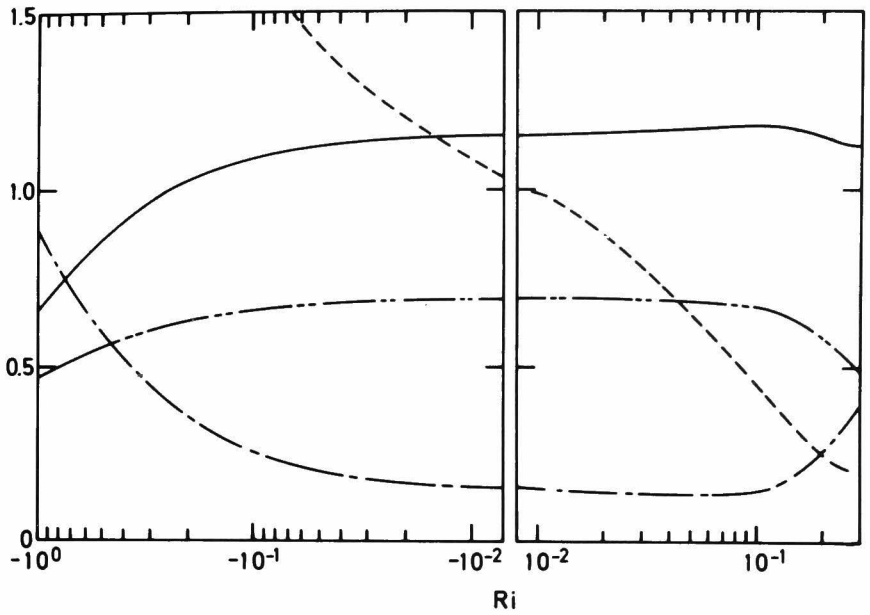

Figure 4.1. Distributions of turbulence kinetic energy and the time-averaged square values of velocity fluctuations.

- – – – – $\overline{q^2}/\overline{q_n^2}$
- ——— $\overline{u^2}/\frac{1}{2}\overline{q^2}$
- — – — $\overline{v^2}/\frac{1}{2}\overline{q^2}$
- —··— $\overline{w^2}/\frac{1}{2}\overline{q^2}$

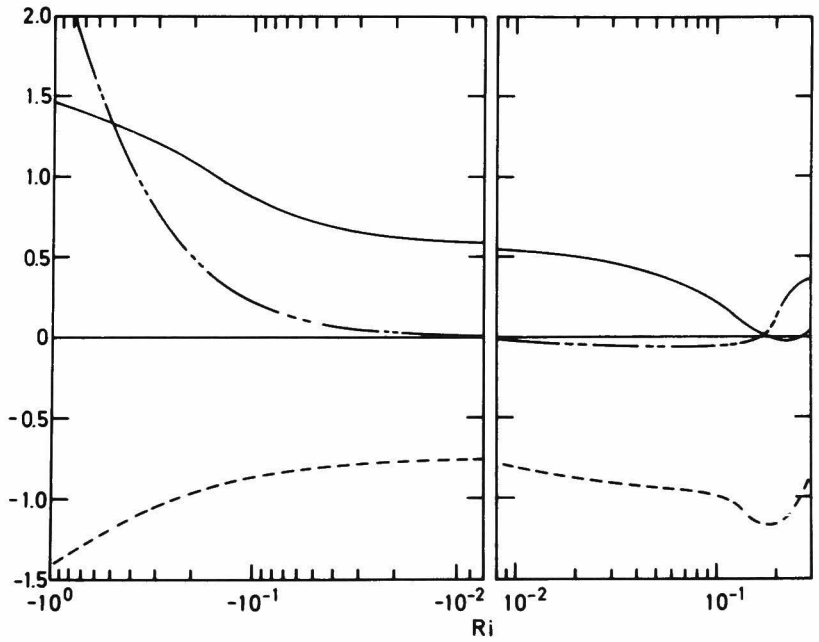

Figure 4.2. Distributions of the contribution terms to turbulence kinetic energy.

- ——— mean-field term/$\frac{1}{2}\overline{q^2}$ (production by shear)
- — – — buoyancy term/$\frac{1}{2}\overline{q^2}$
- — — — dissipation term/$\frac{1}{2}\overline{q^2}$

of $\overline{v^2}$ which has small values in comparison with $\overline{u^2}$ and $\overline{w^2}$. The increase of $\overline{v^2}/(\overline{q^2}/2)$ in the range of $Ri \gtrsim 0.1$ is, therefore, due to the buoyancy term. These results are in qualitative agreement with the experimental results deduced from the measured values shown in figures 2.7 2.10.

In unstable conditions $\overline{q^2}/\overline{q_n^2}$ increases remarkably with increasing instability, mainly due to the increases of the shear production and buoyancy production, as shown in figure 4.2. In the strongly unstable range the buoyancy term becomes very large. This behavior can be seen also in the experimental distributions in figure 3.7. However , the measured values of shear production shown in figure 3.8 exhibit the gradual decreasing behavior contrary to the present trend of the calculated values. This is presumed to be due to the inadequate assumptions used in the spectral equations, for example, an assumption of the uniform velocity gradient, because in the actual unstable flow the mean velocity gradient is not uniform and becomes small due to the intense vertical mixing by buoyancy.

Figure 4.3 shows the distributions of the pressure-force terms which indicate the redistributions of the turbulence energy between the three velocity components. In stable conditions, the energy of $\overline{u^2}$ produced by mean shear is redistributed mainly to $\overline{w^2}$ and in the more stable range of $0.15 \lesssim Ri \lesssim 0.3$ the energy of $\overline{v^2}$ produced by buoyancy is redistributed to $\overline{u^2}$ and $\overline{w^2}$.
In unstable conditions the energy of $\overline{u^2}$ and $\overline{v^2}$ produced by shear and buoyancy is redistributed to $\overline{w^2}$. In the strongly unstable range the energy transfer occurs mostly from $\overline{v^2}$ to $\overline{w^2}$ as seen from figure 4.3.

Figure 4.4 shows the distributions of the time-averaged square value of temperaure fluctuation normalized by that ,$\overline{\theta_n^2}$, in neutral

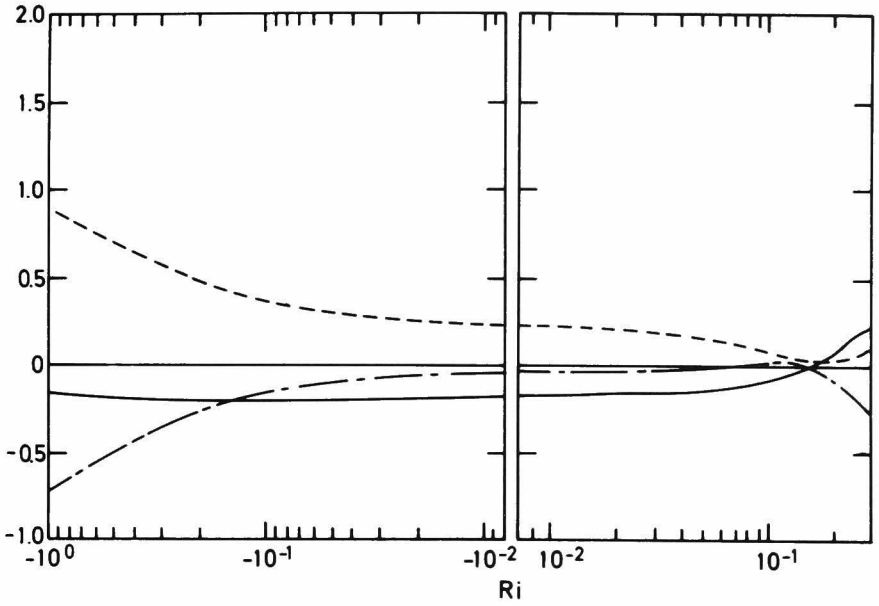

Figure 4.3. Distributions of the pressure-force terms in the the respective transport equations of normal stress.

——— pressure-force term of $\overline{u^2}/\frac{1}{2}\overline{q^2}$

—·—— pressure-force term of $\overline{v^2}/\frac{1}{2}\overline{q^2}$

– – – – pressure-force term of $\overline{w^2}/\frac{1}{2}\overline{q^2}$

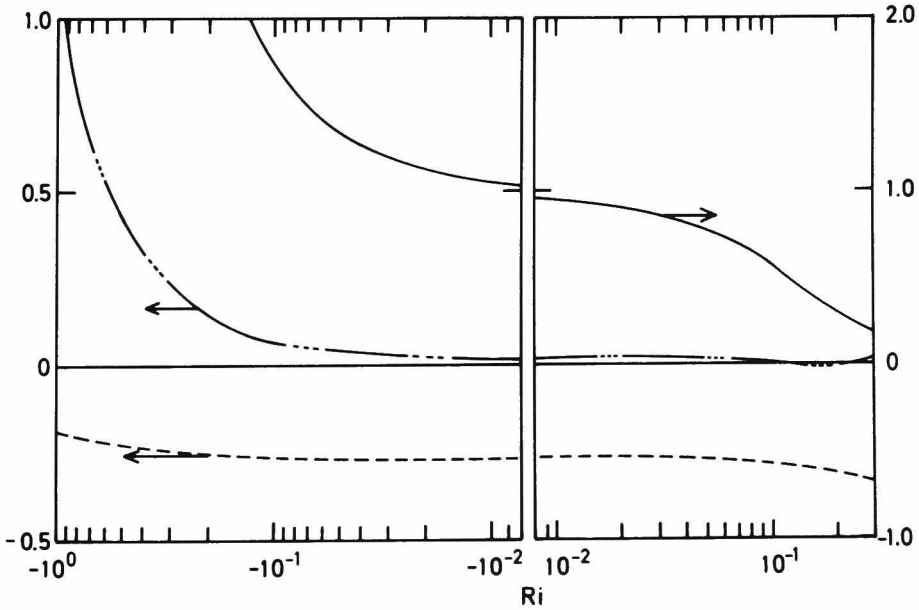

Figure 4.4. Distributions of the time-averaged square value of temperature fluctuation, $\overline{\theta^2}$, and its contribution terms.

——————— $\overline{\theta^2}/\overline{\theta_n^2}$

———·——— mean-field term/$\overline{\theta^2}$ (production by mean temperature gradient)

— — — — — dissipation term/$\overline{\theta^2}$

conditions and the contribution terms normalized by $\overline{\theta^2}$. In stable conditions, the value of $\overline{\theta^2}/\overline{\theta_n^2}$ decreases with increasing stability and, in unstable conditions, increases remarkably due to the increase of the production by mean temperature gradient.

To discuss the changes of turbulent fluctuations with stability in wavenumber space, the spectra of $\overline{u^2}$, $\overline{v^2}$, $\overline{w^2}$ and $\overline{\theta^2}$ are shown in figures 4.5 4.8. The area under the spectral curves decreases monotonously with increasing stability and the peak of the spectra moves towards the lower wavenumber region with increasing stability. However, the shape of $\overline{v^2}$-spectrum at Ri=0.3 is characteristic and a secondary peak appears in the high wavenumber region. This is clearly found to be due to the buoyancy production in the high wavenumber region, as shown in figure 4.9, but physical mechanism of the appearance of the secondary peak cannot be clarified. This seems to be a phenomenon caused by the wavelike motion, as inferred from the turbulence structure discussed in subsection 2.3.2.

4.3.2 Correlation coefficient of the Reynolds stress and streamwise and vertical heat fluxes

Figure 4.10 shows the distributions of the correlation coefficient of the Reynolds stress and the contribution terms in the transport equation of $-\overline{uv}$.

The correlation coefficient decreases remarkably with increasing stability and has almost zero or small negative value in the strongly stable range near Ri=0.2, mainly due to the increasing extraction by buoyancy. This behavior can also be seen in the experimental results shown in subsection 2.3.1.

The dissipation and the extraction by the pressure-force term

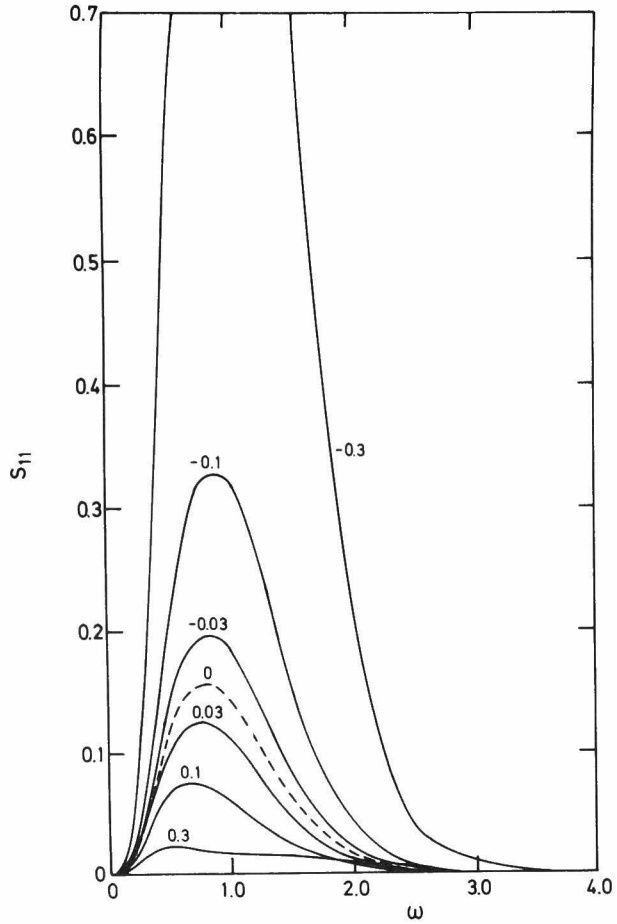

Figure 4.5. Dimensionless spectra of u.
Numbers denote the values of Ri.

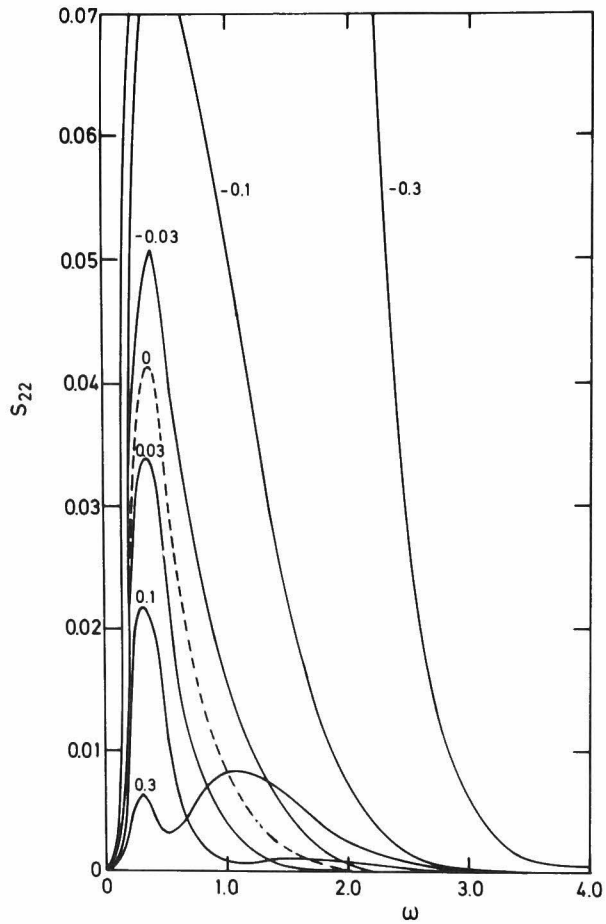

Figure 4.6. Dimensionless spectra of v.
Numbers denote the values of Ri.

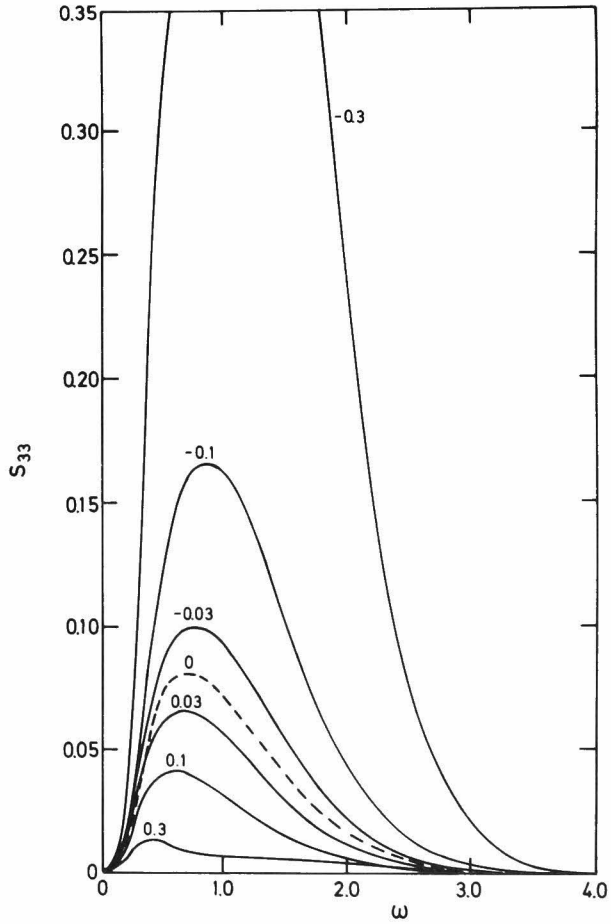

Figure 4.7. Dimensionless spectra of w.
Numbers denote the values of Ri.

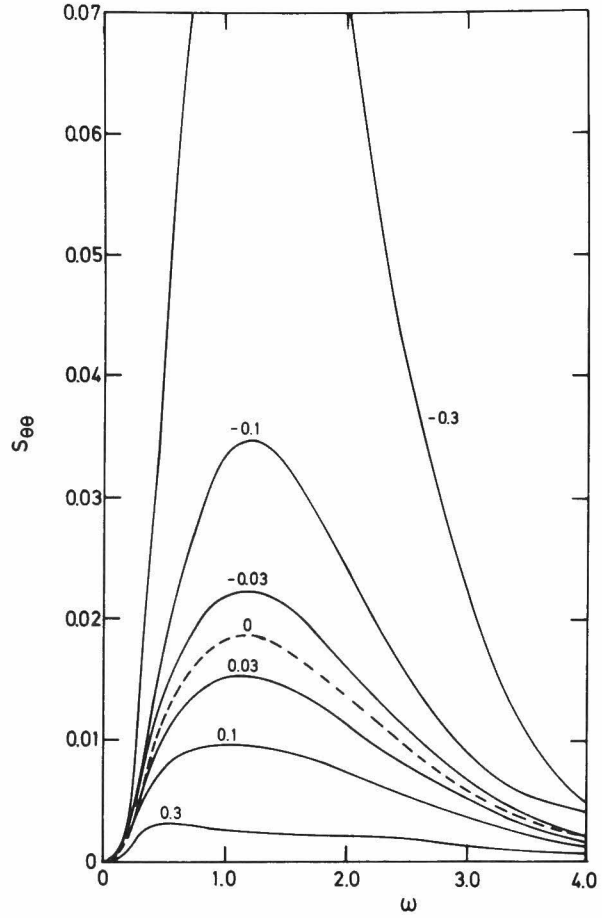

Figure 4.8. Dimensionless spectra of θ.
Numbers denote the values of Ri.

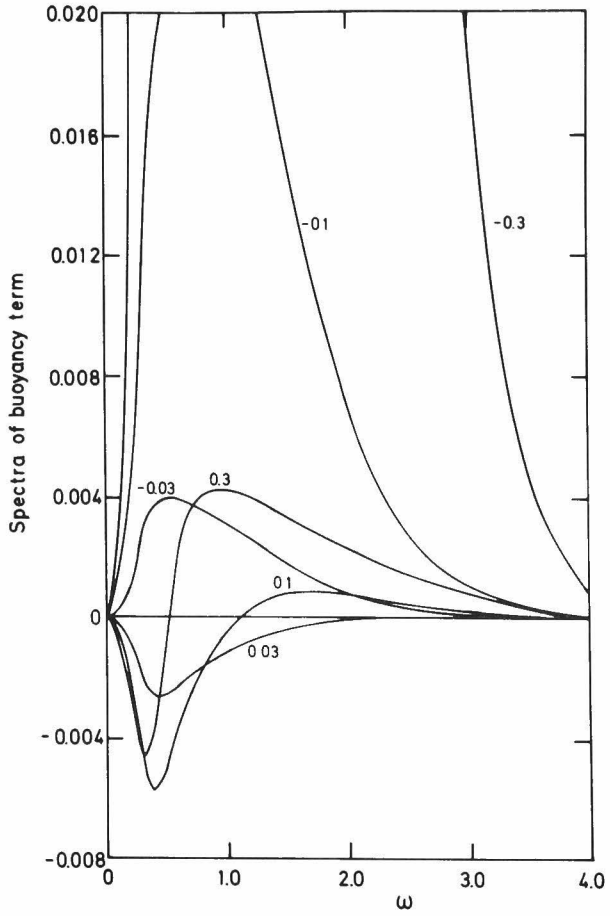

Figure 4.9. Dimensionless spectra of the buoyancy production term.
Numbers denote the values of Ri.

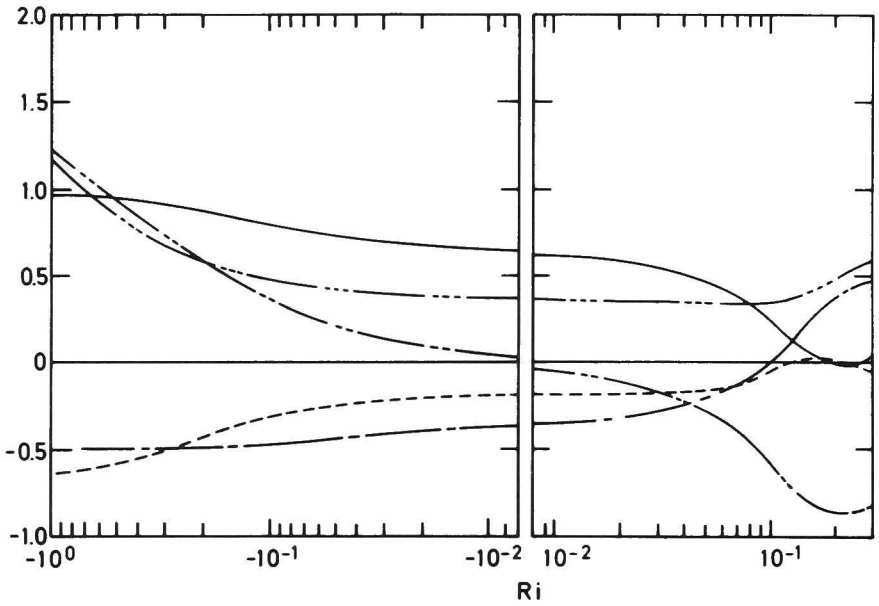

Figure 4.10. Distributions of the correlation coefficient of the Reynolds stress, $-\overline{uv}$, and its contribution terms.

———— $-\overline{uv}/u'v'$ ——- - —— pressure-force term/u'v'

—--- —— mean-field term/u'v' (production by shear) ——-- —— buoyancy term/u'v'

_ _ _ _ dissipation term/u'v'

decreases with increasing stability, and in the strongly stable range of $Ri \gtrsim 0.1$ the pressure-force term changes so as to make positive contributions to $-\overline{uv}$.

In unstable conditions, $-\overline{uv}/u'v'$ increases gradually with increasing instability. This is due to the increase of the production by buoyancy and shear. The behaviors of the correlation coefficient and shear production term in unstable flows are contrary to the measured ones(see figures 3.11 and 3.12). Although the difference cannot be clearly clarified, one of the assumptions involved in the present model, i.e., uniform velocity gradient, may be opposite to the experimental fact, as seen in figure 3.2.

The spectrum of $-\overline{uv}$ is shown in figure 4.11. It decreases with stability and , in the strongly stable range of $Ri \gtrsim 0.1$, the spectrum becomes negative in the high wavenumber region. The negative contribution to $-\overline{uv}$ attributes to the change of the sign of $-\overline{uv}$.

Figure 4.12 shows the distributions of the correlation coefficient of the streamwise heat flux and the contribution terms in the transport equation of $\overline{u\theta}$.

The correlation coefficient decreases slightly in stable conditions and in unstable conditions increases with instability.This variation may be in accordance with the production term constituted by mean temperature and velocity gradients. The spectrum of the streamwise heat flux shown in figure 4.13 exhibits the monotonous decreasing behavior with stability.

Figure 4.14 shows the distributions of the correlation coefficient of the vertical heat flux and the contribution terms in the transport equation of $-\overline{v\theta}$. The correlation coefficient of $-\overline{v\theta}$ decreases remarkably with increasing stability and crosses the zero value at $Ri \simeq 0.15$ and becomes negative in the strongly stable range of $Ri \gtrsim 0.15$.

This variation arises from the increase of the extraction by the buoyancy term and is very similar to that of $-\overline{uv}/u'v'$ showing a qualitative agreement with the experimental results (see figure 2.43).

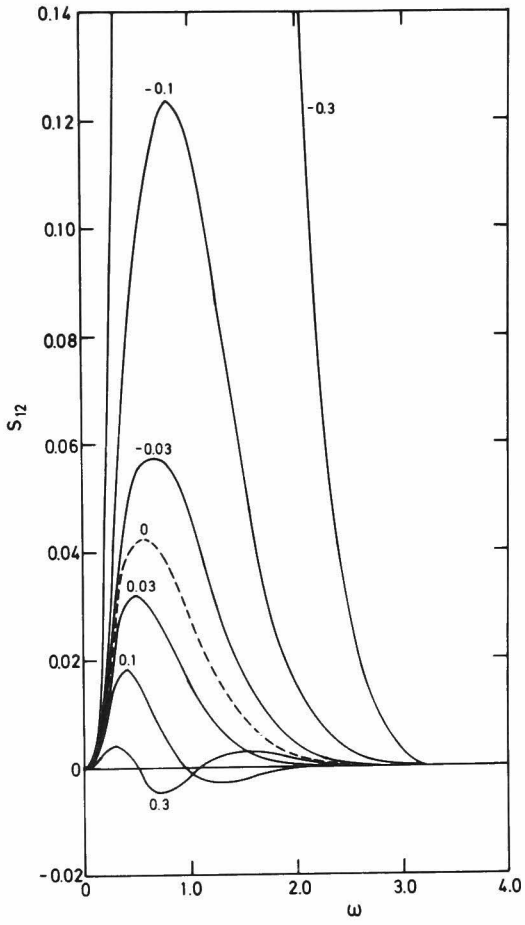

Figure 4.11. Dimensionless spectra of the Reynolds stress. Numbers denote the values of Ri.

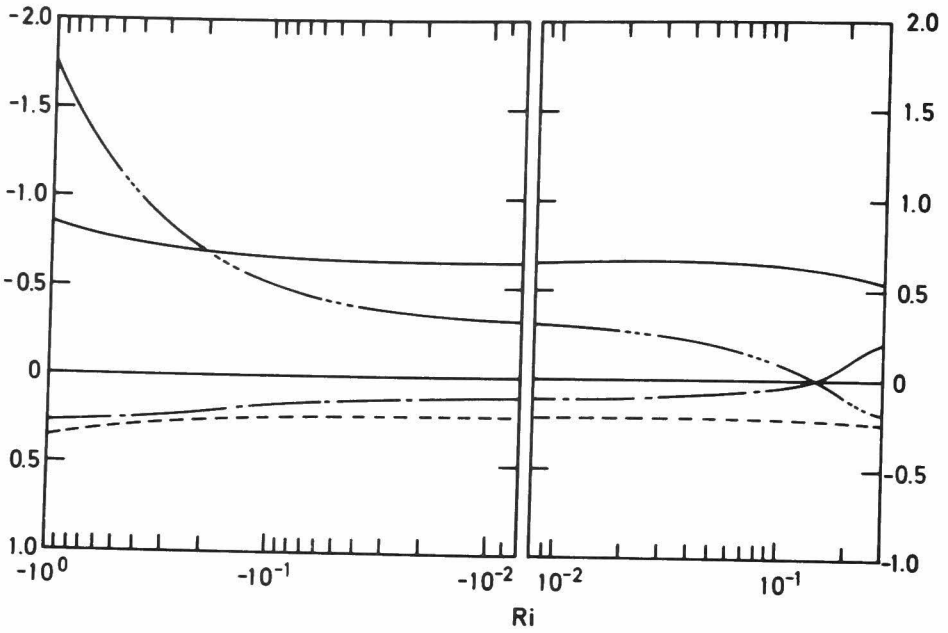

Figure 4.12. Distributions of the correlation coefficient of the streamwise heat flux, $\overline{u\theta}$, and its contribution terms.

——— $\overline{u\theta}/u'\theta'$ ——— - ——— pressure-force term/$u'\theta'$

——— mean-field term/$u'\theta'$ ——— dissipation term/$u'\theta'$

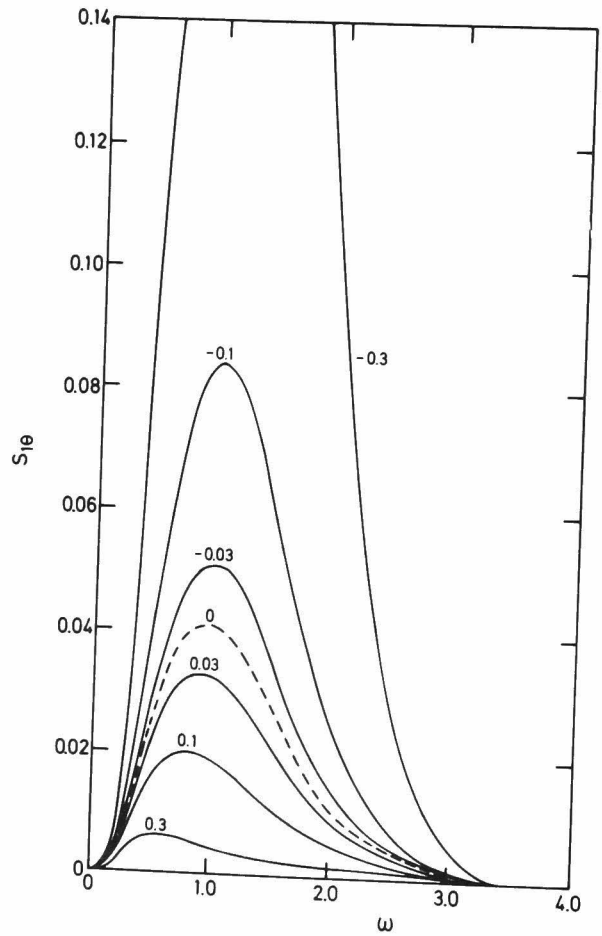

Figure 4.13. Dimensionless spectra of the streamwise heat flux. Numbers denote the values of Ri.

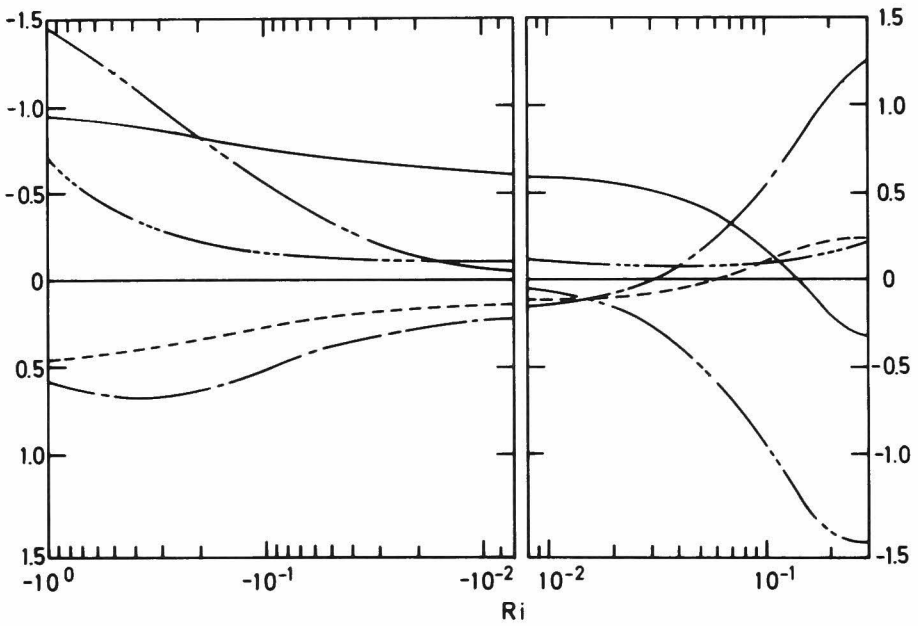

Figure 4.14. Distributions of the correlation coefficient of the vertical heat flux, $-\overline{v\theta}$, and its contribution terms.

———— $-\overline{v\theta}/v'\theta'$ ——- -—pressure-force term/$v'\theta'$

——--—— mean-field term/$v'\theta'$ —-- — buoyancy term/$v'\theta'$

(production by mean temperature gradient) — — — dissipation term/$v'\theta'$

In particular, the change of the sign of $-\overline{v\theta}/v'\theta'$ is more obvious than that of $-\overline{uv}/u'v'$ and shows that larger amounts of heat may be transferred against the mean temperature gradient. With the present spectral equations we cannot clarify the mechanisms of these turbulent transport against the mean temperature and velocity gradients, but the experimental results mentioned in chapter 2 show that the intermittent upward motion of the hot eddy with higher temperature than the mean temperature of the somewhat upper layer causes the upward heat transfer against the mean temperature gradient, and clarify the formation of the hot eddy in the inner part of the flow by taking account of the variation of the vertical heat flux in the streamwise direction, as shown in figure 2.40. If we regard the nondimensional decay time τ_t as the streamwise distance, we can see the similar variation of $-\overline{v\theta}/v'\theta'$ to the experimental result, as shown in figure 4.15. In the figure the calculation was performed for the case of the strongly stable condition with Ri=0.20.

In the upstream region of $\tau_t \lesssim 3.0$, $-\overline{v\theta}/v'\theta'$ is positive and it crosses zero at $\tau_t \simeq 0.31$ and becomes negative in the region of $\tau_t \gtrsim 0.31$, and then approaches zero gradually. This variation corresponds to the experimental results discussed in subsection 2.3.2 (see figure 2.40).

In unstable conditions $\overline{v\theta}/v'\theta'$ increases with increasing instability, mainly due to the increase of the buoyancy production. Similar behavior can also be seen in figures 3.16 and 3.17.

Figure 4.16 shows the spectrum of the vertical heat flux. It decreases in the whole wavenumber region with increasing stability and its peak moves towards the low wavenumber region. The change

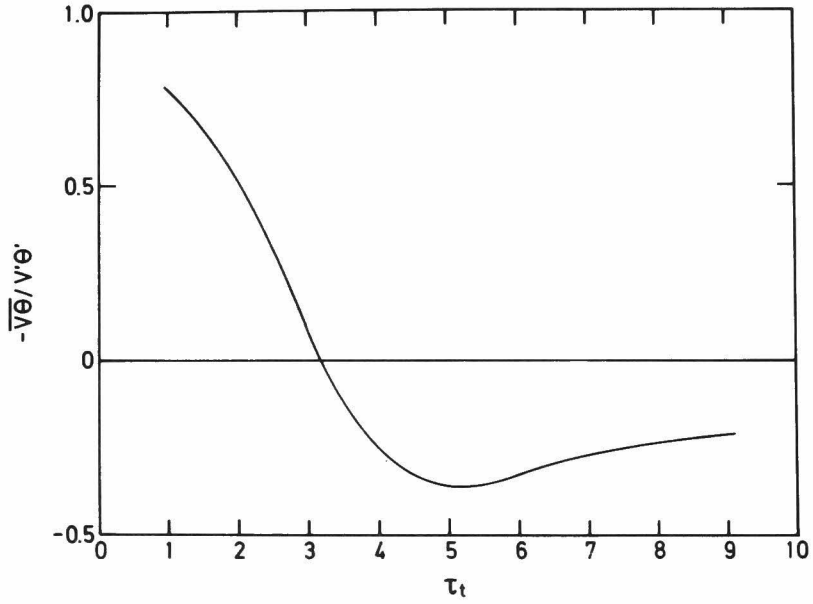

Figure 4.15. Variation of $-\overline{v\theta}/v'\theta'$ with τ_t. (Ri=0.2)

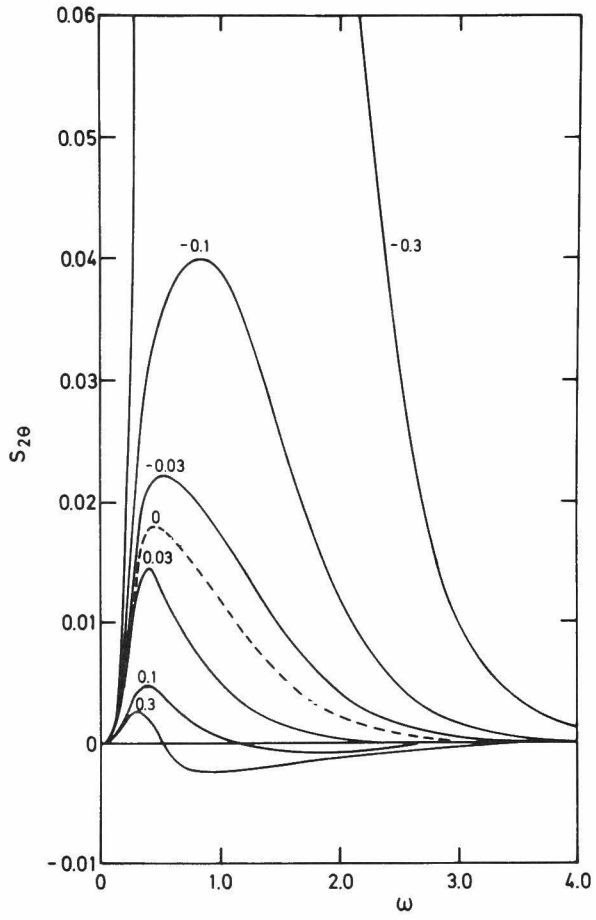

Figure 4.16. Dimensionless spectra of the vertical heat flux. Numbers denote the values of Ri.

of the sign of $-\overline{v\theta}$ at the strongly stable range is found to be attributable to the negative contribution in the high wavenumber region.

4.3.3. Reciprocal turbulent Prandtl number

Figure 4.17 shows the distributions of the reciprocal turbulent Prandtl number $\varepsilon_h/\varepsilon_m$ (the ratio of eddy diffusivity of heat to that of momentum).
In the stable range, $\varepsilon_h/\varepsilon_m$ decreases with increasing stability and reaches an unlimited negative value at $Ri \simeq 0.15$. In the further stable range of $Ri \gtrsim 0.15$ the value of $\varepsilon_h/\varepsilon_m$ oscillates discontinuously, since the value of $-\overline{uv}$ crosses the zero values.
In the unstable range, $\varepsilon_h/\varepsilon_m$ decreases with increasing instability. This $\varepsilon_h/\varepsilon_m$ behavior is in qualitative agreement with the measured values in the paper by the author[54].

4.3.4 Qualitative comparison of the calculated results with the experimental results

Figures 4.18 and 4.19 show the qualitative comparisons of the calculated values of various turbulence quantities with the experimental values in stable and unstable conditions. The variations of the calculated turbulence quantities with Ri are in good qualitative agreement with those of the measured quantities, except for the variations of $\overline{u\theta}/u'\theta'$ and $-\overline{uv}/u'v'$ in unstable conditions.

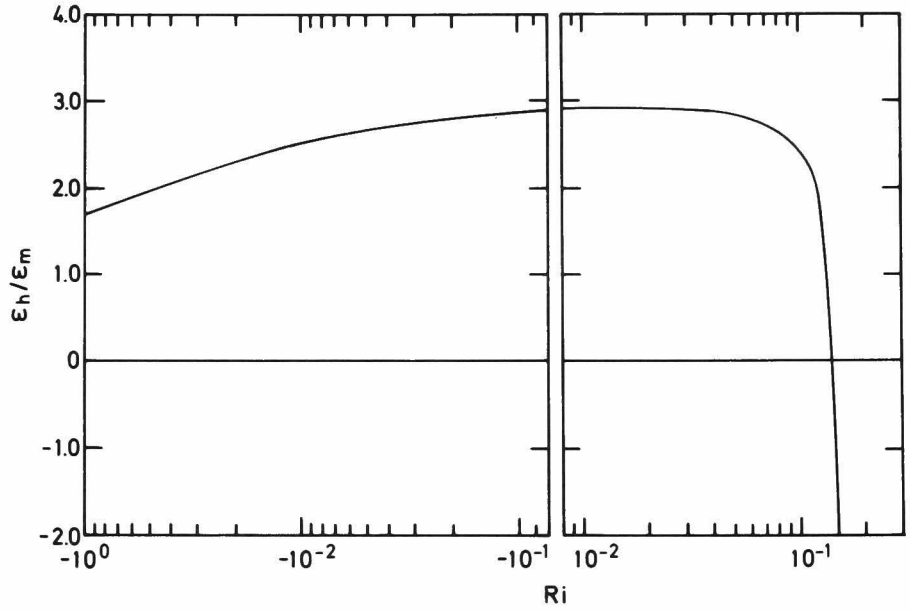

Figure 4.17. Distributions of the reciprocal turbulent Prandtl number, $\varepsilon_h/\varepsilon_m$.

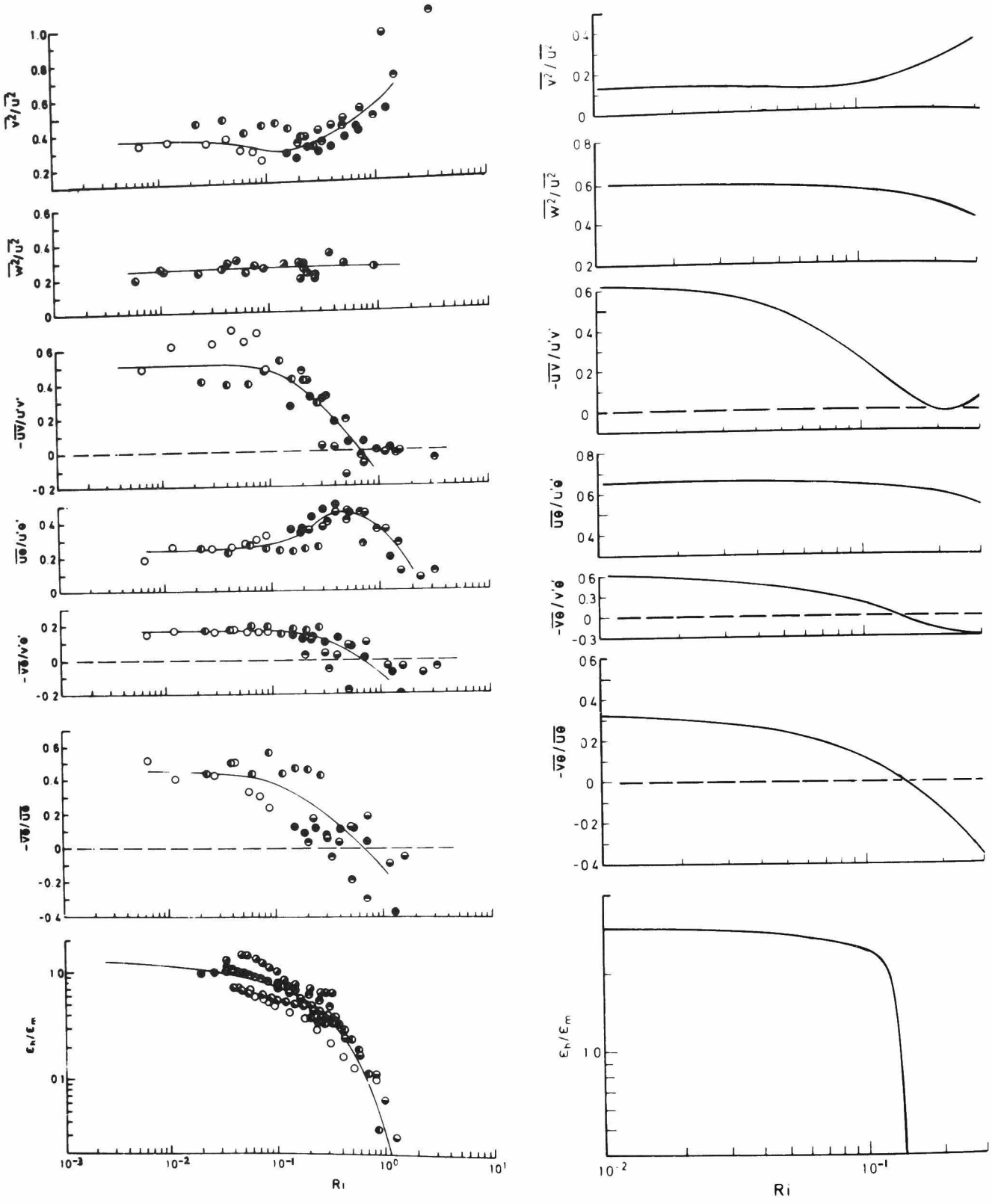

Figure 4.18. Qualitative comparisons of the calculated results with the experimental results. (in stably stratified conditions) The solid lines in the measured results represent the best fitting curves.
Symbols as in table 2.1.

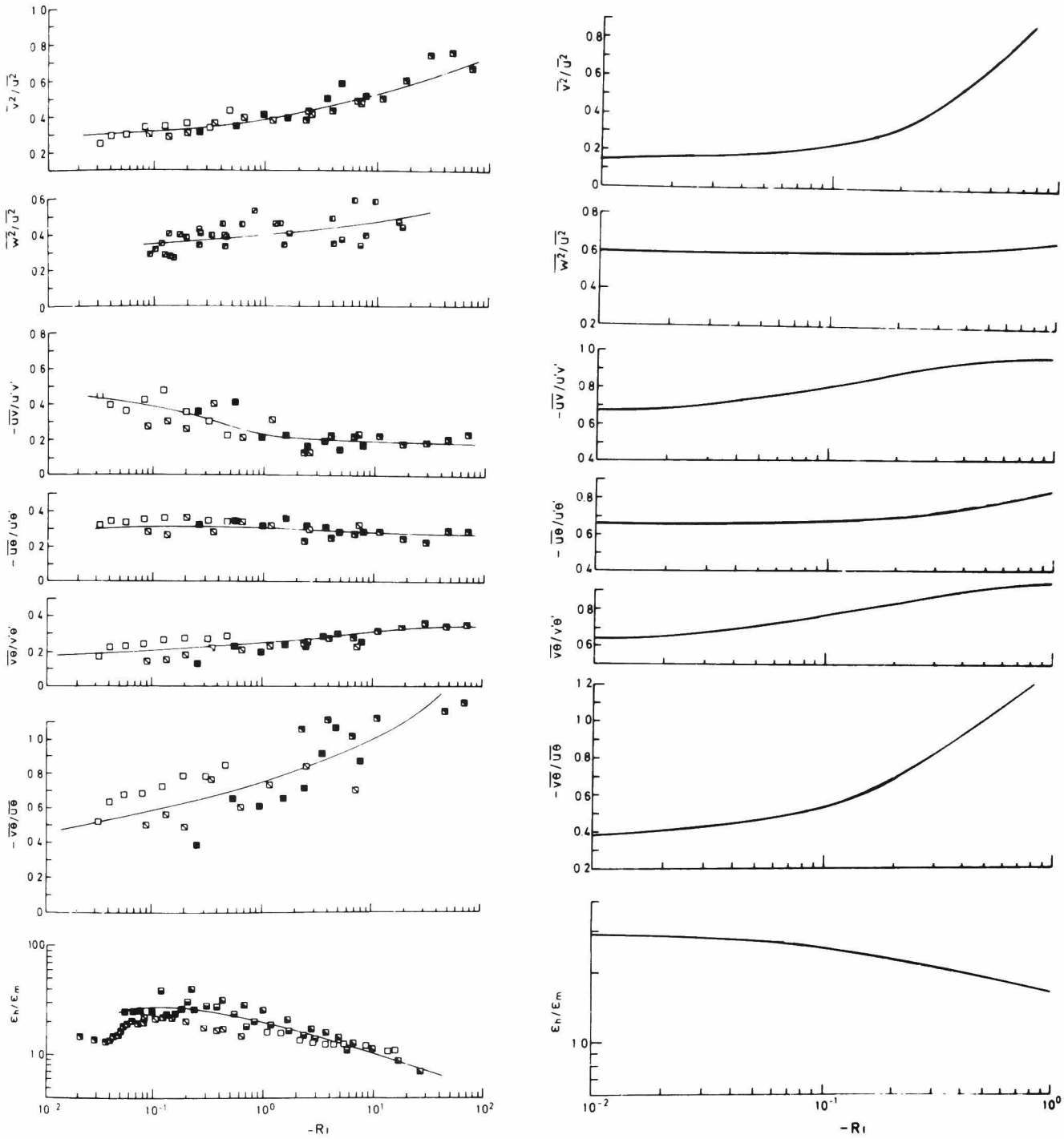

Figure 4.19. Qualitative comparisons of the calculated results with the experimental results. (in unstably stratified conditions)

The solid lines in the measured results represent the best fitting curves.

Symbols as in table 3.1.

4.4 Conclusion

In order to gain some insight into buoyancy effects, the spectral equations based on two-point correlations were applied to stratified weak turbulent shear flow. The variations of the turbulence quantities and the contribution terms involved in their transport equations have been computed as a function of a stability parameter; the local gradient Richardson number Ri, and have been compared with the measured results. The comparisons show the good qualitative agreement in stable and unstable conditions except a few quantities. In particular, the change of the sign of $-\overline{uv}$ and $-\overline{v\theta}$ is such a striking point that any other models cannot depict.

Despite this qualitative agreement, the limitation of the quantitative comparison exists in the spectral equations because of the dependence of the time-dependent parameter τ_t. Therefore, it will be expected to obtain a solution in steady state by considering the higher order correlations.

CHAPTER 5 APPLICATION OF LASER DOPPLER VELOCIMETRY TO TURBULENCE MEASUREMENT IN STRATIFIED FLOW

5.1 Introduction

Since the first successful measurement by Yeh & Cummins[55], laser Doppler velocimetry (L.D.V) has been applied to velocity and turbulence measurements in isothermal flows. Recently, L.D.V. has been applied increasingly to non-isothermal flows, including turbulent shear flow and turbulent flames.

Hong, Jones & Weinberg[56] discussed the application of L.D.V. to turbulent flames, and analysed the interaction of the test beams with moving, convoluted phase-boundaries of the flames. In non-isothermal turbulent flow, however, the laser beams encounter a succession of hot and cold pockets formed by turbulent eddies of various sizes and various temperatures, which modify the phase and direction of the laser beams, and result in a measured apparent velocity. The correction for such interaction effects needs to be determined experimentally, owing to the lack of detailed knowledge of the turbulence.

The purpose of this chapter is to supply an experimental method for estimating and correcting the interaction effect in such non-isothermal flows as stratified flows discussed in chapters 2 and 3, and to discuss the extent of the correction to turbulence measurements made in stratified flow in open channel. Among many turbulence parameters, the present discussion is confined to the measurements of turbulence intensities and power spectral density functions of the Eulerian time correlations at a fixed point in the stratified flow in open channel.

5.2 Experimental Method and Data Reduction Procedure

The measuring and the data reduction system and experimental apparatus used here are also the same described in subsection 2.2.1. A laser Doppler velocimeter(DISA 55L01,55L15,55L20, Mark I system) with an acousto-optic cell (DISA 55L02) and a constant-current thermometer (DISA 55M system) with a cold film probe (Thermo-Systems Inc., model 1264) were used for measuring fluctuating velocity and temperature. Two laser beams were focused by a 600mm lens to a diameter of about 7.44×10^{-4} m. The beam intersection angle was 4.4°. The flow was a thermally stably stratified turbulent flow in a two-dimensional open channel with cross section 0.3m wide and 0.06m high(see section 2.2). The two laser beams intersected on the centerline of the channel at a distance y from the channel floor of about 0.028m.

The output from L.D.V. and the thermometer were digitized at the rate of 100 per second and stored on magnetic tape. They were processed statistically by a computer in the Kyoto University Computer Centre. In order to take into account the drop-out of the L.D.V. signal, the standard Fourier transform relation with a Hanning lag-window weighing function (Bendat & Piersol[22]) was used. The sampling interval , the maximum number of correlation lag value and the sample size were 0.01s, 500 and about 10000, respectively.

Mesurements were made for the flows at two different degrees of thermal stratification, i.e., for local gradient Richardson numbers equal to 0.54 and 1.45, respectively. The Reynolds number and the flow depth were held constant at Re=12000 and δ=0.04m, respectively. At the intersection point the temperature and velocity gradients were 124K/m and $0.84s^{-1}$ for Ri=0.54 and 362K/m and $1.05s^{-1}$ for

Ri=1.45, respectively. The r.m.s. value of temperature fluctuation was 0.52K for Ri=0.54 and 1.1K for Ri=1.45. Details of the flow structure are described in chapter 2.

5.3 Turbulence Intensities and Power Spectra

Let the apparent velocity in the i-direction, U_{ia}, measured by L.D.V. consist of the real flow velocity, U_{ir}, and the fictitious velocity, U_{if}, due to the interaction of the light beam with temperature fluctuations. Then

$$U_{ia}=U_{ir}+U_{if}=\overline{U}_{ir}+\overline{U}_{if}+u_{ir}+u_{if}=\overline{U}_{ia}+u_{ia}\ , \tag{5-1}$$

where the overbar denotes the time-averaged and small letters represent the fluctuating values. The turbulent intensities and the power spectral density functions of the real velocity fluctuations are calculated from the following equations:

$$(\overline{u_{ir}^2})^{1/2}=(\overline{u_{ia}^2}-\overline{u_{if}^2}\quad 2\overline{u_{ir}u_{if}})^{1/2}\ , \tag{5-2}$$

$$S_{rr}(f)=S_{aa}(f)\quad S_{ff}(f)\quad S_{rf}(f)-S_{fr}(f), \tag{5-3}$$

where S_{rr} S_{aa}, etc., denote the spectral functions of $\overline{u_{ir}(t)u_{ir}(t-\tau)}$, $\overline{u_{ia}(t)u_{ia}(t-\tau)}$, etc., and f in the parenthesis is the frequency.

The turbulence intensity $(\overline{u_{if}^2})^{1/2}$ and the power spectrum $S_{ff}(f)$ are calculated from the velocity u_{if} which can be determined experimentally as an apparent velocity of an obstacle held stationary at the point of intersection of the two beams, i.e., an obstacle with $u_{ir}=0$. In the present experiment, the measurement of u_{if} was

accomplished by inserting a small acrylic plate at the point of beam intersection. The plate has a streamlined leading edge and was thick enough to contain the beam intersection in it, even when the beam was moved by the Schlieren effect in the non-isothermal flow. The difference in refractive index between the acrylic plate and water may be ignored. The particles in the plate or on the surface of it behaved as stationary scattering obstacles. The acrylic plate was used rather than a single wire or fibre in order to avoid the signal drop-out condition.

Unlike the quantities $(\overline{u_{if}^2})^{1/2}$ and S_{ff}, it is impossible to determine the correlation $\overline{u_{ir}u_{if}}$ and the power spectral function S_{rf} or S_{fr} directly by experiment. The order of magnitudes of these quantities can, however, be estimated from the following equations and measurements of temperature fluctuations:

$$\overline{u_r u_f} \ (\equiv \overline{u_{1r}u_{1f}}) \lesssim \frac{1.5\alpha\Lambda^2 C_1}{n_0 \bar{U}_r \cos^2\psi} \qquad (= \overline{u_r u_f}\big|_{max}) \qquad (5\text{-}4)$$

for the streamwise component, and

$$\overline{v_r v_f} \ (\equiv \overline{u_{2r}u_{2f}}) \lesssim \frac{1.5\alpha\Lambda^2 C_2 (\overline{u_r^2})^{1/2}}{n_0 \bar{U}_r \cos^2\psi \ (\overline{v_r^2})^{1/2}} \qquad (= \overline{v_r v_f}\big|_{max}) \qquad (5\text{-}5)$$

for the vertical component, where α is the temperature dependence of the refractive index of water, Λ an integral scale, 2ψ the intersection angle, n_0 the averaged refractive index of water and C_1, C_2 the correlation values between each apparent velocity component and the second time-derivative of temperature fluctuation at the measuring point (see section 5.6).

5.4 Results and Discussion

The measured values of the turbulence intensities $(\overline{u_a^2})^{1/2}$ [$\equiv(\overline{u_{1a}^2})^{1/2}$], $(\overline{v_a^2})^{1/2}$ [$\equiv(\overline{u_{2a}^2})^{1/2}$], $(\overline{u_f^2})^{1/2}$ [$\equiv(\overline{u_{1f}^2})^{1/2}$], $(\overline{v_f^2})^{1/2}$ [$\equiv(\overline{u_{2f}^2})^{1/2}$] are given in table 5.1.

To estimate the values of the correlation $\overline{u_{ir}u_{if}}$ given from equations (5-4) and (5-5), the second derivatives of the temperature fluctuations were calculated by a simple three-point finite difference method with a time interval of 0.01s, and other quantities were approximated as $u_r \simeq u_a$, $v_r \simeq v_a$, $\alpha \simeq 0.0001K^{-1}$, $\Lambda \simeq \delta$, $2\psi = 4.4°$, and $\overline{U}_r \simeq 0.1$ m/s (see section 5.6). The estimated values of $(\overline{u_{ir}^2})^{1/2}$, $\overline{u_{ir}u_{if}}\big|_{max}$, C_1 and C_2 are also shown in table 5.1. They show that the correlation $\overline{u_{ir}u_{if}}$ can be neglected in comparison with other quantities. The ratio of $\overline{u_{if}^2}$ to $\overline{u_{ia}^2}$ is estimated to be 2.5 and 9.9% in the streamwise and vertical components for Ri=0.54, and 14.1 and 30.9% for Ri=1.45.

Figures 5.1(a)-(c) show the power spectra of the streamwise and vertical components, u and v, of the velocity fluctuations, and of the temperature fluctuations, θ, respectively, for Ri=0.54.

In figures 5.1(a) and 5.1(b) it is confirmed that the contribution of u_{if} to the apparent velocity is small enough in the low frequency range in which almost all the turbulence energy is distributed. The power spectrum of u_{if} has its maximum at a higher frequency than the characteristic frequency of an energy-containing turbulence eddy. This may be due to the fact that the fictitious velocity fluctuation, u_{if}, depends mainly on the second time-derivative of the temperature fluctuation. In fact, this is confirmed from the

Table 5.1. Turbulent intensities and correlations.

Quantities		Ri = 0.54	Ri = 1.45
$\overline{(u_a^2)}^{1/2}$	[m/s]	4.5×10^{-3}	4.0×10^{-3}
$\overline{(u_f^2)}^{1/2}$	[m/s]	7.1×10^{-4}	1.5×10^{-3}
C_1	[m K / s^3]	5.1×10^{-2}	7.8×10^{-2}
$\overline{u_r u_f}\Big\|_{max}$	[m^2/s^2]	9.2×10^{-8}	1.4×10^{-7}
$\overline{(u_r^2)}^{1/2}$	[m/s]	4.4×10^{-3}	3.5×10^{-3}
$\overline{(v_a^2)}^{1/2}$	[m/s]	2.8×10^{-3}	2.7×10^{-3}
$\overline{(v_f^2)}^{1/2}$	[m/s]	8.8×10^{-4}	1.5×10^{-3}
C_2	[m K /s^3]	6.6×10^{-2}	9.3×10^{-2}
$\overline{v_r v_f}\Big\|_{max}$	[m^2/s^2]	1.2×10^{-7}	1.7×10^{-7}
$\overline{(v_r^2)}^{1/2}$	[m/s]	2.6×10^{-3}	2.2×10^{-3}

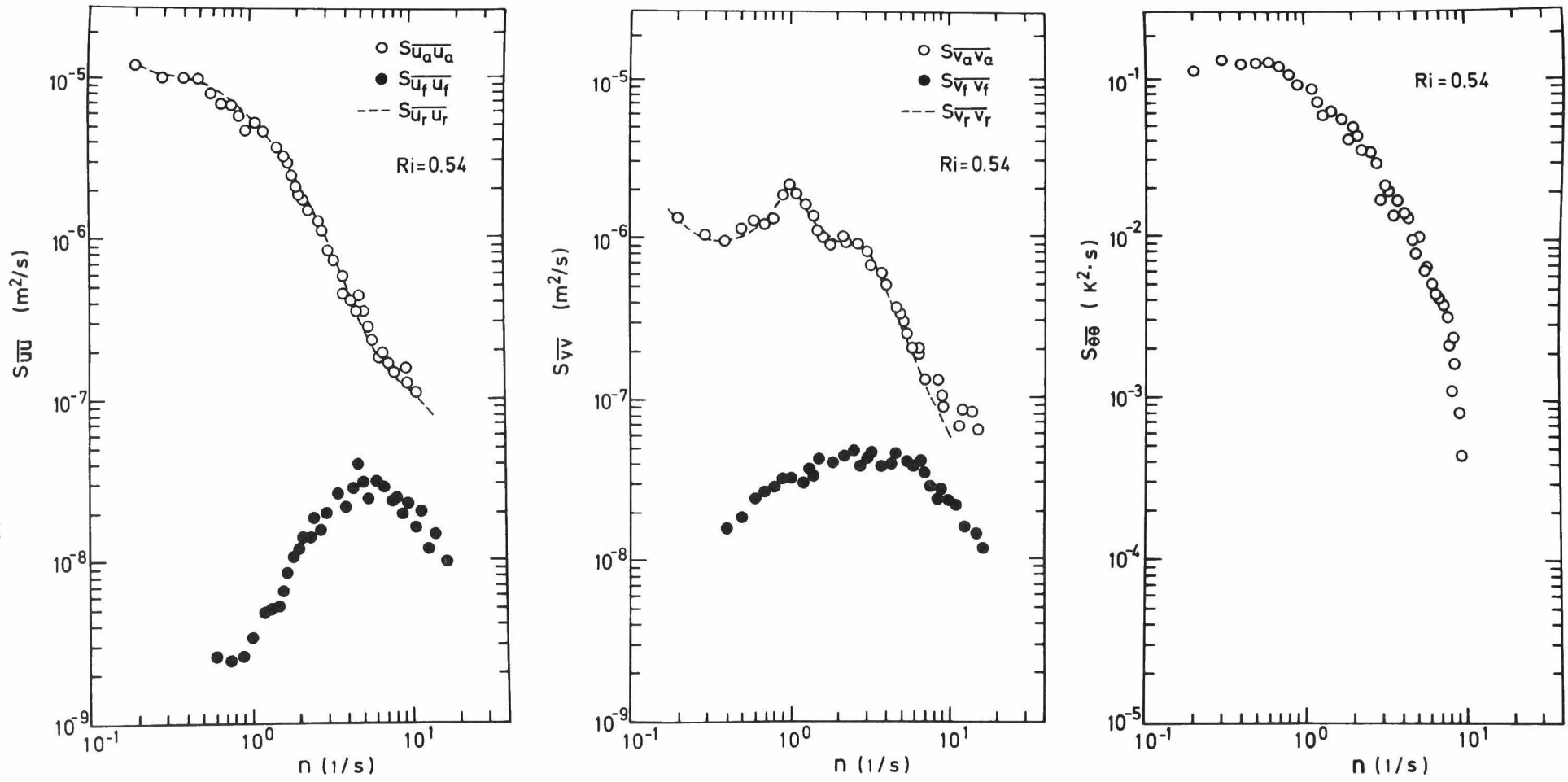

(a) (b) (c)

Figure 5.1. Power spectra obtained for Ri=0.54.

○ S_{aa} , ● S_{ff}, − − − S_{rr}

(a) streamwise velocity fluctuations

(b) vertical velocity fluctuations

(c) temperature fluctuations (○, $S_{\theta\theta}$)

experimental results of the power spectra of $\partial^2\theta/\partial^2 t$ shown in figure 5.2 (see section 5.6).

Figures 5.3(a) (c) show the power spectra obtained in more strongly stratified flow, i.e., Ri=1.45.

The contribution of the fictitious velocity u_{if} to the apparent velocity u_{ia} becomes larger and it may not be ignored even in the low frequency range. The power spectral functions S_{rf} or S_{fr} may be very small and as a result can be neglected, because the values of the correlations $\overline{u_{ir}u_{if}}$ are much smaller than those of $\overline{u_{ir}u_{ir}}$, as shown in table 5.1. These correlations are equal to the integrals of these spectra, S_{rf} and S_{rr}, with respect to the frequency from f=0 to ∞. Therefore, the power spectra of the apparent velocity can be corrected by using the fictitious velocity u_{if} and equation (5-3) to yield the spectra of the real turbulent velocity. Those are shown also in figures 5.1(a), 5.1(b), 5.3(a) and 5.3(b) as smoothed dashed curves. As the higher frequency range, the decaying trends are in good agreement with those of the spectra of temperature fluctuations in figures 5.1(c) and 5.3(c).

5.5 Accuracy of Measured Values

5.5.1 Limitation of frequency tracking

The maximum mean frequency and the maximum ratio of the turbulence intensity to mean velocity are 12100 Hz and 0.045, respectively. Most of the eddies have frequencies less than 10Hz , as shown in figures 5.1 and 5.3. The fraction of the signal drop-out time to the total time is less than 2.8%.

In these circumstances, the tracker(DISA 55L35) can operate

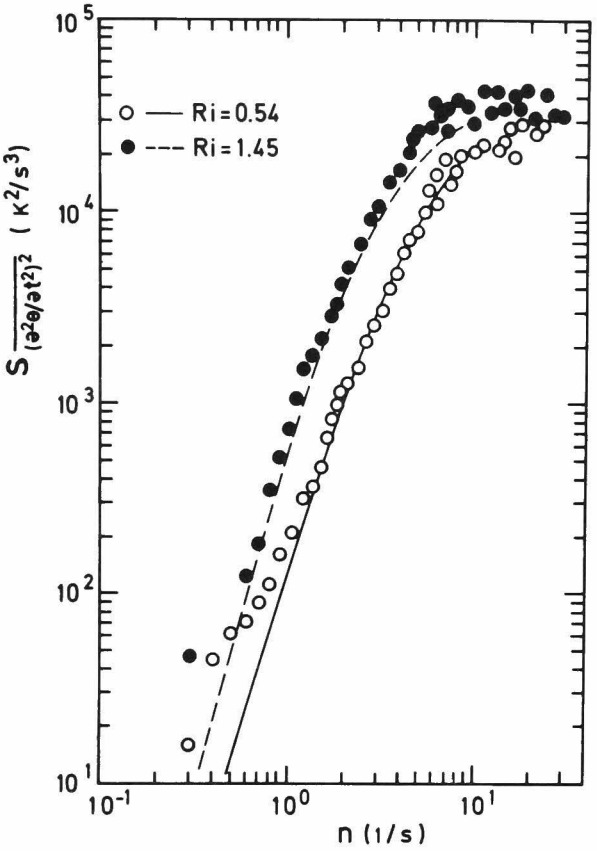

Figure 5.2. Power spectra of the second derivative of the temperature fluctuation.

Points calculated by a simple three point finite difference method

Lines by equation (5-12)

○ , ———:Ri=0.54; ● ,– – – :Ri=1.45.

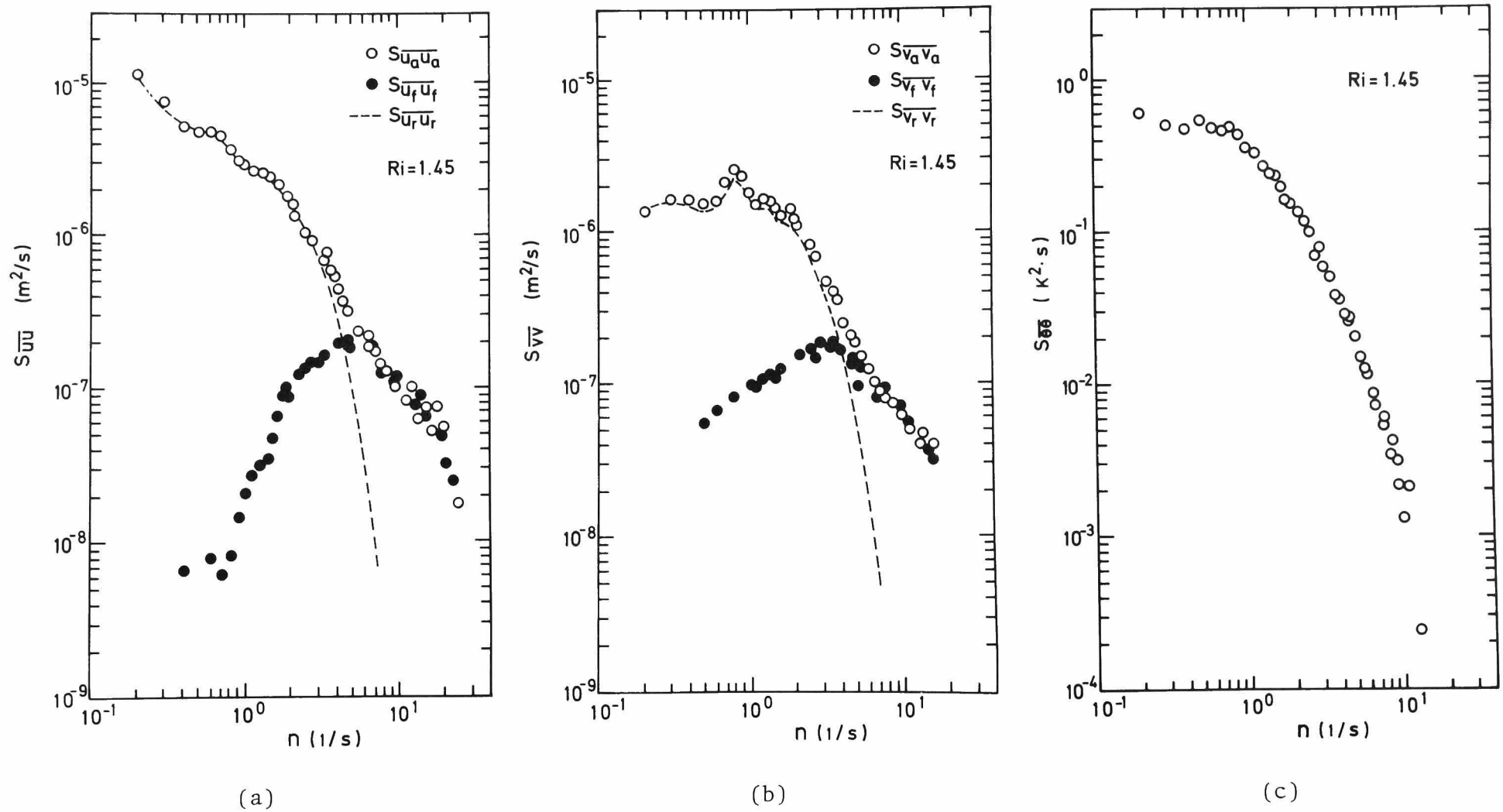

Figure 5.3. Power spectra obtained for Ri=1.45.

Symbols as in figure 5.1.

(a) streamwise velocity fluctuations (b) vertical velocity fluctuations (c) temperature fluctuations

satisfactorily. The error due to the drop-out was removed by neglecting the holding parts of tracker output voltage.

5.5.2 Evaluation of broadening effects

In the measurements of the low turbulence intensities in the present flow, a good estimate of the broadening effects is essential. A large number of investigators have dealt with this problem (see, for example, Durst et al.[57]).

The main sources of the broadening are the finite transit time of scattering particles crossing the measuring volume e_F, small scale turbulent fluctuations within the scattering volume e_T, gradients in mean velocity e_G and the instrumental bandwidth e_P (see Durst et al.[57]). In terms of velocity, the mean square broadening is

$$\overline{e^2}[m^2/s^2] = \overline{e_F^2} + \overline{e_T^2} + \overline{e_G^2} + \overline{e_P^2} + \overline{e_N^2}\ [m^2/s^2], \qquad (5\text{-}6)$$

where $\overline{e_N^2}$ is the mean square of the electric noise. Each term in equation (5-6) can be presented by one of the following theoretical equations:

$$\overline{e_F^2} = \frac{1}{4}\left(\frac{\lambda}{4\pi \sin\psi}\right)^2 \left(\frac{\overline{U_r^2}}{d_1^2} + \frac{\overline{u_{1r}^2}}{d_1^2} + \frac{\overline{u_{2r}^2}}{d_2^2} + \frac{\overline{u_{3r}^2}}{d_3^2}\right) \qquad (5\text{-}7)$$

(Edwards et al.[58]),where wave length λ and scattering volume dimensions d_1, d_2 and d_3 are 6.328×10^{-7}m, 3.72×10^{-4}m, 9.7×10^{-3}m and 3.72×10^{-4}m, respectively.

$$\overline{e_T^2} \simeq \frac{2}{15} d_2^2 \overline{U}_r^2 \frac{\varepsilon}{\nu} \quad , \qquad (5\text{-}8)$$

(George & Lumley[59]) where ε and ν are the ratio of dissipation and the kinematic viscosity.

$$\overline{e_G^2} = d_3^2 \left(\frac{d\bar{U}_r}{dy}\right)^2 \qquad (5\text{-}9)$$

and

$$\overline{e_P^2} = \left(\frac{\lambda \Delta f_0}{4(2\ \ln 2)^{1/2} \sin\psi}\right)^2 \quad , \qquad (5\text{-}10)$$

(Durst et al.[57]), where Δf_0 is the half-power bandwidth (120 Hz in the present measurements).

Accuracy of apparent velocity

The sum of the three mean square values was experimentally obtained from tracking signals in the isothermal laminar flow as

$$\overline{e_F^2} + \overline{e_P^2} + \overline{e_N^2} = 2.45 \times 10^{-7}\ m^2/s^2.$$

This is comparable to the calculated value

$$\overline{e_F^2} + \overline{e_P^2} = 2.10 \times 10^{-7} m^2/s^2.$$

Figure 5.4 shows that the spectrum of the noise measured in the laminar flow is similar to that of the white noise. From equations (5-8) and (5-9),

$$\overline{e_G^2} = 1.38 \times 10^{-7} m^2/s^2 \text{ for } d\bar{U}_r/dy = 1.0$$

and

$$\overline{e_T^2} = 4.19 \times 10^{-3} m^2/s^2 \text{ for } \varepsilon/\nu = 3.5,$$

where ε/ν is estimated from the result obtained by Nakagawa et al.[52]. The calculated value of $\overline{e_T^2}$ is questionable because of the excess over the mean square of the apparent velocity.

In order to estimate the tubulence broadening $\overline{e_T^2}$ experimentally, the spectra of the streamwise velocity in isothermal open channel

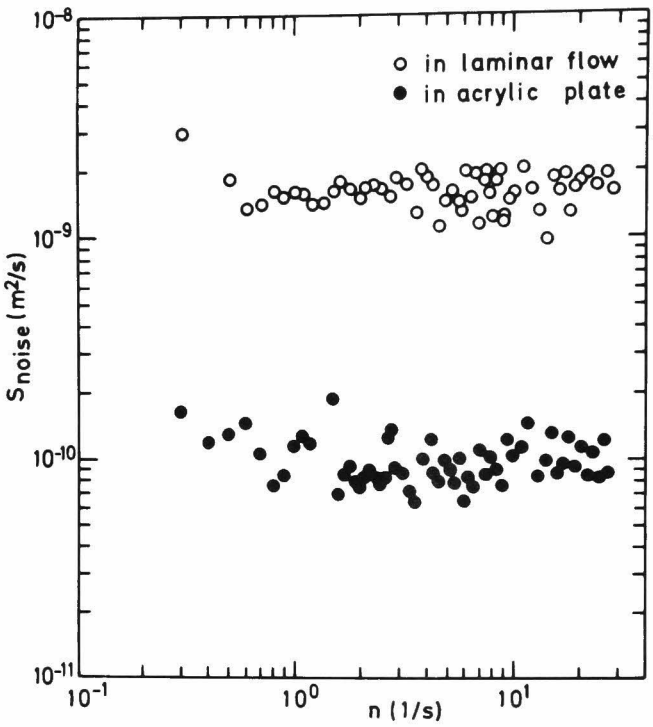

Figure 5.4. Noise spectra measured in laminar flow (O) and on acrylic plate (●).

flow with the Reynolds number very close to that in the present flow were measured at two different beam intersection angles, 4.4° and 9.0° . Figure 5.5 shows that in the case of the present intersection angle of 4.4° the turbulence broadening appears clearly in the frequency range larger than 7 Hz.

The turbulence broadening can then be approximately estimated from the equation

$$\overline{e_T^2} \simeq \overline{u^2} \int_0^7 S(f)df \quad , \tag{5-11}$$

where f is the frequency. The estimated value shows an error of 9% for the mean square velocity $2.56 \times 10^{5} m^2/s^2$.

When considering the same fraction of the turbulence broadening appropriate to the apparent velocities, the total mean square broadening $\overline{e^2}$ may be equal to $1.82 \times 10^{-6} m^2/s^2$ for $\overline{u_a^2}$ at Ri=1.45 and $9.01 \times 10^{7} m^2/s^2$ for $\overline{v_a^2}$ at Ri=1.45. These values show that the error is approximately 5.9% for $(\overline{u_a^2})^{1/2}$ at Ri = 1.45 and 6.4% for $(\overline{v_a^2})^{1/2}$ at Ri=1.45. The error is comparable to that due to the beam intersection effect. However, it should be noted that the error due to the beam intersection is independent of the broadening effects and can be corrected by the accurate measurement of the fictitious velocity with the present correction method.

Figure 5.6 shows the comparison between the turbulence intensities measured both with the L.D.V. used here and with a hot-film anemometer by Nakagawa et al.[52].

The good agreement between the two distributions supports the preceding estimation of the broadening error.

Accuracy of fictitious velocity

In the measurement of the fictitious velocity, $\overline{e_G^2}$ and $\overline{e_T^2}$ are

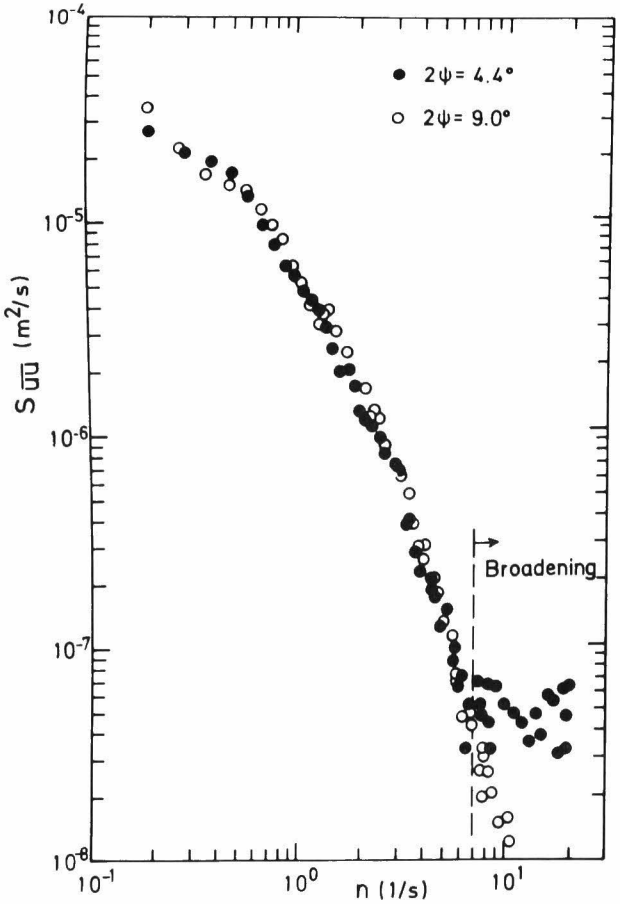

Figure 5.5. Spectra of streamwise velocity fluctuations measured at two different beam intersection angles.

● 4.4° ; ○ 9.0° , Re=10700

$u^* = 4.9 \times 10^{-3}$ m/s.

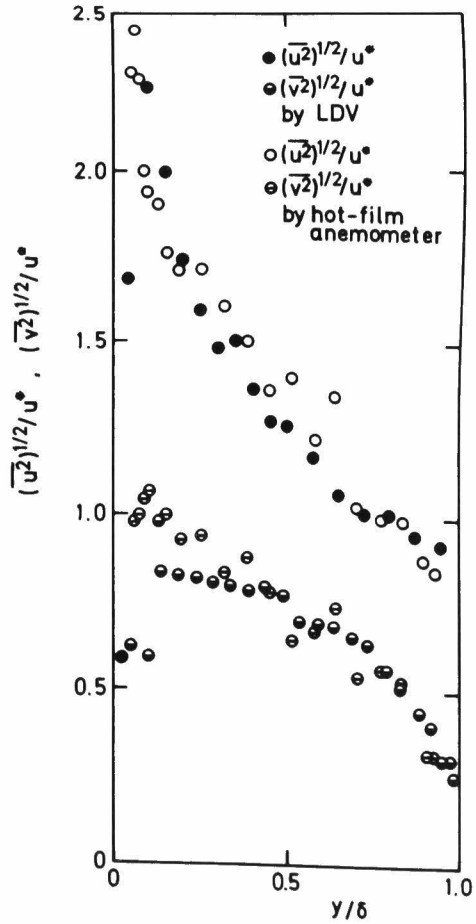

Figure 5.6. Comparison of turbulent intensities measured in isothermal open channel flows by L.D.V. (●, ⊖; Re=8600, $u^*=4.56 \times 10^{-3}$ m/s), and by a hot-film anemometer (○, ⊖; Re=33300, $u^*=8.1 \times 10^{-3}$ m/s; Nakagawa et al. [52]).

Measurements show $(\overline{u^2})^{1/2}/u^*$ (● and ○) and $(\overline{v^2})^{1/2}/u^*$ (⊖ and ⊖).

equal to zero because of the stationary scattering particles in the acrylic plate. From equation(5-7), we have negligible mean square value of transit time broadening

$$\overline{e_F^2} \leq 4.71 \times 10^{12}\ m^2/s^2$$

in the measurement of u_f at Ri=0.54.

In order to estimate $\overline{e_P^2} + \overline{e_N^2}$ experimentally, the noise signal was measured with the acrylic plate held in an isothermal flow. The noise spectrum is also shown in figure 5.4. The mean square value, $\overline{e_P^2} + \overline{e_N^2}$, was $2.44 \times 10^{-8} m^2/s^2$. Then, the total mean square broadening $\overline{e^2}$ is approximately equal to $2.44 \times 10^{-8} m^2/s^2$. The error is 2.5% for $(\overline{u_f^2})^{1/2}$ at Ri=0.54 and 1.6% for $(\overline{v_f^2})^{1/2}$ at Ri=0.54, respectively.

The very accurate measurements of the fictitious velocities support the significance of the correction method of the beam intersection effect.

5.5.3 Accuracy of second derivatives of temperature fluctuations

In figure 5.2, the measured spectra $S_{\ddot{\theta}\ddot{\theta}}(f)$ of $\partial^2\theta/\partial t^2$ based on the finite difference method are compared with those calculated from the following relation,

$$S_{\ddot{\theta}\ddot{\theta}}(f) = 16\,\pi^4 f^4\, S_{\theta\theta}(f)\ , \qquad (5\text{-}12)$$

where $S_{\theta\theta}$ is shown in figures 5.1(c) and 5.3(c).

The calculated spectra are shown by solid and dashed curves for Ri=0.54 and 1.45,respectively. For Ri=1.45, the r.m.s. values of $\partial^2\theta/\partial t^2$ obtained from the integration of the measured and calculated spectra for frequencies less than 10 Hz are 405 and 451K, respectively. These two values agree within an accuracy of 10%.

5.6 Theoretical Derivation of Correlation between Real Velocity and Fictitious Velocity

When light passes through non-isothermal turbulent flow, the effect on the Doppler frequency shift of the variation of refractive index with position and time must be taken into account. The time scale of the variation of refractive index is much larger than the time required for light to travel from the source to the particles in the flow, which enables us to apply the usual equation for the Doppler effect on the light and to use the theory of geometrical optics to describe the light path. The Doppler frequency υ is, therefore, given by the following equation:

$$\upsilon \approx \upsilon_0\left[1-\frac{1}{c}\frac{\mathrm{d}}{\mathrm{d}t}\int_{l_0(t)}^{l_1(t)} n(s,t)\,\mathrm{d}s\right]=\upsilon_0\left[1-\frac{1}{c}\frac{\mathrm{d}l_1}{\mathrm{d}t}n(l_1,t)+\frac{1}{c}\frac{\mathrm{d}l_0}{\mathrm{d}t}n(l_0,t)-\frac{1}{c}\int_{l_0}^{l_1}\frac{\partial n}{\partial t}\mathrm{d}s\right], \qquad (5\text{-}13)$$

where c is the velocity of light, n the refractive index, and ℓ_0 and ℓ_1 denote the position of the light source and the receiver, respectively. In equation(5-13), the term

$$\frac{\mathrm{d}}{\mathrm{d}t}\int_{l_0}^{l_1} n(s,t)\,\mathrm{d}s$$

denotes the relative velocity between the light source and the receiver, and the time-derivatives, $\mathrm{d}\ell_0/\mathrm{d}t$ and $\mathrm{d}\ell_1/\mathrm{d}t$, are the velocity components in the direction of the light path at the source and the receiver, respectively. In the present case $\mathrm{d}\ell_0/\mathrm{d}t=0$ and $\mathrm{d}\ell_1/\mathrm{d}t=(\mathbf{u}_r\cdot\boldsymbol{\tau})$, where $\boldsymbol{\tau}$ is the tangential unit vector of the beam and $\mathbf{u}_r$ is the real velocity vector.

Consider the two-beam system shown in figure 5.7 for the measurement of the streamwise velocity component.

The Doppler frequency at the measuring point is calculated by using equation(5-13) as

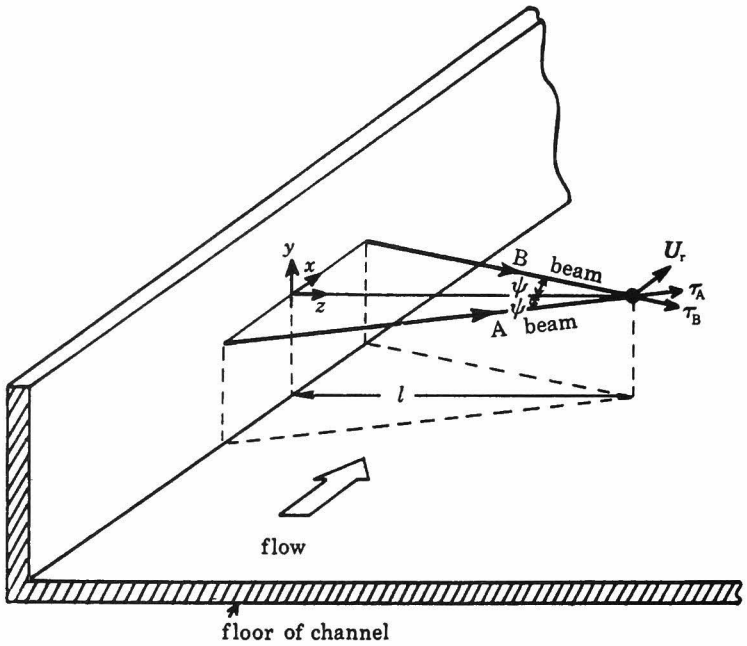

Figure 5.7. Two-beam system for streamwise velocity measurement.

$$\Delta U \approx \frac{n U_0}{c}\left\{(\boldsymbol{u}_r\cdot\boldsymbol{\tau}_A)-(\boldsymbol{u}_r\cdot\boldsymbol{\tau}_B)+\frac{1}{n}\int_{l_0}^{l_A}\frac{\partial n_A}{\partial t}\,ds-\frac{1}{n}\int_{l_0}^{l_B}\frac{\partial n_B}{\partial t}\,ds\right\}, \tag{5-14}$$

where $n=n_A(\ell_A,t)=n_B(\ell_B,t)$.

In order to calculate the terms in equation (5-14), we apply Fermat's principle (Rossi[60]), written as

$$\operatorname{grad} n = \mathrm{d}(n\tau)/\mathrm{d}s. \tag{5-15}$$

On converting the independent variable from s to z, we obtain

$$n\left[(1+F_2^2)\frac{dF_1}{dz}-F_1F_2\frac{dF_2}{dz}\right]-(1+F_1^2+F_2^2)(1+F_2^2)\frac{\partial n}{\partial f_1}+(1+F_1^2+F_2^2)F_1F_2\frac{\partial n}{\partial f_2}$$
$$+(1+F_1^2+F_2^2)F_1\frac{\partial n}{\partial f_3}=0, \tag{5-16}$$

and

$$n\left[(1+F_1^2)\frac{dF_2}{dz}-F_2F_1\frac{dF_1}{dz}\right]+(1+F_1^2+F_2^2)F_1F_2\frac{\partial n}{\partial f_1}-(1+F_1^2+F_2^2)(1+F_1^2)\frac{\partial n}{\partial f_2}$$
$$+(1+F_1^2+F_2^2)F_2\frac{\partial n}{\partial f_3}=0, \tag{5-17}$$

where $F_1=df_1/dz$ and $F_2=df_2/dz$, and $f_1(z)$ and $f_2(z)$ denote the x and y coordinates of the light beam. The instantaneous displacements f_1 and f_2 can be written as

$$f_1=\bar{f}_1+f_1'=(z-l)\tan\psi+f_1'=a(z-l)+f_1', \tag{5-18}$$
$$f_2=\bar{f}_2+f_2', \tag{5-19}$$
$$n=\bar{n}+n'. \tag{5-20}$$

Here, $\bar{n}$ is a function of $\bar{f}_2$ only, because the mean temperature gradient exists only in the y direction.

If the refractive index and its space derivatives are expanded into Taylor series around the point $(\bar{f}_1,\bar{f}_2)$ and the higher order terms are neglected, we obtain

$$\frac{\partial n}{\partial f_1} \approx \left.\frac{\partial n'}{\partial x}\right|_{\bar{f}_1, \bar{f}_2}, \tag{5-21}$$

$$\frac{\partial n}{\partial f_2} \approx \frac{d\bar{n}}{d\bar{f}_2} + \left.\frac{\partial n'}{\partial y}\right|_{\bar{f}_1, \bar{f}_2}, \tag{5-22}$$

and

$$\frac{\partial n}{\partial f_3} \approx \left.\frac{\partial n'}{\partial z}\right|_{\bar{f}_1, \bar{f}_2}. \tag{5-23}$$

Substituting equations (5-21)-(5-23) in equations(5-16) and (5-17), we obtain equations for the averaged and the fluctuating components as follows:

$$\frac{d\bar{n}}{d\bar{f}_2}(1+a^2+\bar{F}_2^2) = \bar{n}\frac{d\bar{F}_2}{dz}, \tag{5-24}$$

$$\begin{aligned}
&\frac{d\bar{n}}{d\bar{f}_2}[\bar{F}_2(1+a^2+\bar{F}_2^2)+2a^2F_1'\bar{F}_2+a\bar{F}_2(1+a^2+\bar{F}_2^2)+aF_2'(1+a^2+\bar{F}_2^2)+2aF_2'\bar{F}_2^2] \\
&\quad -\frac{d\bar{F}_2}{dz}[\bar{n}(\bar{F}_2+a\bar{F}_2+a)-a\bar{F}_2 n'] - \frac{dF_2'}{dz}a\bar{n}\bar{F}_2 + \frac{dF_1'}{dz}\bar{n}(1+\bar{F}_2^2) \\
&\quad -\left.\frac{\partial n'}{\partial x}\right|_{\bar{f}_1, \bar{f}_2}(1+\bar{F}_2^2)(1+a^2+\bar{F}_2^2) \\
&\quad +\left.\frac{\partial n'}{\partial y}\right|_{\bar{f}_1, \bar{f}_2}a\bar{F}_2(1+a^2+\bar{F}_2^2) + \left.\frac{\partial n'}{\partial z}\right|_{\bar{f}_1, \bar{f}_2}a(1+a^2+\bar{F}_2^2) = 0,
\end{aligned} \tag{5-25}$$

and

$$\begin{aligned}
&-\frac{d\bar{n}}{d\bar{f}_2}[(1+a^2+\bar{F}_2^2)(2aF_1'+1+a^2)+2(1+a^2)(\bar{F}_2F_2'+aF_1')] \\
&+\frac{d\bar{F}_2}{dz}[2a\bar{n}F_1'+(1+a^2)(\bar{n}+n')] + \frac{dF_2'}{dz}\bar{n}(1+a^2) - \frac{dF_1'}{dz}a\bar{n}\bar{F}_2 \\
&+\left.\frac{\partial n'}{\partial x}\right|_{\bar{f}_1, \bar{f}_2}a\bar{F}_2(1+a^2+\bar{F}_2^2) - \left.\frac{\partial n'}{\partial y}\right|_{\bar{f}_1, \bar{f}_2}(1+a^2)(1+a^2+\bar{F}_2^2) \\
&+\left.\frac{\partial n'}{\partial z}\right|_{\bar{f}_1, \bar{f}_2}\bar{F}_2(1+a^2+\bar{F}_2^2) = 0.
\end{aligned} \tag{5-26}$$

The equation(5-24) for the averaged quantities is the basic equation for the Schlieren method and can be solved under the following boundary conditions:

$$\bar{f}_2 = 0, \quad \mathrm{d}\bar{f}_2/\mathrm{d}z = \bar{F}_2 = 0, \quad n = n_0 \quad \text{at} \quad z = 0, \tag{5-27}$$

and the approximation

$$\bar{n}^2 \simeq n_0^2 + 2n_0(\mathrm{d}\bar{n}/\mathrm{d}\bar{f}_2)_{z=0}. \tag{5-28}$$

The solution of equation(5-24) is given as

$$\bar{f}_2 = \frac{(1+a^2)}{2n_0}\left.\frac{\mathrm{d}\bar{n}}{\mathrm{d}\bar{f}_2}\right|_{z=0} z^2, \tag{5-29}$$

$$\bar{F}_2 = \frac{(1+a^2)}{n_0}\left.\frac{\mathrm{d}\bar{n}}{\mathrm{d}\bar{f}_2}\right|_{z=0} z, \tag{5-30}$$

and

$$\frac{\mathrm{d}\bar{F}_2}{\mathrm{d}z} = \frac{(1+a^2)}{n_0}\left.\frac{\mathrm{d}\bar{n}}{\mathrm{d}\bar{f}_2}\right|_{z=0}. \tag{5-31}$$

In the case of $(\mathrm{d}\bar{n}/\mathrm{d}\bar{f}_2)_{z=0}/n_0 \ll 1$, the expressions for equations (5-28), (5-30) and (5-31) reduce to

$$\bar{n} \approx n_0, \quad \bar{F}_2 \ll 1 \quad \text{and} \quad \mathrm{d}\bar{F}_2/\mathrm{d}z \ll 1.$$

Introduction of these approximations into equations(5-25) and (5-26) yields

$$n_0\frac{\mathrm{d}^2 f_1'}{\mathrm{d}z^2} = (1+a^2)\left.\frac{\partial n'}{\partial x}\right|_{\bar{f}_1,\bar{f}_2} - a(1+a^2)\left.\frac{\partial n'}{\partial z}\right|_{\bar{f}_1,\bar{f}_2}, \tag{5-32}$$

and

$$n_0\frac{\mathrm{d}^2 f_2'}{\mathrm{d}z^2} = (1+a^2)\left.\frac{\partial n'}{\partial y}\right|_{\bar{f}_1,\bar{f}_2}. \tag{5-33}$$

Now, we can calculate each term in equation(5-14) as:

$$\frac{1}{n}\int_0^l \frac{\partial n}{\partial t}\,ds \approx \frac{1}{n_0}(1+a^2)^{\frac{1}{2}}\int_0^l \frac{\partial n}{\partial t}\bigg|_{\bar{f}_1,\bar{f}_2} dz + \frac{a}{(1+a^2)^{\frac{1}{2}}}\left[\frac{\partial f_1'}{\partial t}\bigg|_{z=l} - \frac{\partial f_1'}{\partial t}\bigg|_{z=0}\right], \tag{5-34}$$

and

$$(u_r\cdot\tau) \approx \frac{a}{(1+a^2)^{\frac{1}{2}}}(\overline{U}_r+u_r) - \frac{a^2\overline{U}_r}{(1+a^2)^{\frac{1}{2}}}\frac{df_1'}{dz}\bigg|_{z=l} + \frac{w_r}{(1+a^2)^{\frac{1}{2}}}, \tag{5-35}$$

where w_r is the real fluctuating velocity in the z direction(see figure 5.7).

The apparent velocity U_a measured by L.D.V. is determined by the equation

$$U_a = c\Delta\upsilon/2\upsilon_0 n\sin\psi. \tag{5-36}$$

With equations(5-14), (5-34) and (5-35), equation(5-36) may be rewritten as

$$U_a|_{z=l} = \frac{1+a^2}{2an_0}\left[\int_0^l\left(\frac{\partial n_B'}{\partial t}-\frac{\partial n_A'}{\partial t}\right)dz\right] - \frac{1}{2}\left[\frac{\partial f_{1A}'}{\partial t}\bigg|_{z=l} + \frac{\partial f_{1B}'}{\partial t}\bigg|_{z=l} - \frac{\partial f_{1A}'}{\partial t}\bigg|_{z=0} - \frac{\partial f_{1B}'}{\partial t}\bigg|_{z=0}\right] + (\overline{U}_r+u_r) + \frac{a\overline{U}_r}{2(1+a^2)}\left[\frac{df_{1B}'}{dz}\bigg|_{z=l} - \frac{df_{1A}'}{dz}\bigg|_{z=l}\right]. \tag{5-37}$$

Since $U_a = \overline{U}_r + u_r + u_f$, the velocity u_f is given as follows:

$$u_f|_{z=l} = \frac{(1+a^2)}{2an_0}\left[\int_0^l\left(\frac{\partial n_B'}{\partial t}-\frac{\partial n_A'}{\partial t}\right)dz\right] - \frac{1}{2}\left[\frac{\partial f_{1A}'}{\partial t}\bigg|_{z=l} + \frac{\partial f_{1B}'}{\partial t}\bigg|_{z=l} - \frac{\partial f_{1A}'}{\partial t}\bigg|_{z=0} - \frac{\partial f_{1B}'}{\partial t}\bigg|_{z=0}\right] + \frac{a\overline{U}_r}{2(1+a^2)}\left[\frac{df_{1B}'}{dz} - \frac{df_{1A}'}{dz}\right]_{z=l}. \tag{5-38}$$

Therefore, the correlation $\overline{u_r u_f}$ is given as

$$\overline{u_r u_f}|_{z=l} = \frac{1+a^2}{2an_0}\left[\int_0^l\left(\overline{u_r|_{z=l}\frac{\partial n_B'}{\partial t}} - \overline{u_r|_{z=l}\frac{\partial n_A'}{\partial t}}\right)dz\right] - \frac{1}{2}\left[\overline{u_r|_{z=l}\frac{\partial f_{1A}'}{\partial t}\bigg|_{z=l}} + \overline{u_r|_{z=l}\frac{\partial f_{1B}'}{\partial t}\bigg|_{z=l}}\right] - \frac{1}{2}\left[\overline{u_r|_{z=l}\frac{\partial f_{1A}'}{\partial t}\bigg|_{z=0}} + \overline{u_r|_{z=l}\frac{\partial f_{1B}'}{\partial t}\bigg|_{z=0}}\right] + \frac{a}{2(1+a^2)}\overline{U}_r\left[\overline{u_r|_{z=l}\frac{df_{1B}'}{dz}\bigg|_{z=l}} - \overline{u_r|_{z=l}\frac{df_{1A}'}{dz}\bigg|_{z=l}}\right]. \tag{5-39}$$

The first and fourth terms can be neglected because

$$\overline{u_r|_{z=l}\frac{\partial n'_B}{\partial t}} \approx \overline{u_r|_{z=l}\frac{\partial n'_A}{\partial t}}, \tag{5-40}$$

and

$$\overline{u_r|_{z=l}\left.\frac{df'_{1B}}{dz}\right|_{z=l}} \approx \overline{u_r|_{z=l}\left.\frac{df'_{1A}}{dz}\right|_{z=l}}. \tag{5-41}$$

The validity of equation(5-40) can be easily understood, since the scale of energy-containing turbulence eddy in the present flow is larger than the distance between the two beams. In addition, the third term in equation(5-39) can be also neglected because of the very small correlation between u_r at $z=\ell$ and $\partial f'_1/\partial t$ at $z=0$. Therefore, by using equation(5-32), we obtain

$$\begin{aligned}\overline{u_r u_f}|_{z=l} = &-\frac{a^2+1}{2n_0}\left[\overline{u_r|_{z=l}\int_0^l dz\int_0^z \left.\frac{\partial^2 n'_A}{\partial x\,\partial t}\right|_{\bar{f}_1,\bar{f}_2} dz'} + \overline{u_r|_{z=l}\int_0^l dz\int_0^z \left.\frac{\partial^2 n'_B}{\partial x\,\partial t}\right|_{\bar{f}_1,\bar{f}_2} dz'}\right] \\ &+\frac{a(a^2+1)}{2n_0}\left[\overline{u_r|_{z=l}\int_0^l dz\int_0^z \left.\frac{\partial^2 n'_A}{\partial z'\,\partial t}\right|_{\bar{f}_1,\bar{f}_2} dz'} + \overline{u_r|_{z=l}\int_0^l dz\int_0^z \left.\frac{\partial^2 n'_B}{\partial z'\,\partial t}\right|_{\bar{f}_1,\bar{f}_2} dz'}\right].\end{aligned} \tag{5-42}$$

Since $a \simeq 0.04$ in this study, we can neglect the second term on the right hand side of equation(5-42). When we further introduce Taylor's hypothesis of frozen turbulence $\frac{\partial}{\partial t} = -\bar{U}_r\frac{\partial}{\partial x}$, then we obtain

$$\overline{u_r u_f}|_{\zeta=0} = \frac{a^2+1}{2n_0\bar{U}_r}\left[\int_0^\infty \overline{\zeta u_r|_{\zeta=0}\frac{\partial^2 n'_A}{\partial t^2}}\,d\zeta + \int_0^\infty \overline{\zeta u_r|_{\zeta=0}\frac{\partial^2 n'_B}{\partial t^2}}\,d\zeta\right] \approx \frac{a^2+1}{n_0\bar{U}_r}\left[\int_0^\infty \overline{\zeta u_r|_{\zeta=0}\frac{\partial^2 n'}{\partial t^2}}\,d\zeta\right], \tag{5-43}$$

where $\zeta = \ell - z$.

The fluctuation n' of the refractive index can be related to the temperature fluctuation θ by the equation

$$n' = \alpha\theta\ , \tag{5-44}$$

where α is the temperature dependence of the refractive index.

Substitution of equation (5-44) in equation (5-43) yields

$$\overline{u_r u_f}|_{\zeta=0} = \frac{\alpha}{n_0 \bar{U}_r \cos^2\psi} \int_0^\infty \zeta \overline{u_r|_{\zeta=0} \frac{\partial^2\theta}{\partial t^2}} \, d\zeta. \tag{5-45}$$

Assuming that

$$\left| \overline{u_r|_{\zeta=0} \frac{\partial^2\theta}{\partial t^2}} \right| \approx \left| \overline{u_a|_{\zeta=0} \frac{\partial^2\theta}{\partial t^2}} - \overline{u_f|_{\zeta=0} \frac{\partial^2\theta}{\partial t^2}} \right| \leqslant 1.5 C_1 \exp(-\zeta/\Lambda), \tag{5-46}$$

we finally obtain

$$\overline{u_r u_f} \leqslant \frac{\alpha \Lambda^2 C_1}{n_0 \bar{U}_r \cos^2\psi}, \tag{5-47}$$

where Λ is an integral scale of turbulence, and

$$C_1 = |\overline{u_a|_{\zeta=0} \partial^2\theta/\partial t^2|_{\zeta=0}}|.$$

Similarly we obtain

$$\overline{v_r v_f}|_{\zeta=0} = \frac{\alpha(\overline{u_r^2}|_{\zeta=0})^{\frac{1}{2}}}{n_0 \bar{U}_r (\overline{v_r^2}|_{\zeta=0})^{\frac{1}{2}} \cos^2\psi} \int_0^\infty \zeta \overline{v_r|_{\zeta=0} \frac{\partial^2\theta}{\partial t^2}} \, d\zeta \leqslant \frac{\alpha C_2 \Lambda^2 (\overline{u_r^2}|_{\zeta=0})^{\frac{1}{2}}}{n_0 \bar{U}_r (\overline{v_r^2}|_{\zeta=0})^{\frac{1}{2}} \cos^2\psi}, \tag{5-48}$$

where the assumptions

$$\frac{\partial n'}{\partial y} \approx \frac{\partial n'}{\partial x} \frac{(\overline{u_r^2}|_{\zeta=0})^{\frac{1}{2}}}{(\overline{v_r^2}|_{\zeta=0})^{\frac{1}{2}}} \approx \frac{(\overline{u_r^2}|_{\zeta=0})^{\frac{1}{2}}}{\bar{U}_r (\overline{v_r^2}|_{\zeta=0})^{\frac{1}{2}}} \frac{\partial n'}{\partial t}, \tag{5-49}$$

and

$$\left| \overline{v_r|_{\zeta=0} \frac{\partial^2\theta}{\partial t^2}} \right| \approx \left| \overline{u_a|_{\zeta=0} \frac{\partial^2\theta}{\partial t^2}} - \overline{u_f|_{\zeta=0} \frac{\partial^2\theta}{\partial t^2}} \right| \leqslant 1.5 C_2 \exp(-\zeta/\Lambda) \tag{5-50}$$

are used. In equation (5-50),

$$C_2 = |\overline{v_a|_{\zeta=0} \partial^2\theta/\partial t^2|_{\zeta=0}}|.$$

The assumptions in equations(5-46) and (5-50) can be estimated experimentally. Figure 5.8 shows the values of $\overline{u_r|_{\zeta=0} \partial^2\theta/\partial t^2}/C_1$ and $\overline{v_r|_{\zeta=0} \partial^2\theta/\partial t^2}/C_2$ against ζ/Λ. The results support the validity of equations(5-46) and (5-50).

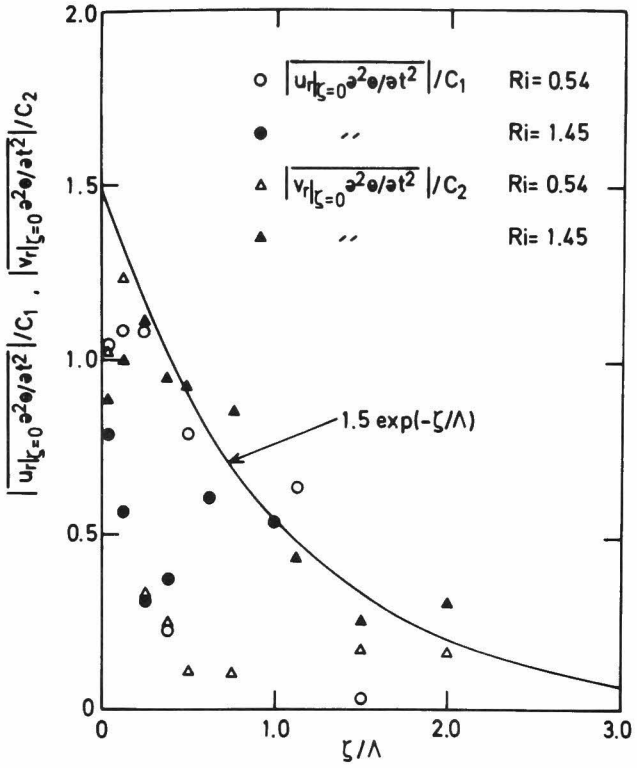

Figure 5.8. Lateral distributions of the correlation between real velocity and the second derivative of temperature fluctuations, at Ri=0.54(open symbols) and Ri=1.45 (solid symbols).

Measurements show $\overline{|u_r|_{\zeta=0}\,\partial^2\theta/\partial t^2|}/C_1$ (circles) and $\overline{|v_r|_{\zeta=0}\,\partial^2\theta/\partial t^2|}/C_2$ (triangles). The curve represents the function $1.5\cdot\exp(-\zeta/\Lambda)$.

5.7 Conclusion

The interaction effect of the laser beams with the temperature fluctuations along the beam paths cannot be neglected even in non-isothermal water flows with comparatively small temperature fluctuations, when applying laser Doppler velocimetry to turbulence measurement in non-isothermal flows. The interaction effect becomes predominant at a frequency range higher than the characteristic frequency of energy-containing turbulence eddies. Also, it is confirmed, by using an approximated optical analysis and measurements of temperature and velocity fluctuations, that the correlation between the real velocity and the fictitious velocity due to the interaction effect is negligible in comparison with the auto-correlation of the real velocity.

In the present study the correction method was applied only to a stratified water flow. However, the method might be applicable to the prediction of the interaction effect in other non-isothermal flows if a small acrylic plate(or in the case of high temperature flows, a glass plate with scattering particles) could be held at the point of intersection of the two beams. In the future, the appearance of more practical correction methods is expected.

CHAPTER 6 CONCLUSION

6.1 Summary and Conclusion

Buoyancy effects on the turbulence structure in both stably and unstably stratified flow were investigated experimentally by means of flow visualization technique and various statistical analyses of turbulent signals. In addition, the spectral equation model was applied to the stratified flows in order to account for the variations of turbulent quantities with the local gradient Richardson number, and measuring technique by a laser Doppler velocimetry in non-isothermal flow with the turbulent temperature fluctuations was developed and applied to the stratified flows.

The main results from this study can be summalized as follows.

1. Distributions of turbulence quantities in both stably and unstably stratified flows are strongly affected by buoyancy and their variations with the bulk Richardson number can be interpreted by investigating the production terms by shear and buoyancy in the respective transport equations.

2. In stably stratified flow the buoyancy works so as to organize the turbulent motion into a wavelike motion. In this case, transport of momentum and heat is reduced. In strongly stable flow the fluid motion is dominated by the wavelike motion, and transport of momentum and heat against the temperature and velocity gradients occurs by the buoyancy-driven force, only at the instant of wave breakdown.

In unstably stratified flow, the buoyancy works so as to enhance the turbulent motion. The predominant buoyancy-driven motion

consists of the downward movement of cold eddy and the upward movement of hot eddy, and in particular the intermittent downward movement of cold eddy mainly causes the vertical transport of heat.

3. The local gradient Richardson number,Ri,is the predominant parameter for representing the buoyancy effects on the turbulence, and the correlations of the turbulence quantities become universal.

4. The spectral equation model is an advanced theoretical model and can explain qualitatively the variations of the measured turbulence quantities with the local gradient Richardson number.

5. When a laser Doppler velocimetry is applied to turbulence measurement in non-isothermal flow, the interaction effect of the laser beams cannot be neglected even in non-isothermal flows with comparatively small temperature fluctuations. To correct and estimate the interaction effect, an experimental method is presented and attains a success on the turbulence measurements in stratified flows.

6.2 Suggestions for Future Work

The progress of this study recommends the following future works;

1. It has been shown that wave breakdown by shear instability causes the turbulent transport in strongly stable flow. Further investigations could help to clarify the mechanism of the wave breakdown.

2. The practical mathematical models based on the present experimental

results could be devised to simulate the development of the stratified flows in the environment; the atmospheric boundary layer, the ocean and the river.

3. The diffusion of the pollutants in stratified flows is an important subject in the environmental problems. Experimental studies of the lateral diffusion of mass in the present flows could give a guide for air or water pollution control.

REFERENCES

[1] Charnock,H. 1967 Quart.J.Roy.Met.Soc. 93,97.

[2] Businger,J.A.,Wyngaard,J.C.,Izumi,Y. & Bradley,E.F. 1971 J.Atmos.Sci. 28,181.

[3] Haugen,D.A.,Kaimal,J.C. & Bradley,E.F. 1971 Quart.J.Roy. Met.Soc. 97,168.

[4] Wyngaard,J.C. & Coté,O.R. 1971 J.Atmos.Sci. 28,190.

[5] Wyngaard,J.C.,Coté,O.R. & Izumi,Y. 1971 J.Atmos.Sci. 28,1171.

[6] McBean,G.A. & Miyake,M. 1972 Quart.J.Roy.Met.Soc. 98,383.

[7] Pruitt,W.O.,Morgan,D.L. & Lourence,F.J. 1973 Quart.J.Roy. Met.Soc. 99,370.

[8] Webster,C.A.G. 1964 J.Fluid Mech. 19,221.

[9] Arya,S.P.S. & Plate,E.J. 1969 J.Atmos.Sci. 26,656.

[10] Arya,S.P.S. 1975 J.Fluid Mech. 68,321.

[11] Ellison,T.H. & Turner,J.S. 1960 J.Fluid Mech. 8,514.

[12] Schiller,E.J. & Sayre,W.W. 1975 J.ASCE HY6,749.

[13] Strele,J.G. & Sayre,W.W. 1976 Proc. Int.Seminar on Turbulent Buoyant Convection,Dubrovnik, Yugoslavia.

[14] Deardorff,J.W. 1973 Workshop on Micrometeorology, American Meteorological Society.

[15] Launder,B.E. 1975 J.Fluid Mech. 67,569.

[16] Gibson,M.M. & Launder,B.E., 1978 J.Fluid Mech. 86,491.

[17] Pao,Yih-Ho, 1969 Radio Sci. 4,1315.

[18] Stewart,R.W. 1969 Radio Sci. 4,1269.

[19] Long,R.R. 1970 J.Fluid Mech. 42,349.

[20] Turner,J.S. 1973 Buoyancy Effects in Fluids, Cambridge University Press.

[21] Durst,F. & Whitelaw,J.H. 1971 DISA Inf. 12,11.

[22] Bendat,J.S. & Piersol,A.G. 1971 Random data: Analysis and

Measurement Procedures. New York: Wiley-Interscience.

[23] Clauser,F.H. 1954 J.Aero.Sci. 21,91.

[24] Gibson,M.M. 1962 Nature. Lond. 195, 1281.

[25] Ueda,H. & Mizushina,T. 1977 5th Biennial Sym. on Turbulence, Univ. of Missouri-Rolla, Missouri.

[26] Batchelor,G.K. & Townsend,A.A. 1949 Proc.Roy.Soc.London A,199,238... A,199,238.

[27] Linden,P.F. 1974 Advance in Geophysics 18,433.

[28] Willis,G.E. & Deardorff,J.W. 1974 J.Atmos.Sci. 31, 1297.

[29] La Fond,E.C. 1966 Encyclopedia of Oceanography, New York: Reinhold,402.

[30] Bretherton,E.P. 1969 Radio Sci. 4,1297.

[31] Deardorff,J.W.,Willis,G.E. & Lilly,D.K. 1969 J.Fluid Mech. 35,7.

[32] Zeman,O. & Lumley,J.L. 1976 J.Atmos.Sci. 33,1974.

[33] Lenschow,D.H. 1970 J.Appl.Met. 9,874.

[34] Ueda,H., Mitsumoto,S., Komori,S. & Mizushina,T. 1979 (submitted to Proc. Roy. Met. Soc.)

[35] Malkus,W.V.R. 1954a Proc. Roy.Soc.London A,225,185.

[36] Malkus,W.V.R. 1954b Proc.Roy.Soc.London A,225,196.

[37] Howard,L.N. 1963 J.Fluid Mech. 17,405.

[38] Busse,F.H. 1969 J.Fluid Mech. 37,457.

[39] Lumley,J.L.,Zeman,O. & Siess,J. 1978 J.Fluid Mech. 84,581.

[40] Townsend,A.A. 1959 J.Fluid Mech. 5,209.

[41] Willis,G.E. & Deardorff,J.W. 1967 Phys.Fluids 10,1861.

[42] Deardorff,J.W. & Willis,G.E. 1967 J.Fluid Mech. 28,675.

[43] Prandtl,L. 1945 Math.-Phys.KL.6.

[44] Hanjalic',K. & Launder,B.E. 1972 J.Fluid Mech. 52,609.

[45] Rodi,W & Spalding,D.B. 1970 W"arme-und Stoffubertragung ,3, No.2,85.

[46] Deissler,R.G. 1958 Phys.Fluids 1,111.

[47] Deissler,R.G. 1961 Phys.Fluids 4,1187.

[48] Deissler,R.G. 1963 Int.J.Heat Mass Transfer 6,257.

[49] Fox.J. 1964 Phys.Fluids 7,562.

[50] Deissler,R.G. 1962 J.Geophys.Res.,67,3049.

[51] Laufer,J. 1951 NACA Rep.1053,1247.

[52] Nakagawa,H. Nezu,I. & Ueda,H. 1975 Proc. Japan Soc.Civil Engi. No.241,155.

[53] Lukenhart,P.M. 1963 Communications of the ACM 6,737.

[54] Mizushina,T.,Ogino,F.,Ueda,H. & Komori,S. 1978 6th Int. Heat Transfer Conf. Toronto, Canada 1,MC16,91.

[55] Yeh,Y & Cummins,H.Z. 1964 Appl.Phys.Lett.4,176.

[56] Hong,N.S., Jones,A.R. & Weinberg,F.J. 1977 Proc.Roy. Soc.London A,353,77.

[57] Durst,F.,Melling,A. & Whitelaw,J.H. 1976 Principles and Practice of Laser-Doppler Anemometry. London:Academic Press.

[58] Edwards,R.V.,Angus,J.C. & Dunning,J.W. 1973 J.Appl.Phys. 44,1694.

[59] George,W.K. & Lumley,J.L. 1973 J.Fluid Mech.60,321.

[60] Rossi,B. 1967 Optics. London: Addison-Wesley Publishing Company.

VITA

Satoru Komori was born in Kyoto , Japan , on January 18 , 1951. After graduating from Syuchi High School , Kyoto , in 1969 , he entered Kyoto University Majoring in Chemical Engineering in 1970 and received the degree of Bachelor of Engineering in 1974, and Master of Engineering in 1976. Then, he advanced to the doctoral course of Kyoto University in 1976 and completed the course in 1979.

He has been serving as a research assistant in the Department of Chemical Engineering in Kyoto University from April 1979.

He is a member of Japan Society of Chemical Engineers.